TOWARDS CONSTRAINTS ON THE EPOCH OF REIONIZATION:

A PHENOMENOLOGICAL APPROACH

Matthew Malloy

A DISSERTATION

in

Physics and Astronomy

Presented to the Faculties of the University of Pennsylvania

in

Partial Fulfillment of the Requirements for the Degree of

Doctor of Philosophy

2015

Supervisor of Dissertation   **Graduate Group Chairperson**

Adam Lidz   R.U. Stupid

Professor, Physics and Astronomy   Professor, Physics and Astronomy

Dissertation Comittee:

Doc 1, Professor, Physics and Astronomy

Doc 2, Professor, Physics and Astronomy

Doc 3, Professor, Physics and Astronomy

Doc 4, Professor, Physics and Astronomy

Doc 5, Professor, Physics and Astronomy

Doc 6, Professor, Physics and Astronomy

TOWARDS CONSTRAINTS ON THE EPOCH OF REIONIZATION:

A PHENOMENOLOGICAL APPROACH

COPYRIGHT ©

2015

Matthew Malloy

Well, it looks like I brought piss to a shit fight.

Acknowledgements

ABSTRACT

TOWARDS CONSTRAINTS ON THE EPOCH OF REIONIZATION: A
PHENOMENOLOGICAL APPROACH

Matthew Malloy

Adam Lidz

Trust me . . . I did stuff . . . it was good. 350 words maximum here. . .

Contents

List of Tables

List of Figures

Preface

Perhaps you feel inclined to preface your work with poetic self-reflection about why you took up this project? Maybe a story that's kind of boring and ends with a joke that's not funny? Go for it!

Chapter 1

First Things First

1.1 Cosmic Context

Any organised system requires energy, be it a machine of some kind or a live organism. Energy is needed to win the uphill battle against entropy and pull together lifeless molecules to be able to do something in this world, like complete a PhD.

1.2 Overview of Selected Probes of the EoR

The Lyα Forest

The 21-cm Line

The Cosmic Microwave Background

Lyα Emitters

Luminosity Function Measurements

1.3 Current Constraints on the Timing and Nature of the EoR

Chapter 2

How to Search for Islands of Neutral Hydrogen in the $z \sim 5.5$ IGM

2.1 Introduction

It has been nearly half a century since **?**) pointed out that the lack of prominent absorption troughs, blueward of the Ly-α line in quasar spectra, implies that intergalactic hydrogen is highly ionized. Only in the year 2001 were complete "Gunn-Peterson" absorption troughs finally revealed in the Ly-α forest of high redshift ($z \gtrsim 6$) quasars discovered using the Sloan Digital Sky Survey (SDSS) (**? ? ?**). Although these prominent absorption troughs were discovered more than a decade ago, the precise interpretation of the observations, and their implications for the reionization history of the universe, remain unclear. One difficulty here relates to the large optical depth to Ly-α absorption: near $z \sim 6$, the optical depth is $\tau_\alpha \sim 4 \times 10^5$ in a fully neutral IGM at the cosmic mean density (**?**). Based on this, it is common to infer that the IGM must be highly ionized below $z \lesssim 6$, at which point quasar spectra do show some transmission through the Ly-α line. In addition, it is clearly hard to

discern whether the gas above $z \gtrsim 6$ – that does show complete absorption in the Ly-α line – is mostly neutral or is only neutral at the level of about one part in ten-thousand or so (e.g. Fan et al. 14); in either case, the Ly-α line will be completely absorbed.

However, if reionization is sufficiently inhomogeneous and ends late, there may be some transmission through the Ly-α forest *before reionization completes* (**? ?**). Theoretical models of reionization show that the IGM during reionization resembles a two-phase medium, containing a mixture of highly ionized bubbles along with mostly neutral regions. The ionized bubbles grow and merge, eventually filling essentially the entire volume of the IGM with ionized gas; the redshift at which this process completes is highly uncertain and still awaits definitive empirical constraint. In principle, the ionized bubbles may allow transmission through the Ly-α forest even when some of the IGM volume is still in fact filled by neutral regions, i.e., before reionization completes. This calls into question the conventional wisdom described above – that the presence of transmission through the $z \lesssim 6$ forest necessarily implies reionization completed by $z = 6$ (**? ?**) – strictly speaking, this conclusion follows only in the unrealistic case of a homogeneously-ionized IGM.

Indeed, some portions of the $z \sim 5 - 6$ Ly-α forest are completely absorbed, while other portions of the forest at these redshifts show transmission through the Ly-α line. Quantitatively, if one counts only the fraction of pixels with some transmission through the forest as "certain to be ionized", the volume-averaged neutral hydrogen fraction need only be smaller than $\langle x_{\mathrm{HI}} \rangle < 0.2$ at $5 \leq z \leq 5.5$, and smaller than $\langle x_{\mathrm{HI}} \rangle < 0.5$ at $z = 6$ (**?**). These constraints are conservative since even mostly-ionized gas will give rise to some completely absorbed regions at these redshifts, but it is nevertheless interesting to ask whether some of the absorbed regions could in fact come from remaining "islands" of mostly neutral hydrogen gas in the IGM. The dark pixel fraction constraints of **?**) certainly leave plenty of parameter space open for reionization completing at $z \leq 6$.

In fact, there are hints – albeit indirect ones – that significant amounts of neutral gas may remain in the IGM at these late times and so we believe that investigating this

possibility amounts to *more* than closing a remaining "loophole" in the analysis of the $z \lesssim 6$ Ly-α forest. For example, recent measurements of the rest-frame ultraviolet galaxy luminosity function suggest a relatively low ionizing emissivity at $z \gtrsim 5 - 6$, even for seemingly generous assumptions about the escape fraction of ionizing photons ($f_{\mathrm{esc}} \sim 0.2$) and allowing significant extrapolations down the faint end of the luminosity function; e.g. the preferred model of **?**) (that matches these observations) has $\langle x_{\mathrm{HI}} \rangle = 0.1$ at $z = 6$. In addition, the fraction of Lyman-break galaxies with detectable Ly-α emission lines shows evidence for a rapid drop between $z \sim 6 - 7$ which may require a significant neutral fraction at $z \sim 7$ (e.g., **?** **?** , although see **?** **?**). The inferred $z \sim 7$ neutral fraction here would be easier to accommodate if there is still some neutral gas at $z \le 6$. Furthermore, **?**) recently discovered an impressive ~ 110 Mpc/h dark region in the $z \sim 5.7$ Ly-α forest. This may result from an upward opacity fluctuation – driven by a fluctuating ultraviolet radiation field in a mostly ionized IGM – but this striking observation invites contemplating the more radical possibility that diffuse neutral regions remain in the IGM at this late time. Finally, **?**) and **?**) argue that the proximity zones of quasars at $z \ge 6$ show evidence for damping wing absorption and a significant neutral fraction, further motivating the search for neutral gas at slightly later times.

Perhaps more importantly, we can design robust observational tests for the presence of neutral islands in the $z \sim 5.5$ IGM, and either definitively detect neutral hydrogen at these redshifts, or significantly improve on the existing upper limits from **?**). Towards this end, we study three possible tests for identifying neutral islands in the $z \sim 5 - 6$ IGM, each of which can be applied using existing Ly-α forest spectra. The presence of some transmission through the Ly-α forest at $z \le 6$ allows us to consider tests that can not be applied at still higher redshift where the forest is completely absorbed (asides for in the "proximity zones" close to the quasar itself). We develop these tests using mock quasar spectra extracted from the numerical reionization simulations of **?**). The first test we consider has been studied before (e.g. Fan et al. 14, **?** , **?**), but is the most model dependent: the abundance and size

distribution of "dark gaps", i.e., regions of saturated absorption in the Ly-α forest. Here we focus on the plausible impact of inhomogeneous reionization on the dark gap statistics. The second test utilizes the fact that the natural line width of the Ly-α line gives rise to extended damping wing absorption, in the case that highly neutral gas is present in the IGM (39). As a result, the transmission recovers more slowly around significantly neutral absorbed regions than around absorbed yet ionized regions. We find that this signature can be detected in partly neutral models by examining the stacked profile around extended absorbed regions. Note that, in contrast to previous work, here we propose to search for the damping wing signature in typical regions of the IGM, as opposed to in the proximity zones of quasars (**? ?**), or redward of Ly-α at the source redshift. Our third test involves the stacked profile of extended absorbed regions in the Ly-β forest. If these regions are significantly neutral, there should be a feature from absorption in the deuterium Ly-β line just blueward (but not redward) of absorbed regions.

The outline of this paper is as follows. In §2.2, we briefly discuss which range of (volume-averaged) neutral fractions are physically plausible at $z = 5.5$. In §2.3 we describe the simulations used and the process for generating mock spectra. We discuss how the dark gap size distribution may be used to constrain the neutral fraction in §2.4. In §2.5, we describe how quasar spectra may be stacked in order to reveal the presence of deuterium and HI damping wing absorption in an idealized scenario and discuss adapting this approach for more realistic spectra in §2.6. We then apply this approach to mock quasar spectra in §2.7, discuss the constraining power of the stacking approaches in §2.8, and conclude in §2.17. Throughout, we consider a ΛCDM cosmology parametrized by $n_s = 1$, $\sigma_8 = 0.8$, $\Omega_m = 0.27$, $\Omega_\Lambda = 0.73$, $\Omega_b = 0.046$, and $h = 0.7$, (all symbols have their usual meanings), broadly consistent with recent Planck constraints from (**?**).

2.2 Viability of Transmission Through a Partially Neutral IGM

Ideally, this study would make use of mock Ly-α forest spectra extracted from fully self-consistent simulations of reionization, in which the efficiency of the ionizing sources and other relevant parameters are tuned so that reionization completes at $z \leq 6$. Unfortunately, large-scale reionization simulations that simultaneously resolve the properties of the gas distribution, as well as the sources and sinks of ionizing photons, while capturing large enough volumes to include a representative sample of the ionized regions, are still quite challenging. Here, we instead explore more approximate, yet more flexible, models. As we describe in more detail in the next section, we make use of the reionization simulations of ?) to describe the size and spatial distribution of the ionized and neutral regions during reionization. Inside of the ionized regions, we rescale the simulated photoionization rates, adjusting the intensity of the UV radiation field to match the observed mean transmitted flux through the Ly-α forest. For simplicity, we assume that the intensity of the UV radiation field in the ionized regions is uniform and comment on the possible impact of this approximation where relevant.

Before proceeding further, however, it is worth considering which (volume-averaged) neutral fractions are physically plausible near $z \sim 5.5$. In order to get transmission through the $z \sim 5.5$ Ly-α forest, at least some of the hydrogen needs to be highly ionized. This requires the mean free path of ionizing photons to be relatively large, although we should keep in mind that the attenuation length will vary spatially during and after reionization, and so this quantity needs to be large only across some stretches of the IGM. This in turn demands some minimum separation between the neutral islands, because otherwise the neutral islands themselves will limit the mean free path and prevent a sufficiently intense UV radiation field from building up between the islands. Hence, it may be inconsistent to have remaining neutral islands in the IGM, yet still have some transmission through

the Ly-α forest. Here we briefly quantify this reasoning; we will be content with only a rough estimate, as our focus here is more on designing empirical tests. Further theoretical exploration here might be valuable, however, perhaps along the lines of (**?**).

Quantitatively, previous studies infer that a photoionization rate on the order of $\Gamma_{HI} \sim 5 \times 10^{-13} \mathrm{s}^{-1}$ is required to match the mean transmitted flux in the $z \sim 5.5$ Ly-α forest (e.g., **?** , **?**).[1] If we demand that the photoionization rate between the neutral islands needs to be in this ballpark to allow transmission through the forest, we can translate this into a required minimum average separation between the neutral islands, given an assumed ionizing emissivity. The average ionizing emissivity is likely on the order of $\epsilon_{HI} \sim 3$ photons per atom per Gyr (e.g. **?**). This is close to the value required simply to balance recombinations and maintain the ionization of the IGM at the redshifts of interest. This emissivity is also comfortable with that inferred from the above photoionization rate and measurements of the mean free path to ionizing photons (**?** , although **?** recently argued for a slightly larger value), as well as the UV emissivity implied by measurements of the galaxy luminosity function (e.g. **?**).

In this context, it is useful to note that:

$$\Gamma_{HI} = \varepsilon_{HI} \sigma_{HI,lim} \lambda_{mfp} \frac{\beta}{\beta + 1.5}, \tag{2.1}$$

where ε_{HI} is the average proper ionizing emissivity, $\sigma_{HI,lim} = 6.3 \times 10^{-18} \mathrm{cm}^2$ is the photoionization cross section at the Lyman limit, λ_{mfp} is the mean free path of ionizing photons at the Lyman limit, and β is the intrinsic, unhardened spectral index of the ionizing radiation. This expression assumes that the mean free path to ionizing photons propagating through

---

[1]Theses studies assume that reionization is complete at these redshifts. If the universe is in fact partly neutral, then a higher photoionization rate should be required in the ionized regions. In our rough estimate here, we neglect this given the other significant uncertainties involved.

a clumpy IGM scales as $\nu^{3/2}$ (**?**). Inserting typical numbers we find:

$$\Gamma_{\rm HI} = 5.0 \times 10^{-13} {\rm sec}^{-1} \left[\frac{\varepsilon_{\rm HI}}{3 \text{ photons/atom/Gyr}} \right] \tag{2.2}$$

$$\times \left[\frac{\beta}{2} \right] \left[\frac{3.5}{1.5 + \beta} \right] \left[\frac{1 + z}{6.5} \right]^3 \left[\frac{\lambda_{\rm mfp}}{9.1 \text{ pMpc}} \right]. \tag{2.3}$$

In other words, to get transmission through the forest for plausible values of the ionizing emissivity, we require the mean separation between neutral islands to be $\lambda_{\rm min} \gtrsim \lambda_{\rm mfp} \gtrsim$ 9.1pMpc. This is a minimal requirement in that it assumes the neutral islands set the mean free path, when in fact Lyman limit systems and cumulative absorption in the mostly ionized gas may also play a role. On the other hand, the required minimum separation between the neutral islands would go down if a smaller $\Gamma_{\rm HI}$ suffices to allow transmission through the forest, or if the ionizing emissivity is in fact higher. However, the mean free path to ionizing photons has recently been measured at $z = 5.16$ to be $\lambda_{\rm mfp} = 10.3 \pm 1.6$pMpc (**?**), only somewhat larger than our assumed $\lambda_{\rm mfp}$ here. While there are still uncertainties, and while the measured mean free path scales steeply with redshift ($\lambda_{\rm mfp} \propto (1 + z)^{5.5}$), viable models are unlikely to have neutral islands spaced much more closely than this.

We can then use this requirement on $\lambda_{\rm mfp}$ to get some sense of which volume-averaged neutral fractions are plausible at $z \sim 5.5$. In the simulation outputs considered here (see §2.3), the mean separation between neutral islands is $\lambda_{\rm mfp} = 17.0$ pMpc, 5.3 pMpc, and 2.7 pMpc for $\langle x_{\rm HI} \rangle = 0.05$, 0.22, and 0.35, respectively. The first case certainly satisfies the requirement described above, the second case is just a bit on the small side, while the third case is uncomfortably small. Given the uncertainties in this argument, and the possibility that the neutral islands are a bit larger than in our simulation (which would increase their mean separation at fixed filling factor), we consider all three cases, but refrain from considering still more neutral models. We regard the latter case ($\langle x_{\rm HI} \rangle = 0.35$) as an extreme scenario intended mostly for illustration.

Finally, it is worth keeping in mind that any remaining neutral islands will likely be photoionized on a short timescale. For example, using Eq. 1 in **?**) with $C = 3$, $M_{\rm min} =$

$10^9 M_\odot$, and $\zeta = 20$, the redshift interval over which the volume average ionized fraction transitions from $\langle x_i \rangle = 0.8$ to $\langle x_i \rangle = 1$ is only $\Delta z \sim 0.5$. However, it is possible that we are catching this – likely brief – phase in $z \sim 5.5$ Ly-α forest spectra and the possibility of testing this remains tantalizing.

2.3 Simulations and Mock Spectra

With the above discussion to frame the range of possibilities, we move to describe the numerical simulations used in this analysis and our approach to constructing mock Ly-α forest absorption spectra before reionization completes. We use simulated density and ionization fields generated from a dark matter simulation of (**?**) which tracks 1024^3 dark matter particles in a simulation volume with a co-moving sidelength of $L = 130$ Mpc$/h$. We assume that the gas closely follows the dark matter. In this work, we focus on redshift $z = 5.5$, but consider several possible neutral fractions. In practice, we obtain ionization fields with higher (lower) neutral fractions by using simulation outputs at higher (lower) redshifts. This should be an appropriate approximation since the statistical properties of ionized regions at a given neutral fraction are most sensitive to the neutral fraction and are relatively insensitive to the redshift at which the neutral fraction was attained (see McQuinn et al. 36 and Furlanetto et al. 18).

We generate mock quasar spectra according to the usual "fluctuating Gunn-Peterson" approach (e.g., **?**), with a few refinements to capture the main effects of incomplete reionization. First and foremost, we do not assume a fully ionized IGM. The transmission in the Ly-α forest is sensitive to the precise ionized fractions in the ionized phase of the IGM. In order to simplify our study, as mentioned in the previous section, we rescale the simulated photoionization rates in the ionized regions to match the observed mean transmitted flux through the Ly-α forest. We do this assuming ionization equilibrium, and a constant value of the UV background (with a photoionization rate per atom of Γ_{HI}) within ionized regions. Specifically, simulated pixels with $x_i > 0.9$ are considered highly ionized while less ionized

pixels are considered fully neutral.[1] This simplified approach allows us to consider a range of different possibilities for the ionization state of the IGM quickly. We comment on the shortcomings of this approach when appropriate. The optical depth of a given pixel, i, in the simulation can then be found by summing over contributions from neighboring pixels (Bolton & Haehnelt 2008):

$$\tau_\alpha(i) = \frac{c\sigma_\alpha \delta R}{\pi^{1/2}} \sum_j \frac{n_{\mathrm{HI}}(j)}{b(j)} H(a,x),$$ (2.4)

where $b(j) = (2k_{\mathrm{B}}T(j)/m_p)^{1/2}$ is the Doppler parameter, $T(j)$ is the temperature of pixel j, δR is the pixel proper width, $\sigma_\alpha = 4.48 \times 10^{-18}\mathrm{cm}^2$ is the Ly α scattering cross section, m_p is the proton mass, $H(a,x)$ is the Hjerting function, and $n_{\mathrm{HI}}(i)$ is the number density of hydrogen atoms at pixel i, found using the simulated density field. To calculate the Doppler parameter, we assume that the gas obeys a modified temperature-density relationship

$$T(\delta) = \begin{cases} T_0(1+\delta)^{\gamma-1} & \text{if ionized} \\ 1,000\mathrm{K} & \text{if neutral,} \end{cases}$$ (2.5)

where δ is the matter overdensity in units of the cosmic mean and we choose $T_0 = 2 \times 10^4\mathrm{K}$ and $\gamma = 1.3$ as the temperature at mean density and slope of the temperature-density relation, respectively. For simplicity, we assume the ionized gas lies on the aforementioned temperature-density relation, although there should be significant scatter around this relation close to reionization (e.g. **?**). We do not expect this to impact our conclusions significantly. The neutral gas should be colder than the ionized gas, of course, with a temperature set perhaps by low levels of X-ray pre-heating. Here we adopt $T = 1,000$ K for the neutral gas; this choice is likely a bit large (it was chosen partly for ease in computing the Hjerting function below), but we have checked that we get nearly identical results for colder temperature choices.

---

[1]After effectively thresholding the ionization field in this way, we end up with neutral fractions which are $\approx 20\%$ higher than in the original simulation. Throughout the paper, we refer to increased, thresholded neutral fractions.

The Hjerting function is a convolution of a Lorentzian profile, which incorporates the natural line profile of the Lyman-series lines, with a Maxwell-Boltzmann distribution, which accounts for the effects of thermal broadening on the line profile. The Hjerting function is defined by:

$$H(a, x) = \frac{a}{\pi} \int_{-\infty}^{\infty} \frac{e^{-y^2} \mathrm{d}y}{a^2 + (x - y)^2},$$

where $a = \Lambda_\alpha \lambda_\alpha / 4\pi b(j)$, $\Lambda_\alpha = 6.265 \times 10^8 \sec^{-1}$ is the damping constant, $\lambda_\alpha = 1215.67$r A is the Ly α wavelength, x is the relative velocity of pixel i and pixel j in units of the Doppler parameter, defined as $x = [v_\mathrm{H}(i) - u(j)]/b(j)$, where $u(j) = v_\mathrm{H}(j) + v_{\mathrm{pec}}(j)$. The peculiar velocity field is generated by applying linear perturbation theory to the underlying density field.[1] In detail, the natural line profile is only approximately described by a Lorentzian (**?**), with asymmetric corrections becoming important far from line center. In this study, the precise shape of the damping wing far from line center is unimportant: we make use only of the gradual recovery in transmission around saturated neutral regions, rather than the detailed shape of this recovery, which is also strongly influenced by neighboring neutral regions. We hence expect the Lorentzian form to be a good approximation for our present purposes.

In addition to including absorption from the hydrogen damping wing, we also include absorption from primordial deuterium. As a result of big bang nucleosynthesis, primordial hydrogen should be accompanied by traces of deuterium, with a relative abundance by number of $D/H = 2.5 \times 10^{-5}$ (**?**). Due to its slightly increased reduced mass, Lyman series transitions in deuterium will be shifted blueward by 82km/s compared to the same transitions in hydrogen. We account for deuterium by scaling the number density of hydrogen in a given pixel by the relative abundance and shifting the resulting optical depths blueward by

---

[1]This was done because the full peculiar velocity field was not readily available, but this approximation should not impact our results.

82km/s. Additionally, the Doppler parameter is adjusted to $b_\mathrm{D}(j) = (2k_\mathrm{B}T(j)/(2m_p))^{1/2}$ to account for the increase in mass.

In this work, we focus mostly on $z = 5.5$ and adopt a mean transmitted flux at this redshift of $\langle F \rangle = 0.1$, consistent with determinations from e.g., (**?**). In some cases, we test the sensitivity of our results to the mean transmitted flux by considering $\langle F \rangle = 0.05$ as well. In general, the lower the mean transmitted flux, the more challenging it is for us to identify any remaining neutral islands. On the other hand, the likelihood that neutral islands remain increases towards high redshift and decreasing mean transmitted flux. As mentioned previously, we rescale the simulated photoionization rates in the ionized regions to a uniform value, normalized so that an ensemble of mock spectra matches the observed mean transmitted flux. It is important to note that the mean transmitted flux is a very steep function of redshift near $z \sim 5.5$, and that the sightline-to-sightline scatter in this quantity is substantial (14), and so one may want to carefully test for sensitivity to the precise redshift binning used.

We use the same approach as described above to generate $\mathrm{Ly}\,\beta$ mock spectra, with $\lambda_\beta = 1025.72\mathrm{r}$ A, $\Lambda_\beta = 1.897 \times 10^8\,\mathrm{sec}^{-1}$, and $\sigma_\beta = 7.18 \times 10^{-19}\mathrm{cm}^2$. However, in generating $\mathrm{Ly}\,\beta$ mock spectra, we must also account for foreground $\mathrm{Ly}\,\alpha$ absorption due to gas at lower redshifts, $\lambda_\alpha(1 + z_{\mathrm{Ly}\alpha}) = \lambda_\beta(1 + z_{\mathrm{Ly}\beta})$, where $z_{\mathrm{Ly}\alpha}$ is the redshift of the foreground $\mathrm{Ly}\,\alpha$ absorber and $z_{\mathrm{Ly}\beta}$ is the redshift of the $\mathrm{Ly}\,\beta$ absorber. We will assume we are investigating quasar spectra at $z_{\mathrm{Ly}\beta} = 5.5$ for this work, such that the corresponding foreground $\mathrm{Ly}\,\alpha$ absorption in the $\mathrm{Ly}\,\beta$ spectra occurs at redshift $z_{\mathrm{Ly}\alpha} = 4.5$. We adjust Γ_HI for the foreground $\mathrm{Ly}\,\alpha$ absorption to match measurements of the mean transmission from (**?**) at these redshifts ($\langle F \rangle \approx 0.31$ at $z = 4.5$).[1] The optical depth of a pixel in a $\mathrm{Ly}\,\beta$ spectrum

---

[1]We generate foreground $\mathrm{Ly}\,\alpha$ absorption by considering the absorption from regions in the same simulation box, but demand that they are widely-separated from the high redshift regions of interest ($> 10\ \mathrm{Mpc}/h$). This enforces that the underlying density fields sourcing the $\mathrm{Ly}\,\beta$ absorption and the foreground $\mathrm{Ly}\,\alpha$ absorption are uncorrelated, as should be the case for actual spectra.

is then the sum of the contribution from the foreground Ly α absorption and the intrinsic Ly β absorption $\tau_\beta^{\text{tot}}(z_{\text{Ly}\beta}) = \tau_\beta(z_{\text{Ly}\beta}) + \tau_\alpha(z_{\text{Ly}\alpha})$.

In Fig. 2.1, we show an example mock Ly α spectrum for a particular line of sight through the simulation. We show only a portion of the line of sight in order to exhibit smaller-scale features. The top figure shows the Ly α transmission when the hydrogen damping wing is neglected (black) and when it is included (dashed red), while the bottom panel shows the underlying thresholded ionization field. We have neglected peculiar velocities in creating this figure in order to facilitate a comparison between the spectrum and the underlying ionization field.

From this figure, we see that the damping wing indeed has a significant effect on the transmission, but that its effect is hard to discern without knowing the damping-wing-less transmission. This is the case for two reasons. First, the forest here is very absorbed and the damping wing absorption becomes mixed with resonant absorption from neighboring ionized regions. Second, the damping wing from a particular neutral region may overlap with the damping wing from another neutral region, altering the shape of the resulting absorption. Specifically, we see that, in the example spectra, the region at $v \approx 4500$ km/s is sandwiched between HI regions to the left and right, both within 1000km/s. Therefore, the optical depths for the corresponding pixels likely have significant contributions from resonant absorption, damping wing absorption from the HI region to the left, and damping wing absorption from the HI region to the right. While detecting individual instances of damping wing absorption in this case seems impossible, we will show that detecting the presence of damping wing absorption *on average* should be feasible through the stacking of high-redshift quasar spectra.

2.4 Dark Gap Statistics

With the mock spectra of the previous section in hand, we now consider the size distribution of regions of saturated absorption – dark gaps – and its dependence on the underlying neutral

fraction. Using such dark gap statistics has been widely discussed as a potential probe of the IGM neutral fraction (see, e.g., Fan et al. 14, **?** , **?** , **?**). In a fully ionized IGM, the size of dark gaps in quasar spectra should grow with increasing redshift, simply owing to the increasing mean density of the universe and as a result of any decline in the intensity of the UV radiation background. However, once quasar spectra start to probe the tail end of reionization, the increase in dark gap size should accelerate due to the presence of islands of neutral hydrogen.

In Fig. 2.2, we have plotted the size distribution of dark gaps, $dP(L)/d\ln L$, in blue for the $\langle x_{\rm HI} \rangle = 0.22$ mock spectra, assuming a mean transmission of $\langle F \rangle = 0.1$. Additionally, the dashed curves display the two underlying populations of dark gaps: those sourced by ionized gas (magenta) and those sourced by neutral gas (cyan). For clarity, we only show dark gaps larger than $L_{\rm sat,min} = 0.7$ Mpc/h (~ 90km/s), since smaller saturated regions will be predominantly ionized. Additionally, we have neglected peculiar velocities when generating spectra here. Two important points become apparent from this figure. First, at $L \sim 8.5$ Mpc/h (~ 1100km/s), dark gaps transition from being primarily sourced by ionized gas to being primarily sourced by neutral gas. This reinforces our intuition that, in a partially neutral IGM, the largest dark gaps should correspond to the remaining neutral islands. Second, the dark gaps being composed of two different populations gives rise to a bimodality in the size distribution. This suggests that the behavior of the large-L tail of the size distribution may offer additional information about the neutral fraction, with a steep decline suggesting a highly ionized IGM and a more gradual decline, or the emergence of a second peak, suggesting a significantly neutral IGM. Such a "knee" in the dark gap size distribution is also mentioned in (**?**).

Additionally, we can consider the large-L tail of the size distribution and its dependence on neutral fraction at a fixed mean transmission. In Fig. 2.3, we plot an expected histogram of dark gap sizes for 10 spectra for $\langle x_{\rm HI} \rangle = 0$ (magenta), 0.05 (cyan), 0.22 (blue), and 0.35 (black), again assuming that $\langle F \rangle = 0.1$. Three trends become obvious from this plot. First,

as the neutral fraction is increased (at fixed $\langle F \rangle$), the number of large saturated regions increases and, second, as the neutral fraction is increased, the size of the largest dark gaps also increases. For example, in the $\langle x_{\mathrm{HI}} \rangle = 0.22$ model, the largest dark gaps are roughly five times bigger than in the fully ionized model. Additionally, we again see hints of the underlying dark gap size distribution being bimodal as the neutral fraction is increased, supporting the idea that the *shape* of the dark gap size distribution may be a diagnostic for the underlying neutral fraction.

Given these trends, it should be possible to compare dark gap distributions from observed spectra against models at various neutral fractions and use this to constrain the mean neutral fraction of the IGM. This approach is appealing in that it does not require especially high-resolution or high signal-to-noise spectra. However, it does require comparison with simulated models of the dark gap size distribution and so the conclusions reached will be somewhat model dependent. Additionally, the distributions are dependent on the assumed mean transmission, which is itself uncertain. In particular, estimates of the mean transmission at high redshift may be impacted by continuum fitting errors, given the inherent difficulty in estimating the unabsorbed continuum level in highly-absorbed spectra.

In order to investigate the impact of possible continuum fitting errors, we generate mock spectra in the fully ionized model with $\langle F \rangle = 0.03$ but then rescale the flux in each simulated pixel by a multiplicative factor – to mimic the effect of continuum misplacement – such that the measured mean transmitted flux appears to be $\langle F_{\mathrm{meas}} \rangle = 0.1$. This case is shown as the magenta dashed line in Fig. 2.3. Here the dark gap size distribution is shifted towards sizes than one would expect in an ionized model at $\langle F \rangle = \langle F_{\mathrm{meas}} \rangle = 0.1$. However, the shape of the size distribution is still quite different than in the partly neutral models. Importantly, the dark gap distribution in the ionized model still lacks the distinctive bump at large sizes that is the hallmark of a partly neutral IGM in our models.

2.5 Stacking Toy Spectra

In this section we describe our basic approach of stacking $Ly\,\alpha$ and $Ly\,\beta$ spectra in order to detect the presence of HI damping wings and absorption due to deuterium, respectively. While the forest is too absorbed at these redshifts to easily detect damping wings or deuterium absorption due to individual neutral regions, here we demonstrate that the presence of such features can be revealed *on average* by stacking regions of transmission over many spectra.

This section serves as a proof of principle by applying a simplified stacking approach to mock spectra generated using an idealized IGM model. Specifically, we consider an ensemble of sightlines through our simulation box and assume that the IGM is entirely ionized with the exception of a single HI island with mean density and varying length, L, inserted randomly along each line of sight. We then generate mock spectra assuming these density and ionization fields. The stacking in this section is always done starting at the HI/HII boundaries of a given HI region moving outward.

HI Damping Wing

Our stacking approach can be clearly demonstrated by considering the damping wing from neutral hydrogen. Due to the natural width of the $Ly\,\alpha$ line, a neutral hydrogen gas parcel should cause $Ly\,\alpha$ absorption over a range of frequencies. Far from line center, this absorption will have an optical depth roughly following (**?**):

$$\tau_{Ly\alpha}^{DW}(\Delta v) \approx \frac{\tau_{GP} R_\alpha c}{\pi} \left[\frac{1}{\Delta v} - \frac{1}{\Delta v + v_{ext}} \right] \tag{2.6}$$

where τ_{GP} is the Gunn-Paterson optical depth, $R_\alpha \equiv \Gamma_\alpha \lambda_\alpha / 4\pi c$, $\Gamma_\alpha = 6.265 \times 10^8 \, \mathrm{sec}^{-1}$ is the $Ly\,\alpha$ decay constant, Δv is the separation from the HI/HII boundary in velocity space, v_{ext} is the extent of the hydrogen region in velocity space, and c is the speed of light. For a large neutral region, this equation implies that $\tau_{Ly\alpha}^{DW}(|v| < 600\mathrm{km/s}) \geq 1$ at $z \sim 5.5$. This

excess absorption is referred to as the hydrogen "damping wing". While both neutral gas and highly ionized gas can cause absorption in quasar spectra, only a significantly neutral hydrogen patch will result in damping wing absorption, owing to the greatly reduced optical depth in the wing compared to line center. As such, detecting damping wing absorption would be a smoking gun for the presence of significantly neutral hydrogen islands. Note that the transmission profile will differ from the simple form of Eq. 2.6, owing mostly to neighboring neutral regions, however the gradual recovery to transmission around saturated neutral regions should be a distinctive indicator that highly neutral regions remain in the IGM.

In Fig. 2.4 we show the results of stacking transmission outside of neutral regions in the toy mock spectra described earlier in this section, neglecting deuterium for the time being. Namely, we show the stacked transmission outside neutral islands of length $L = 0.76$ Mpc/h (~ 100km/s) in black, $L = 1.27$ Mpc/h (~ 170km/s) in blue, $L = 5.34$ Mpc/h (~ 700km/s) in cyan, and stacked transmission neglecting the damping wing in red. Additionally, we have plotted the analytic curves corresponding to Eq. 2.6 for the various L values, shown with dashed curves. We have applied a single multiplicative factor to these curves to account for average resonant absorption from ionized gas. Together, this figure implies that damping wing absorption from isolated neutral regions has a significant impact on quasar spectra, extending ~ 1000km/s past the HI/HII boundaries, which may be observable through stacking as expected from Eq. 2.6.

In providing a toy example of how the hydrogen damping wing can affect spectra, we have neglected many important challenges that such a measurement would face. For example, we assumed perfect knowledge of the underlying ionization state of the IGM in order to determine where to stack and we assumed that we could discriminate between neutral and highly ionized absorption systems. However, the presence of such a large and potentially-observable feature provides motivation for us to apply the stacking approach in

a more realistic manner. In §2.6 and in Appendix B, we describe several such challenges and subtleties along with potential resolutions.

Deuterium

With the stacking approach of the previous section in mind, we now consider absorption due to deuterium. As noted in §2.3, primordial hydrogen should be accompanied by traces of deuterium, with a relative abundance of $\sim 2.5 \times 10^{-5}$ (**?**). Due to its slightly increased reduced mass, atomic transitions in deuterium are shifted blueward by 82km/s compared to the same transitions in hydrogen. This implies that absorption due to neutral hydrogen in the IGM should be accompanied by additional absorption from deuterium, shifted blueward by 82km/s. We can estimate the optical depth for Lyα absorption in deuterium at cosmic mean density by simply scaling the hydrogen Lyα optical depth by the deuterium abundance:

$$\tau_{D,\alpha} = \left[\frac{D}{H}\right] \times \tau_{\mathrm{GP}} \approx 8.25 x_{\mathrm{HI}} \left(1+\delta\right) \left[\frac{1+z}{6.5}\right]^{3/2}. \tag{2.7}$$

Thus, we see that while the relative abundance of deuterium is extremely small, the Gunn-Peterson optical depth is so large that the resulting deuterium optical depth is still of order 10 in Lyα.

An appealing aspect of searching for damping wing absorption is that the optical depth in the wing is large enough to cause significant absorption in the presence of neutral islands, but small enough to be negligible for ionized absorption systems. We see this again in the case of deuterium absorption, suggesting that it may be useful as an additional "smoking gun" indicator for underlying neutral hydrogen. However, an obvious problem with detecting deuterium in Lyα spectra is that the feature should be narrow and well within the broad range of velocities where the hydrogen damping wing is significant. Specifically, according to Eq. 2.6, at $\Delta v = 82$km/s, the damping wing optical depth for an extended neutral region

should be $\tau_{\mathrm{Ly}\alpha}^{\mathrm{DW}}(\Delta v \approx 82\mathrm{km/s}) \approx 8$. Therefore, the feature should be completely wiped out in Ly α spectra by the hydrogen damping wing.

However, the damping wing optical depth in the Ly β line is much smaller. Specifically, according to Eq. 2.6, the damping wing optical depth scales as

$$
\begin{aligned}
\frac{\tau_{\mathrm{Ly}\beta}^{\mathrm{DW}}}{\tau_{\mathrm{Ly}\alpha}^{\mathrm{DW}}} &= \frac{\tau_{\mathrm{GP},\beta}}{\tau_{\mathrm{GP},\alpha}} \times \frac{R_\beta}{R_\alpha} = \frac{f_\beta \lambda_\beta}{f_\alpha \lambda_\alpha} \times \frac{(\Gamma_\beta + \Gamma_{\mathrm{H}\alpha})\lambda_\beta}{\Gamma_\alpha \lambda_\alpha} \\
&= \frac{f_\beta^2}{f_\alpha^2}\left(1 + \frac{f_{\mathrm{H}\alpha}}{f_\beta}\frac{\lambda_\beta^2}{\lambda_{\mathrm{H}\alpha}^2}\right) = .0410,
\end{aligned}
\tag{2.8}
$$

and should therefore be significantly narrower in Ly β than in Ly α. In the above expression, f_α, f_β, and $f_{\mathrm{H}a}$ are the oscillator strengths of the Ly α, Ly β, and Balmer-α transitions, respectively, with λ denoting the corresponding wavelengths and Γ denoting the corresponding decay constants. By modifying Eq. 2.6 for Ly β, we see that $\tau_{\mathrm{Ly}\beta}^{\mathrm{DW}}(|\Delta v| \gtrsim 25\mathrm{km/s}) \leq 1$. Therefore we find that *the hydrogen damping wing should not wipe out deuterium absorption features in Ly β.* Furthermore, while the hydrogen damping wing optical depth is reduced by a factor of roughly f_β^2/f_α^2 when considering Ly β, the total optical depth in the deuterium line is only reduced relative to deuterium Ly α by $f_\beta \lambda_\beta/f_\alpha \lambda_\alpha \approx 1/6$, such that the optical depth should still be of order 1 for deuterium Ly β. Therefore, not only should a deuterium absorption feature survive the hydrogen damping wing, but it should still have a strong enough optical depth to cause significant absorption if neutral islands in fact remain.

Naturally, it should be very difficult to detect individual deuterium absorption features from the diffuse IGM, as the Ly-β spectra will be very absorbed when the universe is neutral enough to produce the features in the first place. However, the feature may nonetheless be observable *on average* through the stacking of high-resolution quasar spectra. In order to demonstrate the strength of the deuterium absorption feature in stacked spectra, we incorporate deuterium into the same toy sightlines from §2.5 to produce mock Ly β spectra, neglecting foreground Ly α absorption for the time being. We are then able to stack transmission outside of neutral regions in the spectra, starting at the HI/HII boundaries

and moving outward. However, since deuterium absorption will only occur on the blue side of neutral regions, we need only stack those regions of transmission. In fact, this offers a clean test for detecting deuterium. Namely, we can separately stack transmission redward and blueward of neutral regions and compare. Excess absorption on the blue side of neutral regions, on average, could signal the presence of deuterium absorption. This is especially appealing since there should be no sources of contamination that would cause a similar, and significant, red/blue asymmetry.[1]

In Fig. 2.5, we show the results of stacking transmission in Ly β redward (red) and blueward (black) of the toy neutral regions across the full ensemble of mock quasar spectra. As in Fig. 2.4, all stacking begins at HI/HII boundaries. We can see the blueward transmission clearly exhibits excess absorption due to deuterium extending roughly $\sim$80km/s from the HI/HII boundary. Thus, in this idealized scenario, the presence of deuterium in islands of neutral hydrogen leaves a very clear signature in the stacked Ly β transmission.

Before proceeding further, we should point out one important caveat here. In our simulated models, the transition between fully neutral and highly ionized regions is, by construction, perfectly sharp. If this transition is more gradual in reality, then the narrow deuterium feature could be overwhelmed by absorption from mostly ionized hydrogen in this transition region. A minimal scale for this transition region is set roughly by the mean free path to ionizing photons through the neutral IGM, which is only $\lambda_{\mathrm{HI}} \sim 1/(n_{\mathrm{HI}}\sigma_{\mathrm{HI}}) \approx$ 6proper kpc/$h \approx 0.8$km/s. This minimal scale is two orders of magnitude smaller than the scale of the deuterium feature and hence does not present a worry. However, if the edges of the ionized regions tend to experience a reduced ionizing background, this might obscure

---

[1]One source of asymmetry we do find, which can be seen in Fig. 2.9, results from the fact that, when dealing with realistic spectra, we force there to be transmission in Ly β at the locations where stacking begins. This results in a small selection effect, where selected neutral absorption systems have a reduced probability of having nearby neutral regions and have correspondingly-smaller nearby optical depths. For deuterium, this smaller optical depth is shifted blueward, causing *less* absorption on the blue side of the line for $\Delta v \gtrsim 82$km/s. However, this asymmetry is minor and *opposes* the asymmetry from deuterium absorption.

the deuterium feature, even in the case of a partly neutral IGM. We believe the possibility of detecting this deuterium feature is enticing enough to warrant further investigation.

As was the case in §2.5, we have made several simplifying assumptions and have additionally neglected foreground Ly α absorption from the lower-redshift IGM. However, the clear presence of deuterium absorption revealed through the simplified stacking approach provides motivation to also consider applying it to more realistic spectra, as will be discussed in §2.6.

2.6 Steps of Approach

In §2.5, we demonstrated the utility of stacking idealized quasar spectra in order to reveal the presence of the HI damping wing and deuterium absorption. The success of this approach in the toy case provides motivation for us to apply it to realistic mock spectra. In doing so, we must confront the simplifying assumptions made in §2.5.

The most obviously unrealistic assumption made in §2.5 is that we can precisely identify the HI/HII boundaries underlying our spectra. In practice, we will only have access to the level of transmission at each point along the spectra. However, based on Fig. 2.5, the recovery from saturated absorption to transmission occurs within $\lesssim$ 15km/s in Ly β from the edge of the neutral zone, and should therefore provide a relatively good indicator of the HI/HII boundary. Therefore, we choose to identify stacking locations based on where transmission recovers *in Lyβ*. To be clear, for the case of the hydrogen damping wing, we are stacking transmission in the Ly α forest, but we are choosing where to start the stacking based on features in the Ly β forest. A drawback of this approach, when searching for the hydrogen damping wing, is that we are only able to stack regions of the Ly α forest with corresponding regions in the Ly β forest that are not contaminated by Ly γ absorption. This effectively reduces the amount of usable spectra, since, for a quasar at $z = 5.5$, the pure Ly α forest will extend $4.5 \leq z \leq 5.5$, but Ly γ absorption will contaminate the Ly β forest

at $z \lesssim 5.16$. If presented with a limited number of spectra, it may be worth searching for the damping wing by using only the Ly α regions of the spectra.

By stacking at the precise locations of HI/HII boundaries in §2.5, we were also ensuring that our sample of absorption systems was all neutral. However, when we modify our approach to begin stacking at locations where transmission recovers from saturated absorption, we may start stacking transmission outside of ionized absorption systems together with transmission outside of neutral absorption systems, diluting our signal. Since the signal we are aiming to find is small to begin with, it is important that we minimize this contamination from ionized regions. To do this, we take advantage of the main argument of §2.4, namely that regions of saturated absorption sourced by neutral gas should be significantly larger, on average, than those sourced by ionized gas. Therefore, we choose to stack only transmission outside of *large* regions of saturated absorption. Furthermore, since true neutral regions should cause saturated absorption in Ly β, we choose to stack only outside of large saturated regions which are fully absorbed in Ly β, where we define "large" to be $> 500\mathrm{km/s}$ ($\gtrsim 4\ \mathrm{Mpc}/h$) in Ly β. Note that this choice is tuned for the case of $\langle F \rangle = 0.1$: a different choice may be better for other values of the mean transmitted flux. At any rate, in applying these tests to real data, one would likely vary this size scale across a range of possible values.

Additionally, an appealing feature of the search for deuterium absorption is that it offers a very clean test for its detection, namely a red/blue asymmetry in the transmission outside of plausibly neutral regions. The disparity in the size distribution of saturated regions sourced by neutral and ionized gas suggests a similar test may be possible for the detection of the HI damping wing. Namely, while large regions of saturated absorption are likely to be sourced by neutral gas, small regions of saturated absorption are likely to be sourced by ionized gas. Therefore, to find evidence of excess absorption outside of neutral regions due to the HI damping wing, we compare the stacked transmission outside of large absorption systems, plausibly sourced by neutral gas, to that outside of small absorption

systems, likely sourced by ionized gas. A significant amount of excess absorption outside of the former compared to the latter, extending further than any possible density correlations, would suggest the presence of damping wing absorption.

Furthermore, in §2.5, we discussed how the damping wing is greatly weakened in Ly β compared to in Ly α. Therefore, an additional test for the presence of damping wing absorption could be to take the ratio of the stacked Ly β transmission to the stacked Ly α transmission, where stacking occurs in the same physical regions in both cases. In the event that there is significant damping wing absorption, this ratio should also slowly recover to some constant value at large Δv. We further discuss and develop this approach in Appendix B.

When dealing with realistic spectra, we must adjust our approach to accommodate the presence of noise (and finite spectral resolution). While noise should average out in stacked regions, the presence of noise will also obfuscate the precise boundaries between saturated absorption and transmission. We choose to handle this by smoothing our noisy spectra over a scale of 100 km/s (~ 0.75 Mpc/h) and defining any pixel, i, with transmission $F_i < 3\tilde{\sigma}_N$ to be consistent with saturated absorption, where $\tilde{\sigma}_N$ denotes the standard deviation of the smoothed noise. We then define regions in the smoothed spectra where the flux goes from $F < 3\tilde{\sigma}_N$ to $F > 3\tilde{\sigma}_N$ as the transitions from saturated absorption to transmission, and therefore as potential points to start stacking. When stacking transmission, however, we stack the transmission in the *unsmoothed* spectra.

Another concern is that damping wing absorption sourced by DLAs may erroneously be attributed to a significantly neutral IGM. However, in Appendix A, we estimate the expected rate of DLAs occurring in $z \sim 5.5$ quasar spectra and find it is small enough to be ignored. Additionally, DLAs may be discriminated from diffuse neutral islands based on the presence of metal lines and the relative sizes of their absorption in Ly α and Ly β.

Finally, as mentioned previously, we approximate the ionizing background in the ionized regions as uniform and ignore scatter in the temperature density relation. Accounting for

these fluctuations *might* lead to a more gradual recovery in the transmission around absorbed regions – in the case of a fully ionized universe – than in our models. Further investigation of this issue would certainly be required if a gradual recovery is indeed found in real spectra. In Appendix B, we discuss a possible empirical test that may help in this regard.

2.7 Results

Having considered the subtleties of the previous section, we are now ready to apply the three-pronged approach to more realistic mock spectra. In each section, we first consider the ideal case where no noise has been applied to give an idea of the potential constraining power of the different methods. Subsequently, we add realistic levels of noise and consider realistic spectra resolution to give an idea of the constraining power of the approaches applied to Keck HIRES spectra for the deuterium feature and damping wing, and spectra with slightly higher resolution than SDSS for the dark gap size distribution.

Detecting the Damping Wing

We first consider the ability to uncover the presence of the hydrogen damping wing by strategically stacking regions of transmission in the the $\mathrm{Ly}\,\alpha$ forest of $z \approx 5.5$ noiseless mock quasar spectra. As discussed in §2.6, our aim is to compare the average transmission outside of plausibly neutral absorption systems to the transmission outside of likely ionized systems.

We identify the plausibly neutral absorption systems by requiring the regions be completely absorbed in $\mathrm{Ly}\,\beta$, and also that the regions of saturated absorption are at least $L_{\mathrm{sat}} > 500\mathrm{km/s}$ ($\sim 4~\mathrm{Mpc}/h$) *in Lyβ*. We begin stacking at the point in the $\mathrm{Ly}\,\alpha$ spectrum which corresponds to the recovery from absorption to transmission *in Lyβ*. We identify the likely ionized absorption systems by requiring that they are *below* a maximum length $L_{\mathrm{max}} = 300\mathrm{km/s}$ *in Lyβ*.

In Fig. 2.6, we show the results of applying this approach to realistic mock spectra generated assuming various ionization states of the IGM. In the top panel, we show the stacked transmission outside of plausibly neutral absorption systems (solid) and likely ionized absorption systems (dashed), using a volume-averaged neutral fraction of $\langle x_{\mathrm{HI}} \rangle = 0.35$ (black), 0.22 (blue), 0.05 (cyan), and $\langle x_{\mathrm{HI}} \rangle = 0$ (magenta). The curves agree with our expectations, namely that transmission outside of neutral regions should recover more slowly and exhibit a rough damping wing shape with a large extent in velocity space. We see that the excess absorption extends *farther* than the $\lesssim 1000 \mathrm{km/s}$ expected from an isolated damping wing. However, as discussed in Appendix C, we find that the spatial clustering of neutral regions is responsible for this effect.

While, for several reasons discussed earlier, the shape of the absorption is distorted compared to Fig. 2.4, it can be seen for all significantly neutral ionization states. An important check is to apply the stacking procedure to a fully ionized IGM and ensure that we do not make a false detection. The results of this check are shown by the magenta curves in Fig. 2.6. As we can see, the resulting stacked transmission outside of plausibly neutral regions lacks an overall damping wing shape and stays roughly fixed near the mean transmission.

We can also see that the transmission outside of small absorption systems is very sensitive to the underlying neutral fraction. We expect this, however, since this stacked transmission depends strongly on the average transmission in regions which are not in saturated absorption, denoted $\langle F | F > 0 \rangle$. Since the dark pixel covering fraction in our mock spectra increases with $\langle x_{\mathrm{HI}} \rangle$, mock spectra with larger neutral fractions must have larger values for $\langle F | F > 0 \rangle$ to maintain $\langle F \rangle = 0.1$. As such, Fig. 2.6 shows that the stacked transmission outside of small absorption systems increases monotonically with $\langle x_{\mathrm{HI}} \rangle$.

We estimated the stacked transmission from a large ensemble of simulated spectra to produce a smooth estimate of the average transmission around saturated regions in each model. The transmission curves outside of individual absorption systems are, however, quite

noisy on their own such that, from saturated region to saturated region, there is significant scatter about the mean-value curves shown in the top panel. In order to estimate how confidently we can distinguish the solid and dashed curves with a reasonable number of quasar spectra, we scale the number of identified absorption systems to what we would expect using ~ 20 spectra. Specifically, we take the difference between the dashed and solid curves and divide by the scatter in each bin. The scatter of each bin is simply the scatter in stacked transmission outside of large absorption systems, scaled by $1/\sqrt{N_{\text{sat,large}}}$, added in quadrature with the scatter in the stacked transmission outside of small absorption systems, scaled by $1/\sqrt{N_{\text{sat,small}}}$. Here we scale to estimate the plausible scatter around the mean after estimating the transmission around saturated regions using 20 quasar absorption spectra.

The results of this are shown in the bottom panel of Fig. 2.6 for the same ionization states. The results appear to be very encouraging, indicating that, assuming noiseless spectra, the solid and dashed curves are $\gtrsim 5\sigma$ statistically-significantly different (*even for* $\langle x_{HI} \rangle = 0.05!$). In addition, we see that the difference roughly follows a damping wing shape and remains significant for $\gtrsim 3000$km/s. We should emphasize that, while the deuterium absorption feature will necessarily be a $\lesssim 80$km/s feature and require high resolution spectra to be seen, the damping wing feature extends an order of magnitude farther in velocity space and should be accessible to lower-resolution spectra.

In Fig. 2.7, we show the same results as in Fig. 2.6, but assume a lower mean transmission of $\langle F \rangle = 0.05$, consistent with spectra at $5.7 \lesssim z < 6$ (**?**). From the figure, we see that these results are very similar to those for $\langle F \rangle = 0.10$, but with the significance curves peaking at a $\sim 70\%$ lower value and with the stacked transmission recovering to a lower mean. Overall, this provides encouragement for applying the approach to higher-z spectra, suggesting that a range of physically interesting neutral fractions could be probed.

It is also interesting to consider these results when spectra are generated according to the specifications of existing data. In Fig. 2.8 we show the same results as in the bottom panel

of Fig. 2.6 except we have adjusted the spectra to mimic HIRES spectra. Namely, we have assumed a spectral resolution with FWHM = 6.7km/s and bins with size $\Delta v_{\mathrm{bin}} = 2.1$km/s (e.g. **?**). Additionally, we have assumed a signal to noise of SNR = 10 at the continuum per 2.1km/s pixel and that we have 20 such spectra. While we are currently only aware of 10 such spectra, this case is still interesting since spectra with significantly worse spectral resolution should also be adequate for this test.

From this figure, we can see that, despite the degradation of the spectra, the damping wing is still visible with the significance curve peaking at $\gtrsim 5\sigma$ ($\gtrsim 8\sigma$) significance for the $\langle x_{\mathrm{HI}} \rangle = 0.22$ (0.35) ionization state. However, this figure suggests that, in the $\langle x_{\mathrm{HI}} \rangle = 0.05$ case, it is less-clear whether the damping wing is detectable.

An important effect of adding noise to the mock spectra is that it obscures the precise location where spectra should be stacked and also increases the fraction of selected saturated regions which are, in fact, ionized. We find that for the spectra in this section $\sim 30\%$, 40%, and 75% of identified plausibly neutral regions are in in fact ionized for $\langle x_{\mathrm{HI}} \rangle = 0.35$, 0.22, and 0.05, respectively. This is compared to $\sim 7\%$, 10%, and 20% contamination when noise is neglected.

Statistical significances in this section are only estimates. In reality, the statistical significance with which the damping wing can be detected will depend on how extended the significance curves are, along with how correlated the errors in neighboring bins are. We discuss this in §2.8.

Deuterium Feature Results

We now turn to consider the prospects for identifying deuterium absorption in realistic Lyβ mock spectra. As discussed in §2.6, our aim is to identify plausibly neutral absorption systems in the Lyβ spectra and compare the stacked transmission moving blueward and redward away from the absorption. We identify the plausibly neutral regions in the same manner as for the damping wing.

In Fig. 2.9, we show the results of applying the stacking approach to the same mock spectra as in the previous section. The top panel shows the mean transmission blueward (solid) and redward (dashed) moving away from plausibly neutral absorption systems for the same ionization states as in the previous section. We can very clearly see excess absorption in the partially neutral spectra, extending ~ 80km/s, consistent with our expectations from Fig. 2.5. Additionally, we also find that, in the fully ionized case, the blueward and redward stacked transmission match up very well.

As in the previous section, we can construct a rough significance curve for the difference between the blueward and redward transmission. Specifically, in the bottom panel of Fig. 2.9 we show the excess blueward absorption in units of the standard deviation of the stacked blueward transmission assuming 20 quasar spectra. We can see that the significance of the red/blue asymmetry extends ~ 70km/s (~ 0.3 Mpc/h) and is $\gtrsim 3\sigma$ for all of the partially neutral models considered, with increasing significance for models with higher neutral fractions. Additionally, we see that the curve corresponding to the fully ionized model shows no statistically-significant deviation from red/blue symmetry. Thus, this is indeed a very clean test for the presence of deuterium. However, the signal itself is an order of magnitude smaller in velocity-space extent and is found with significantly less statistical significance than the damping wing signal. Therefore, we expect that high-resolution, high-signal-to-noise spectra will be necessary to search for it.

As in §2.7, we can reproduce Fig. 2.9 assuming spectra with specifications mimicking Keck HIRES. Unfortunately, we find that, with a signal to noise per pixel in the continuum of 10, the deuterium feature is hard to observe. Because of this, we consider using 20 HIRES-style spectra with a signal to noise per pixel of 30 in the continuum. While this signal-to-noise value is higher than those for existing spectra we found in the literature, it is not unreasonable to assume such spectra may become available in the future. Furthermore, this may provide additional motivation to obtain such spectra. Regardless, after applying the stacking approach with twenty SNR = 30 HIRES spectra, we obtain the results shown

in Fig. 2.10. This figure shows that the feature should be observable with modest statistical significance. Specifically, for $x_{\mathrm{HI}} = 0.35$ (0.22) the significance curve peaks at $\sim 3.7\sigma$ ($\sim 3\sigma$). Additionally, when these curves are generated assuming MIKE-style spectra, with spectral resolution FWHM = 13.6km/s and velocity bin size $\Delta v_{\mathrm{bin}} = 5.0$km/s, we obtain similar curves as in Fig. 2.10 but with the signal being statistically significant over a smaller range of velocities.

Again, important effects of adding noise to the mock spectra are that it obscures the precise location where spectra should be stacked and increases the fraction of selected plausibly neutral regions which are, in fact, ionized. We find that for the spectra in this section $\sim 15\%$, 20%, and 40% of identified plausibly neutral regions are in in fact ionized for $\langle x_{\mathrm{HI}} \rangle = 0.35$, 0.22, and 0.05, respectively. This is compared to $\sim 7\%$, 10%, and 20% contamination when noise is neglected. As expected, we find a smaller level of contamination than in the previous section, owing to the increased signal to noise of the spectra used. However, for the case of deuterium, the effect of noise on the stacking location is more apparent. Fig. 2.9 demonstrates that, without noise, deuterium absorption imprints a feature on stacked noiseless spectra extending ≈ 80km/s, but only extending ≈ 60km/s in stacked noisy spectra, as shown in Fig. 2.10.

The above results suggest that stacking Ly β transmission in high-z spectra can indeed be used to detect the presence of primordial deuterium, and hence that of hydrogen, but that high-resolution and high signal-to-noise spectra will be required. Nevertheless, it would certainly be interesting to apply this approach to existing HIRES/MIKE spectra as it provides an additional test, independent of the damping wing search, for the presence of underlying neutral hydrogen in the IGM. As such, a detection with modest levels of statistical significance could lend credence to a claimed detection of the HI damping wing.

Dark Gap Statistics

We now shift our focus away from stacking and toward the distribution in lengths of regions of saturated absorption (dark gaps). As discussed in §2.4, the dark gap size distribution in quasar spectra should contain information about the underlying ionization state of the IGM. Specifically, in a more neutral IGM, the typical sizes of dark gaps should be larger and the shape of the dark gap size distribution should have a more gradual decline, and possibly show a hint of bimodality, toward large L.

We continue this discussion in this section by considering plausible dark gap size distributions that could be observed with moderate-resolution, moderate-signal-to-noise spectra. Specifically, we consider spectra with spectral resolution FWHM = 100km/s, bin size $v_{\rm bin}$ = 50km/s, and a signal-to-noise ratio of 10 at the continuum. These spectra are of only slightly better quality than SDSS spectra. Additionally, since we are not concerned with Ly β transmission, we are able to use the entire Ly α forest for each spectra.

In Fig. 2.11, we show the resulting dark gap size histogram expected for 20 such spectra for $\langle x_{\rm HI} \rangle$ = 0.35 (black), 0.22 (blue), 0.05 (cyan), and 0 (magenta). In generating this figure, we use the same ensemble of mock spectra as in §2.7 and §2.7, except with their spectral resolution and bin size modified as mentioned. We maintain the requirement that $\langle F \rangle = 0.1$.

This figure qualitatively agrees with Fig. 2.3, where noiseless spectra with finer spectral resolution were used, but shows a shift toward larger L due to smoothing the spectra. Additionally, the ionization states are not as easily distinguishable as in Fig. 2.3, with the $\langle x_{\rm HI} \rangle$ = 0.05 distribution looking practically identical to the fully ionized scenario. However, for the other neutral fractions considered, the situation looks very encouraging. The distributions for $\langle x_{\rm HI} \rangle$ = 0.22 and 0.35 show a more gradual decline toward large L than the fully ionized case and also reveal the clear emergence of a bimodal distribution. Additionally, the largest dark gaps in these ionization states are roughly twice as large as in the fully ionized case.

2.8 Forecasts

Having discussed the results of the proposed stacking approaches applied to realistic mock spectra, we now consider the ability of these methods to constrain the ionization state of the $z \sim 5.5$ IGM. Specifically, in this section we focus on the ability of each method to rule out the hypothesis of a fully ionized IGM.

In both the case of the HI damping wing and deuterium absorption feature, we would like to compare models representing different ionization states and estimate the $\Delta\chi^2$ between $\langle x_{\mathrm{HI}} \rangle \neq 0$ models and the fully ionized model, assuming a reasonable number of spectra. Let $F_{\langle x_{\mathrm{HI}} \rangle}(\Delta v)$ denote the mean behavior for a model with given neutral fraction, $\langle x_{\mathrm{HI}} \rangle$, as a function of stacked velocity separation and let $F_{\mathrm{ion}}(\Delta v)$ denote the mean behavior of the ionized model, also as a function of stacked velocity separation. The precise definitions of what is meant by behavior will be discussed later in this section. In this case, the $\Delta\chi^2$ value between two models can be calculated by

$$\Delta\chi^2_{\langle x_{\mathrm{HI}} \rangle} = \Delta F_{\langle x_{\mathrm{HI}} \rangle} \cdot C^{-1} \cdot \Delta F^{\mathrm{T}}_{\langle x_{\mathrm{HI}} \rangle} \tag{2.9}$$

where C is the covariance matrix of the $\langle x_{\mathrm{HI}} \rangle$ model, representing the correlation between stacked pixels, and $\Delta F_{\langle x_{\mathrm{HI}} \rangle}(\Delta v) \equiv F_{\mathrm{ion}}(\Delta v) - F_{\langle x_{\mathrm{HI}} \rangle}(\Delta v)$, with $\Delta F^{\mathrm{T}}_{\langle x_{\mathrm{HI}} \rangle}$ denoting its transpose. For simplicity, rather than estimating the full covariance matrix and its inverse, we approximate pixels at sufficiently wide separations as independent. We then coarsely sample the pixels – on the scale where they can be well approximated as independent – and assume a diagonal covariance matrix for the coarsely sampled pixels. Specifically, we estimate $\Delta\chi^2_{\langle x_{\mathrm{HI}} \rangle}$ by simply adding up the squared statistical significance of each coarsely-sampled bin, $\left[\Delta F_{\langle x_{\mathrm{HI}} \rangle}(\Delta v_i) / \sigma_{\langle x_{\mathrm{HI}} \rangle}(\Delta v_i) \right]^2$, where $\sigma_{\langle x_{\mathrm{HI}} \rangle}(\Delta v_i)$ is the standard deviation of $F_{\langle x_{\mathrm{HI}} \rangle}(\Delta v_i)$.

Deuterium

Perhaps it is best to consider the case of the deuterium absorption feature first. In the case of a fully ionized IGM, the transmission looking blueward and redward from absorption systems should be symmetric on average, with excess blueward absorption only occurring when the IGM is significantly neutral. Therefore, we may calculate the $\Delta\chi^2_{\langle x_{\mathrm{HI}}\rangle}$ between stacked transmission looking redward ($F_{\langle x_{\mathrm{HI}}\rangle,\mathrm{red}}(v)$) and blueward ($F_{\langle x_{\mathrm{HI}}\rangle,\mathrm{blue}}(v)$) from plausibly neutral absorption systems for each ionization state $\langle x_{\mathrm{HI}}\rangle$ to estimate our ability to rule out the hypothesis of a fully ionized IGM in each case.

Thus, in the context of Eq. 2.9, we have

$$\Delta F_{\langle x_{\mathrm{HI}}\rangle}(\Delta v) \equiv F_{\langle x_{\mathrm{HI}}\rangle,\mathrm{red}}(\Delta v) - F_{\langle x_{\mathrm{HI}}\rangle,\mathrm{blue}}(\Delta v) \tag{2.10}$$

$$C_{ij}^{-1} = \delta_{ij}/\sigma^2_{\langle x_{\mathrm{HI}}\rangle,\mathrm{blue}}(v_i) \tag{2.11}$$

where $\sigma_{\langle x_{\mathrm{HI}}\rangle,\mathrm{blue}}(v_i)$ is the standard deviation of the stacked transmission blueward of plausibly neutral absorption systems, assuming a given number of spectra, and we have assumed that we have already resampled $\Delta F_{\langle x_{\mathrm{HI}}\rangle}(v)$ at sufficient velocity separations such that neighboring bins can be approximated as independent. At this point, the only missing ingredient is the minimum separation between two stacked pixels for them to be considered independent. We calculate the correlation function between stacked pixels in Ly β, and find that the correlation has a width of FWHM $\approx$ 80km/s and, as such, we do not expect to get more than one independent bin within the scale of the deuterium feature. Therefore, a rough estimate of the $\Delta\chi^2_{\langle x_{\mathrm{HI}}\rangle}$ value obtainable in each ionization state can be estimated simply by the peak value in the "significance curves" in Fig. 2.10. Thus, if the underlying neutral fraction of the IGM is $\langle x_{\mathrm{HI}}\rangle = 0.22$ (0.35), then we expect to be able to rule out a fully ionized IGM with $\sim 3\sigma$ ($\sim 3.7\sigma$) confidence, assuming 20 HIRES/MIKE spectra with signal to noise of 30 per pixel at the continuum. Unfortunately, we do not expect to be able to rule out the hypothesis of a fully ionized IGM if the underlying neutral fraction is $\langle x_{\mathrm{HI}}\rangle \lesssim 0.05$.

HI Damping Wing

Assessing the statistical significance with which we can observe the HI damping wing is slightly more complicated than the deuterium case since the test for its detection is not as simple. When faced with actual spectra, we would look for the presence of significant and extended absorption outside of large absorption systems compared to that outside of small absorption systems.

Therefore, the behavior we would like to compare in each case is the stacked transmission outside of plausibly neutral absorption systems ($f_{\text{large}}(\Delta v)$) and the transmission outside of likely ionized absorption systems ($f_{\text{small}}(\Delta v)$). Let us denote

$$F(\Delta v) \equiv f_{\text{small}}(\Delta v) - f_{\text{large}}(\Delta v) \tag{2.12}$$

as the difference in these stacked transmissions where $F_{\langle x_{\text{HI}} \rangle}(\Delta v)$ and $F_{\text{ion}}(\Delta v)$ represent this behavior for the ionization state with neutral fraction $\langle x_{\text{HI}} \rangle$ and the fully ionized state, respectively. Thus, in the context of Eq. 2.9, we have

$$\Delta F_{\langle x_{\text{HI}} \rangle}(\Delta v) = F_{\text{ion}}(\Delta v) - F_{\langle x_{\text{HI}} \rangle}(\Delta v) \tag{2.13}$$

$$C_{ij}^{-1} = \delta_{ij}/\sigma^2_{F_{\langle x_{\text{HI}} \rangle}}(v_i) \tag{2.14}$$

where $\sigma_{F_{\langle x_{\text{HI}} \rangle}}(v_i)$ denotes the standard deviation of $F_{\langle x_{\text{HI}} \rangle}(v)$ at v_i. The resulting $\sqrt{\Delta \chi^2}$ value indicates the expected significance with which we could rule out a *fully ionized* IGM if the neutral fraction were, in fact, $\langle x_{\text{HI}} \rangle$. Again, for Eq. 2.14, we have assumed that $\Delta F_{\langle x_{\text{HI}} \rangle}(\Delta v)$ has been resampled at velocity separations such that the pixels can be treated as independent. We find that the correlation function between pixels of stacked transmission in the Ly α forest within the scale of the HI damping wing has FWHM ≈ 100km/s. While this scale is large, the excess absorption due to the presence of damping wing absorption leaves a feature extending $\gtrsim 3000$km/s, leaving us with $\gtrsim 30$ independent bins within the scale of the feature.

In this manner, we are able to calculate a rough estimate for the $\Delta\chi^2$ values for the ionization states considered thus far. Assuming the same type of spectra as in Fig. 2.6, namely 20 HIRES spectra with signal to noise in the continuum of 10 per pixel, we find that if the IGM is, in fact, 5%, 22%, or 35% neutral, then we should be able to rule out a fully ionized IGM at 5.3σ, 19.2σ, or 26.3σ, respectively. In the case of $\langle F \rangle = 0.05$, this reduces to 14.8σ, 8.7σ, and 2.2σ, respectively.[1] While we are only aware of ~ 10 such spectra that exist at the moment, we still regard this estimate as somewhat conservative. We found that excess stacked absorption due to the damping wing extends thousands of km/s, and therefore it is not necessary to have the state-of-the-art in spectral resolution to measure it. Especially with such extended correlation among neighboring pixels, it is unclear how much is gained by resolution improvements beyond ~ 100km/s.

2.9 Conclusion

In this work, we developed empirical tests of the possibility that the Epoch of Reionization is not yet complete by $z \sim 5.5$. Specifically, we proposed three measurements that can be made with existing, and future, high-redshift quasar spectra in order to investigate this region of reionization history parameter space.

First, we discussed using the dark gap size distribution in quasar spectra as a means of constraining the $z \sim 5.5$ neutral fraction. We find that not only do the typical sizes of dark gaps increase with neutral fraction but that the *shape* of the size distribution is also sensitive to the neutral fraction. Specifically, the presence of dark gaps sourced by significantly neutral hydrogen islands introduces a bimodality in the dark gap size distribution. We find that this bimodality should be observable at $z \sim 5.5$, provided that $\langle x_{\mathrm{HI}} \rangle \gtrsim 0.2$, and should not be affected by continuum fitting errors.

Next, we proposed a method for searching for hydrogen damping wing absorption by strategically stacking regions of transmission in the Ly α forest. Specifically, we searched for

excess absorption in stacked transmission outside of plausibly neutral regions compared to that outside of likely ionized regions. We found that the presence of the hydrogen damping wing will result in excess absorption extending $\sim 5000 \mathrm{km/s}$ past ionization boundaries of neutral regions. Furthermore, this excess absorption should be detectable with $\gtrsim 5.3\sigma$ statistical significance for $\langle x_{\mathrm{HI}} \rangle \gtrsim 0.05$, using 20 HIRES-style spectra with a signal-to-noise value per pixel of 10 at the continuum.

Lastly, we proposed a similar stacking measurement utilizing the Ly β forest in order to search for deuterium absorption associated with significantly neutral hydrogen islands at $z \sim 5.5$. We proposed searching for this feature by looking for excess absorption in stacked Ly β transmission blueward of plausibly neutral regions compared to the corresponding redward transmission. We find that this feature should be observable in principle but will likely require additional high-resolution spectra in order to be detected. Specifically, we find that the feature should be observable at $z \sim 5.5$ with $\sim 3\sigma$ ($\sim 3.7\sigma$) confidence using 20 HIRES-style spectra with a signal-to-noise value per pixel of 30 at the continuum if $\langle x_{\mathrm{HI}} \rangle = 0.22$ (0.35). While we are not aware of this many available spectra with such specifications, this provides motivation for acquiring such spectra in the future, possibly through the follow-up observation of SDSS quasars.

While we have taken many steps to ensure that the analysis of mock spectra presented in this work is realistic, there are still additional complexities that will be faced when one is presented with actual spectra. For example, we treat all portions of our spectra as being at $z = 5.5$ when, in reality, the redshift will evolve along the lines of sight. In addition, we ignored spatial fluctuations in the UV radiation field and in the temperature density relation. Additional work will certainly be required to definitively interpret future measurements along the lines we suggest here. However, we believe the signatures explored here are well-worth further investigation and should ultimately improve our understanding of the reionization history of the IGM.

Appendix A: Contamination from DLAs?

A potential concern is that damping wings from super Lyman-limit systems and damped Ly-α absorbers (DLAs) might produce "false positives" and contaminate our search for diffuse neutral islands. Since DLAs and super Lyman-limit systems are mostly associated with galaxies and the circumgalactic medium (see **?** for a review), we would like to distinguish these absorbers from the more diffuse and spatially extended islands of neutral hydrogen that are the subject of our search. In addition, note that it is difficult to fully resolve and model high column density absorbers in cosmological simulations (e.g. **?** and references therein) – especially given our present aim of capturing the large-scale features of reionization – and so the impact of these systems is not captured in our present modelling.

Fortunately, we don't expect these dense absorbers to be a big contaminant, provided we make use of the Ly-β forest – which helps owing to the lower cross section in the wing of the line (compared to Ly-α) – and confine our search to fairly extended neutral islands. The Ly-β line profile for a high column density absorber can be approximated by a Lorentzian, so that the optical depth at velocity offset Δv is:

$$\tau_{\beta,\mathrm{DLA}}(\Delta v) = N_{\mathrm{HI}} \frac{\sigma_{\beta,0}}{\pi} \frac{R_\beta}{(\Delta v/c)^2 + R_\beta^2}. \tag{2.15}$$

For comparison, a fully neutral and isolated absorber of co-moving length L_{neut} produces saturated Ly-β absorption over a velocity extent slightly larger than $\Delta v_{\mathrm{neut}} = H(z)L_{\mathrm{neut}}/(1+z)$. We can then determine the column density required for a DLA to produce as long a saturated region in the Ly-β forest as produced by a neutral island of length L_{neut}. We consider a DLA to produce saturated absorption at velocity separations where $\tau_{\beta,\mathrm{DLA}} \geq 3$. Provided the extent of the absorber is large enough that $\Delta v_{\mathrm{neut}}/c \gg R_\beta$ (which is a good approximation for the extended neutral islands of interest), this critical column density,

$N_{\mathrm{HI,crit}}$, is given by:

$$N_{\mathrm{HI,crit}} = 7.2 \times 10^{21} \mathrm{cm}^2 \left[\frac{\tau_{\beta,\mathrm{DLA}}}{3}\right] \left[\frac{1+z}{6.5}\right] \left[\frac{L_{\mathrm{neut}}}{3.8\mathrm{Mpc/h}}\right]^2.$$

(2.16)

The fiducial value of L_{neut} in the above equation corresponds to $\Delta v_{\mathrm{neut}} = 500$ km/s – this is the minimum saturated stretch included in our stacks when we search for neutral regions (see §2.6). The column density $N_{\mathrm{HI,crit}}$ required for a DLA to produce this much saturated absorption is quite large, and the abundance of DLAs with column densities larger than $N_{\mathrm{HI,crit}}$ is very small.

Quantitatively, taking the Gamma function fit to the column density distribution of DLAs from **?**)[1] (which accounts for the sharp cutoff in the observed abundance of DLAs at high column densities), we find that the number of DLAs with $N_{\mathrm{HI}} \geq N_{\mathrm{HI,crit}}$ is only $d\mathcal{N}(> N_{\mathrm{HI,crit}})/dz = 1.5 \times 10^{-3}$. For reference, the redshift extent of the forest between the Ly-α and Ly-β emission line at these redshifts is roughly $\Delta z \approx 1$, and so such high column density DLAs should be exceedingly rare. Since $N_{\mathrm{HI,crit}}$ is only a little smaller than the exponential cut-off in the column density distribution function, the results are rather sensitive to the precise choice of $N_{\mathrm{HI,crit}}$. Given that smaller column-density DLAs might still leak into our stack if they happen to be next to saturated ionized regions, it is worth checking this dependence. However, even choosing $N_{\mathrm{HI,crit}} = 2 \times 10^{20}$ cm^2 yields only $d\mathcal{N}/dz = 0.43$, which is still smaller than the abundance of neutral islands we seek to detect. From these estimates, we expect very minimal contamination from DLAs leaking into our stacked sample of possible neutral regions. Note also that deuterium Ly-β absorption from these high column density absorbers will be in the saturated part of the HI Ly-β line, and

---

[1]This is for the case where we do not attempt to further optimize the analysis for the decrease in transmission. It is possible that further gains could be made, with Fig. 2.7 representing a best-possible-case scenario.

[1]Specifically, we use their highest redshift bin fit, which includes DLAs between redshifts $3.5 \leq z \leq 5.5$.

so DLAs should not contaminate our search for the deuterium signature of neutral islands either.

A separate possible worry is that DLAs could instead contaminate our sample of *small* saturated regions that we use for comparison purposes (as described in §2.6). Our small saturated sample is meant to reflect absorption around saturated yet ionized regions, and so should not contain significant damping wing absorption. In principle, wings from any DLAs in *this* sample could influence the transmission around the small saturated regions. It seems unlikely that this is a significant worry, since the saturated yet ionized regions are likely vastly more abundant than even the small column density DLAs and super Lyman-limit systems. In addition, we can simply inspect the profile of the small saturated sample to see whether it shows any hint of damping wing absorption that might arise from either small isolated neutral regions or DLAs.

Although contamination from DLAs does not appear to be a big worry for our tests, a more detailed examination would certainly be warranted if possible neutral islands are discovered in real data. We may also be able to remove DLA-contaminated regions by flagging spectral regions in the Ly-α and Ly-β forest that have the same redshift as strong metal absorbers, which generally accompany DLAs (see e.g. **?**).

Appendix B: Further Utilizing the Ly β Forest

In order to infer the presence of the HI damping wing, we would like to compare the stacked transmission outside of plausibly neutral absorption systems to what that transmission would have been in the absence of the damping wing. Up to this point, we have been using the stacked transmission outside of *small* absorption systems as a proxy for the latter quantity. From there, we argued that any extended excess absorption outside of large, plausibly neutral absorption systems compared to small, likely ionized absorption systems is indicative of the presence of damping wing absorption.

However, we do have another handle on what transmission would be like in the absence of the HI damping wing and that is the transmission in the Ly β forest. As discussed in §2.5, the HI damping wing should be significantly reduced in the Ly β forest compared to the Ly α forest. Specifically, we saw that the damping wing optical depth in Ly β falls to less than one at velocity separations $\gtrsim 25$km/s from neutral gas. Therefore, at separations greater than this, stacked transmission in the Ly β forest should provide information on what the shape of the Ly α transmission would have been in the absence of the damping wing, with foreground Ly α absorption only altering the stacked Ly β transmission by an overall constant $\langle F_\alpha(z_\alpha) \rangle$. Using information from stacked Ly β transmission has the appeal that it does not require using physically different regions of space in order to estimate the damping-wing-less transmission outside of selected plausibly neutral absorption systems. This provides protection from problems arising from unanticipated differences between the small, likely ionized absorption systems and the large, plausibly neutral absorption systems.

Thus, we would like to find a way to estimate the Ly α transmission in the absence of the damping wing by using only the Ly β transmission. In principle, this can be done by using simulations to model the relationship between the two and generating a (ionization-state-dependent) mapping that takes a measurement of stacked Ly β transmission outside of large absorption systems and maps it to an estimate of the damping-wing-less Ly α transmission in the same regions. From there, the ratio of the stacked Ly α transmission to this estimate of the damping-wing-less Ly α transmission would leave us with an estimate of $e^{-\tau_{\mathrm{DW}}(v)}$. In the left-hand panel of Fig. 2.12, we show the recovered $e^{-\tau_{\mathrm{DW}}(v)}$ curve after applying this approach to each of the ionization states considered thus far, and then normalizing each curve to peak at 1. Specifically, a mapping between stacked Ly β transmission and stacked damping-wing-less Ly α transmission for each ionization state was generated using a large ensemble of mock spectra and then applied to groups of 20 spectra. The error bars in the figure show the scatter in the estimated damping wing absorption between realizations of 20 spectra. For ease of viewing, we show only the error bars for $\langle x_{\mathrm{HI}} \rangle = 0$ and 0.35. This

figure demonstrates that the approach works well and recovers a damping wing shape for an IGM with $\langle x_{\mathrm{HI}} \rangle \gtrsim 0.05$ (in the absence of noise).

A few things are worth pointing out about this process. First, the recovered damping wing profiles are only useful to the extent that they provide confidence that we are, in fact, observing neutral hydrogen in the IGM. The stacked profile of the HI damping wing is a complicated entity and, as such, we *do not* expect to be able to, for example, fit the recovered curves to Eq. 2.6 and estimate $\langle x_{\mathrm{HI}} \rangle$. Secondly, it is comforting to note that not only is no damping shape recovered in the case of $\langle x_{\mathrm{HI}} \rangle = 0$, but even if a mapping corresponding to a significantly neutral IGM is applied to a measurement of a fully ionized IGM, we do not recover a damping wing shape. Therefore, we do not expect this approach to yield false positives. Lastly, this process relies on simulations in order to map the stacked Ly β transmission to damping-wing-less Ly α transmission and is therefore somewhat model-dependent. However, we do not expect the specifics of reionization to significantly impact this mapping and we are also not interested in the fine details of the results here. We are primarily interested in whether damping wing absorption can be measured *at all* in the case of a somewhat neutral IGM and, as such, we are comfortable with this level of model dependence.

Finally, we find that this mapping is relatively simple. Namely, for velocity separations $\gtrsim 100 - 200$km/s, the stacked Ly β transmission and the stacked damping-wing-less Ly α transmission differ by roughly a constant multiplicative factor. Thus, in aiming to recover the *shape* of the stacked damping wing absorption, it appears to be a very good approximation to simply divide the stacked Ly α transmission by the stacked Ly β transmission. In the right-hand panel of Fig. 2.12 we simply take groups of 20 spectra and divide their stacked Ly α transmission by their stacked Ly β transmission (outside of large absorption systems) and give the result unity amplitude. Qualitatively, the results look very similar to those obtained from the mapping procedure (shown on the left-hand side) but are without any model-dependence. Additionally, we again find that, in the case of a fully ionized IGM,

we do not recover a damping wing shape. Thus, this provides another check which may be performed with actual spectra in order to bolster confidence that a damping wing is in fact being observed.

A potential concern for our $\text{Ly}\,\alpha$ stacking approach in general could be that, while we make the approximation that ionized regions are exposed to a uniform ionizing background, the ionizing background will in fact be fluctuating spatially. It is then possible that, in scenarios where the ionizing background is weaker closer to the stacking location and stronger farther from the stacking location, an extended recovery could be imprinted on the stacked transmission despite the IGM being fully ionized. If one were not careful, and if these spatial fluctuations occurred on scales comparable to the damping wing feature, a false detection could be possible. One tool we have to protect against this is the fact that the scale of the damping wing is significantly smaller in $\text{Ly}\,\beta$ than in $\text{Ly}\,\alpha$. Therefore, any extended recovery in stacked transmission which occurs over similar scales in $\text{Ly}\,\alpha$ and $\text{Ly}\,\beta$ is unlikely to be caused by the damping wing.

Appendix C: Extended damping wing Absorption from Correlated HI Islands

As mentioned in §2.7, and seen in Fig. 2.6, 2.7, & 2.8, stacked $\text{Ly}\,\alpha$ transmission outside of large saturated regions in a significantly neutral IGM displays excess absorption extending significantly past the scale of an isolated damping wing. To explain this, we seek to model the expected transmission outside of a neutral region, incorporating the correlation between the neutral region at the origin and neighboring neutral regions. In order to simplify the calculation, while capturing the main effect, we ignore correlations between the neighbors themselves – i.e., we only include the correlation between the neutral region at the origin and the neighbors and ignore inter-neighbor correlations.

Ignoring correlations between the neighboring neutral regions, we can approximate them as following a Poisson distribution and consider the total absorption contributed by these neutral islands or "clouds" following (**?**). Suppose that on average m clouds contribute to the absorption at a given region of the spectrum. Let $F_k \equiv e^{-\tau_1} e^{-\tau_2} \cdots e^{-\tau_k}$ denote the transmission when k clouds reside along the line of sight and impact the given spectral region, with τ_i being the optical depth of the ith cloud. If we allow the clouds to be placed independently and if they have equal optical depths, then:

$$\langle F_k \rangle \equiv \left\langle e^{-\tau_1} e^{-\tau_2} \cdots e^{-\tau_k} \right\rangle = \left\langle e^{-\tau_1} \right\rangle \left\langle e^{-\tau_2} \right\rangle \cdots \left\langle e^{-\tau_k} \right\rangle = \left(e^{-\tau} \right)^k. \tag{2.17}$$

Using this expression, we can calculate the ensemble-averaged transmission by averaging over all the possible numbers of intervening clouds:

$$\langle F \rangle = \sum_{k=0}^{\infty} \text{Pois}(k; m) \langle F_k \rangle = \sum_{k=0}^{\infty} \frac{e^{-m}}{k!} m^k \left\langle e^{-\tau} \right\rangle^k = e^{-m} \sum_{k=0}^{\infty} \frac{(m e^{-\tau})^k}{k!} \tag{2.18}$$

$$= e^{-m} e^{m e^{-\tau}} = e^{-m \left(1 - e^{-\tau} \right)}. \tag{2.19}$$

Let us define the quantity τ_{eff} as

$$e^{-m \left(1 - e^{-\tau} \right)} \equiv e^{-\tau_{\text{eff}}} \tag{2.20}$$

$$\tau_{\text{eff}} \equiv m \left(1 - e^{-\tau} \right). \tag{2.21}$$

We now have the absorption from neighboring clouds, characterized by the parameter τ_{eff}.

We just need to adapt this slightly to the problem at hand. Suppose that – with certainty – there is a neutral region located at $v = 0$ and let us consider the excess absorption, above random, contributed by neighboring neutral regions. First, the optical depth at $v = \Delta v$ that is contributed by a neighboring cloud located at $v = v'$ will depend on $|\Delta v - v'|$: clouds closer to $v = \Delta v$ will have larger optical depths at that corresponding frequency. We can account for this by substituting $\tau \to \tau(|\Delta v - v'|)$, according to Eq. 2.6. Next, the expected

number of HI islands in a region with velocity extent dv' nearby our stacking location can be approximated as

$$m \approx dv' \langle n_{\mathrm{HI}} \rangle \left(1 + \xi_{\mathrm{HI,HI}}(v') \right) \tag{2.22}$$

where $\langle n_{\mathrm{HI}} \rangle$ is the average number of HI islands per interval dv' and $\xi_{\mathrm{HI,HI}}(v')$ is the correlation function between the centers of neutral regions separated by v'. From here, we can model the effective optical depth at a given velocity separation due to neighboring HI islands, $\tau_{\mathrm{eff}}(\Delta v)$, as

$$\tau_{\mathrm{eff}}(\Delta v) = \int dv' \langle n_{\mathrm{HI}} \rangle \left(1 + \xi_{\mathrm{HI,HI}}(v') \right) \left[1 - e^{-\tau(|\Delta v - v'|)} \right]. \tag{2.23}$$

In other words, the excess effective optical depth from neighboring systems involves the convolution of the absorption profile around each region with the correlation function of the neutral regions. This is analogous to the "two-halo" term in the halo model (e.g. **?**).

Thus, the model for the overall stacked transmission outside of neutral regions, also incorporating the damping wing from the central neutral region, becomes:

$$\langle F \rangle (\Delta v) = e^{-\tau_{\mathrm{DW}}(\Delta v)} e^{-\tau_{\mathrm{eff}}(\Delta v)}. \tag{2.24}$$

This model requires two inputs. First, it requires the correlation function between the centers of neutral regions, $\xi_{\mathrm{HI,HI}}(v')$, which can be calculated from a model of the underlying ionization field. Second, the optical depth profile for neutral regions, $\tau(|\Delta v - v'|)$, is a function of the size of the neutral regions, per Eq. 2.6. While the neutral regions in the mock spectra take on a range of sizes, we make the simplifying approximation here – but not in the body of this paper – that the neutral regions at a given neutral fraction have one typical size and denote this L_{typical} with a corresponding extent in velocity space v_{ext}. This effectively results in the optical depth profile of an individual neutral island in the right hand side of Eq. 2.23 being described by a piecewise function

$$\tau_{\mathrm{DW}}(\Delta v) = \begin{cases} \infty & \text{if } |\Delta v| < v_{\mathrm{ext}}/2 \\ \dfrac{\tau_{\mathrm{GP}} R_\alpha c}{\pi} \left[\dfrac{1}{\Delta v - v_{\mathrm{ext}}/2} - \dfrac{1}{\Delta v + v_{\mathrm{ext}}/2} \right] & \text{otherwise.} \end{cases} \tag{2.25}$$

Next, we would like to compare this model against results using mock spectra. We do this by first generating mock spectra which *only include absorption from neutral islands*, since this is the only type of absorption incorporated in our model, and stack these mock spectra at the HI/HII boundaries. To be clear, while the model curve described above adopted a fixed L_{neut} for the purpose of calculating a τ_{eff}, the mock spectra here are generated using the same simulated ionization fields as throughout the rest of the paper, with a wide range of sizes for the underlying neutral regions.

To obtain a model for the stacked transmission, we first calculate the correlation function between the centers of neutral regions using the mock underlying ionization fields and also choose a value for L_{typical} to be used in the optical depth profile. Additionally, in Eq. 2.23, the $(1 + \xi_{\text{HI,HI}}(v'))$ term effectively breaks our integral into two pieces: the first representing the mean absorption from neutral regions and the second representing the excess or reduced absorption at $v = \Delta v$ due to the clustering of neutral islands. For our case, we are only concerned with the *excess* absorption, so we make the replacement $(1 + \xi_{\text{HI,HI}}(v')) \to \xi_{\text{HI,HI}}(v')$.

Therefore, by providing a value for L_{typical} and measuring $\xi_{\text{HI,HI}}(v')$, we can get a estimate for the mean transmission outside of neutral regions which incorporates absorption from spatially-correlated neighboring regions. In the left panel of Fig. 2.13, we plot an example of this for $\langle x_{\text{HI}} \rangle = 0.22$. We show the modelled damping wing absorption from the central neutral region in blue, the modelled absorption from neighboring neutral islands and their damping wings in cyan, and the product of these in black. For comparison, we show the stacked transmission in the mock spectra in magenta, shifted by $v_{\text{ext}}/2$ to account for stacking occurring at HI/HII boundaries instead of at the center of neutral regions. All curves have been divided by the mean transmission. After taking $L_{\text{typical}} = 3.2 \text{ Mpc}/h$, we find good agreement between the above model and the stacked transmission. The precise agreement should be taken with a grain of salt, since the model makes several simplifying assumptions, especially that the neutral regions have a fixed size. However, the model

does demonstrate that clustered neutral islands should lead to extended excess absorption, significantly beyond the scale of an individual damping wing.

In the right panel of Fig. 2.13, we show the comparison between the stacked transmission (solid) and modelled transmission (dashed) for $\langle x_{\mathrm{HI}} \rangle = 0.35$ (black), 0.22 (blue), and 0.05 (cyan), where each curve has been multiplied by the mean transmission for clarity. In generating these plots, we have assumed $L_{\mathrm{typical}} = 2.5$ Mpc/h, 3.2 Mpc/h, and 0.75 Mpc/h for $\langle x_{\mathrm{HI}} \rangle = 0.35$, 0.22, and 0.05, respectively. We again find a very nice agreement between the modelled and stacked transmission, further confirming that spatially-correlated regions are indeed responsible for the significantly-extended excess absorption.
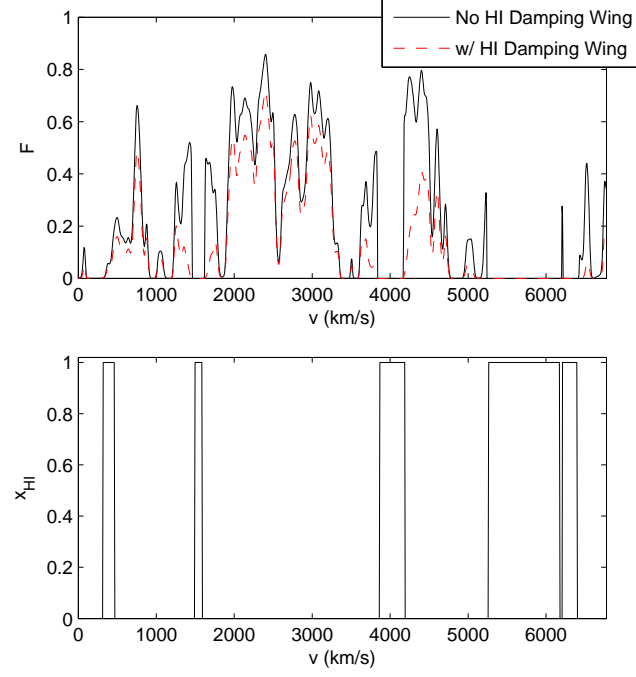
Figure 2.1: Example mock Ly α forest spectrum and corresponding neutral fraction. The top panel shows the Ly α transmission while the bottom panel is the neutral fraction along the line of sight, with ionized regions set to $x_{\mathrm{HI}} \approx 0$ for illustration. The black curve in the top panel shows the transmission through the forest when absorption due to the hydrogen damping wing is neglected, while the red curve includes damping wing absorption. The comparison illustrates that damping wing absorption has a prominent impact, but it is also clear that the presence of the damping wing will be hard to discern by eye. The line of sight is extracted from a model with $\langle x_{\mathrm{HI}} \rangle = 0.22$, but note that we have deliberately chosen a sightline with more neutral regions than typical.
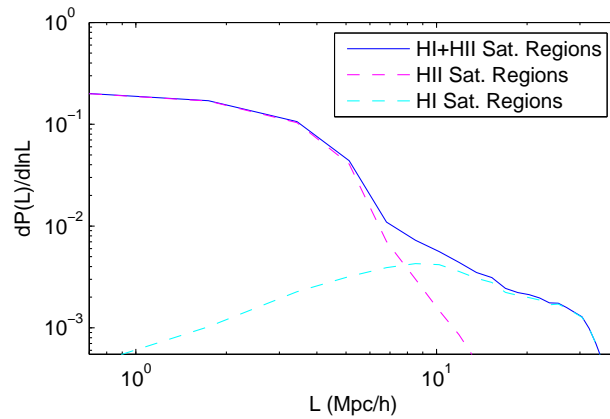
Figure 2.2: Dark gap size distribution for the $\langle x_{\mathrm{HI}} \rangle = 0.22$, $\langle F \rangle = 0.1$ model. The solid blue curve shows the total distribution of dark gaps from an ensemble of mock spectra, where the magenta (cyan) curve shows the same thing but for the dark gaps sourced by ionized (neutral) gas. Here, we have focused on dark gaps with $L > 0.75$ Mpc/h. This clearly demonstrates that neutral hydrogen is the dominant source of *large* dark gaps in our mock spectra, provided there is an appreciable neutral fraction.
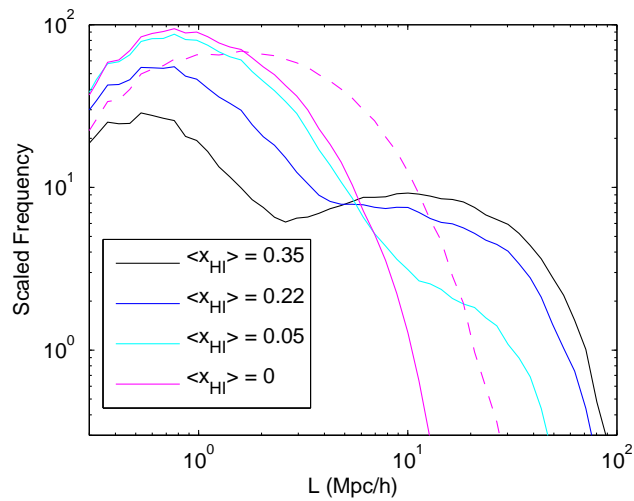
Figure 2.3: Large-length tail of the dark gap size histogram for $\langle x_{\mathrm{HI}} \rangle = 0$ (magenta), 0.05 (cyan), 0.22 (blue), and 0.35 (black) for the case when $\langle F \rangle = 0.1$. The y-axis is scaled to indicate the expected number of dark gaps obtainable from 20 spectra. Bins in this figure are spaced logarithmically. The dashed magenta line indicates the dark-gap size distribution in the fully ionized case when the true transmission is $\langle F \rangle = 0.03$, but continuum fitting errors result in a measured mean transmission of $\langle F_{\mathrm{meas}} \rangle = 0.1$.
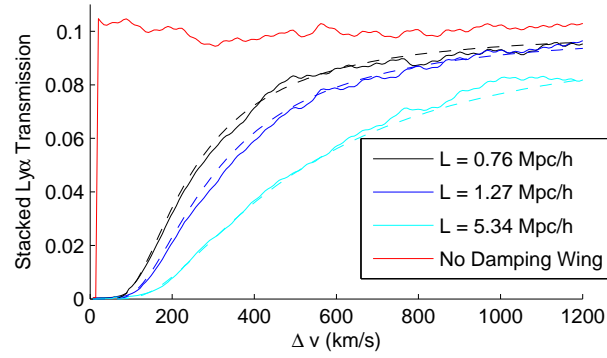
Figure 2.4: Stacking idealized Ly α spectra containing toy HI regions. The above figure shows the stacked transmission outside isolated HI regions with mean density and size $L = 0.76$ Mpc/h ($v_{\text{ext}} \approx 100$km/s), $L = 1.27$ Mpc/h ($v_{\text{ext}} \approx 170$km/s), and $L = 5.34$ Mpc/h ($v_{\text{ext}} \approx 700$km/s) shown in black, blue, and cyan, respectively. The solid red curve shows the stacked transmission outside of the same HI regions *neglecting* the damping wing, which will be the same on average in all cases. In generating these spectra, we assume $\langle F \rangle = 0.1$. In this greatly-idealized case, the presence of the hydrogen damping wing is seen clearly through extended excess absorption compared to the red curve. Furthermore, we can see that the excess absorption closely follows what we would expect analytically based on multiplying Eq. 2.6 by the overall mean transmission. In this figure, all stacking starts at HI/HII boundaries.

50
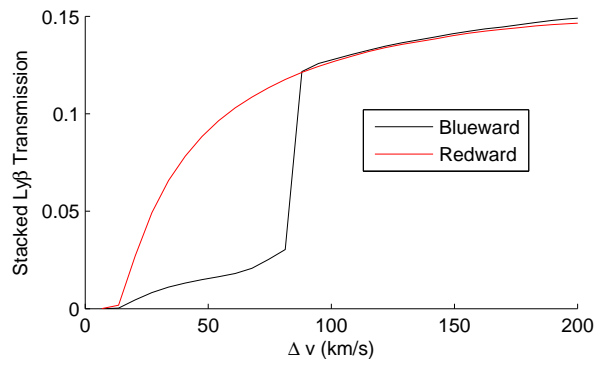
Figure 2.5: Presence of deuterium absorption revealed through stacking idealized $\text{Ly}\,\beta$ spectra containing toy neutral regions. The red and black curves show the stacked $\text{Ly}\,\beta$ transmission redward and blueward, respectively, of toy neutral regions of length $L = 5 \text{ Mpc}/h$ ($\approx 700\text{km/s}$) randomly inserted into many sightlines, with spectra generated assuming $\langle F_{\text{Ly}\alpha} \rangle = 0.1$. In each case, stacking begins at the underlying HI/HII boundary. We have also mimicked the effect of including foreground $\text{Ly}\,\alpha$ absorption by scaling the feature by the mean transmission in the foreground $\text{Ly}\,\alpha$ forest. This demonstrates that, at least in this idealized case, the presence of deuterium absorption can be easily seen out to $\sim 80\text{km/s}$ past the HI/HII boundaries.
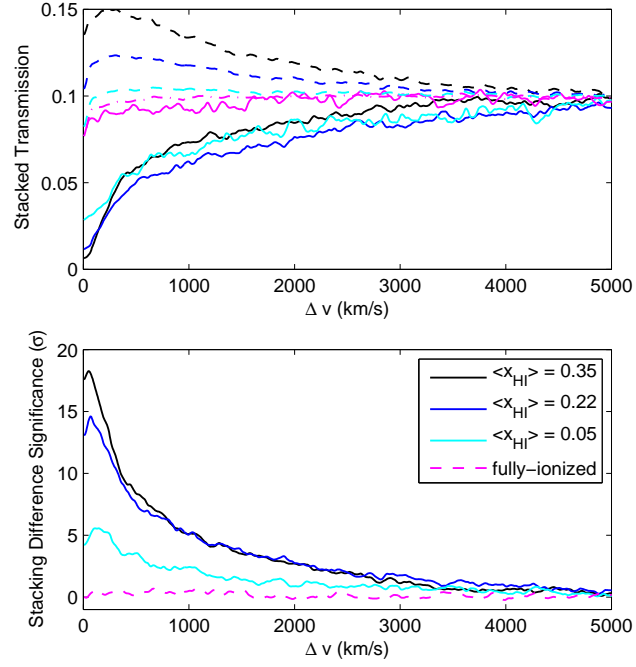
Figure 2.6: Ly α stacking results for various neutral fractions. The top panel shows the mean (noiseless) stacked transmission outside of large absorption systems (solid) and small absorption systems (dashed) in the Ly α forest for neutral fractions $\langle x_{\mathrm{HI}} \rangle = 0.35$ (black), 0.22 (blue), 0.05 (red), and 0 (magenta). The transmission here is estimated from a large ensemble of mock spectra to obtain a smooth estimate of the average transmission around saturated regions in each model. The bottom panel shows the statistical significance of the difference between the dashed and solid curves in the top panel assuming a sample of 20 spectra are used in the stacking process.
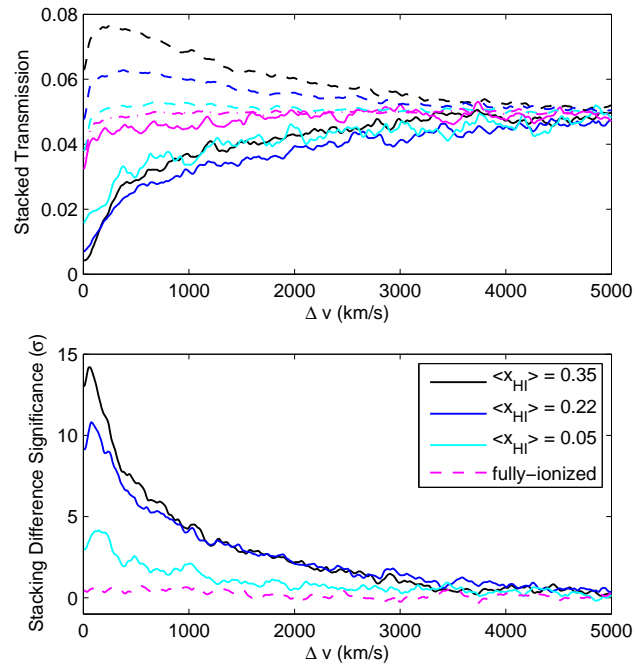
Figure 2.7: Ly α stacking results assuming $\langle F \rangle = 0.05$. The above panels are identical to those in Fig. 2.6 except that mock spectra have been generated assuming $\langle F \rangle = 0.05$.
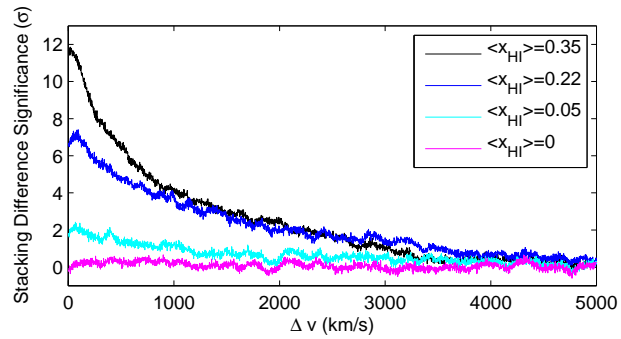
Figure 2.8: Results of Ly α stacking with HIRES-style spectra ($\langle F \rangle = 0.1$). The above panel is identical to the bottom panel in Fig. 2.6 except that the spectra have had the bin size and spectral resolution adjusted to match that of Keck-HIRES spectra. Additionally, we have added noise such that the spectra have a signal-to-noise value of 10 per pixel at the continuum.
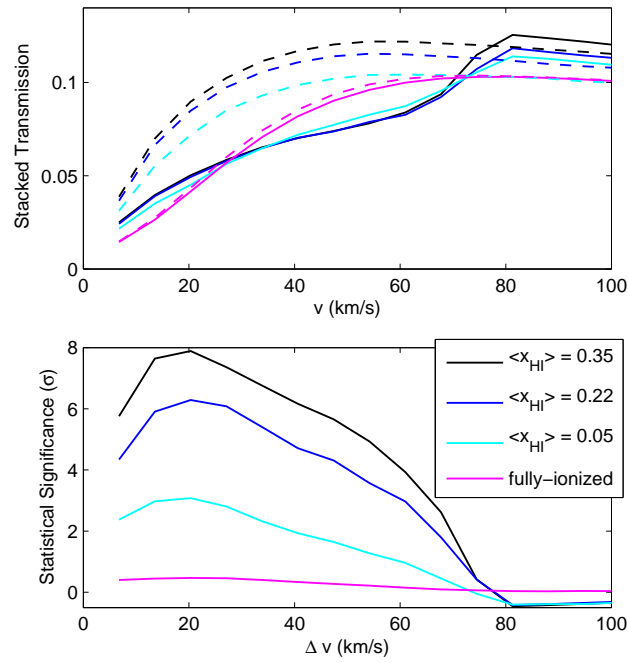
Figure 2.9: Deuterium Ly β stacking results for various neutral fractions. The top panel shows the mean ensemble-averaged noiseless stacked transmission moving blueward (solid) and redward (dashed) away from large absorption systems in the Ly β forest for neutral fractions $\langle x_{\mathrm{HI}} \rangle = 0.35$ (black), 0.22 (blue), 0.05 (cyan), and 0 (magenta). The bottom panel shows the excess blueward absorption in units of the standard deviation of the stacked redward transmission, assuming 20 spectra.
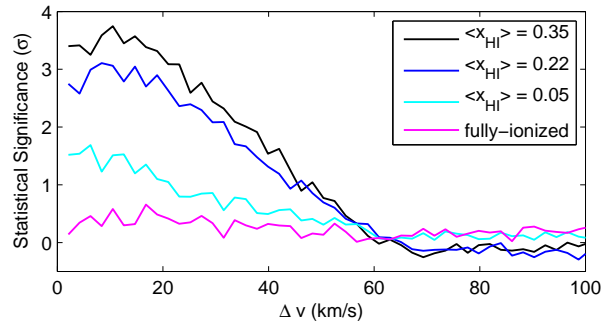
Figure 2.10: Results of Ly β stacking with HIRES-style spectra. The above panel is the same as in the bottom panel of Fig. 2.9, except that it is generated using HIRES-style spectra, with spectral resolution of FWHM = 6.7km/s and additive noise with signal to noise of 30 per 2.1 km/s pixel at the continuum.
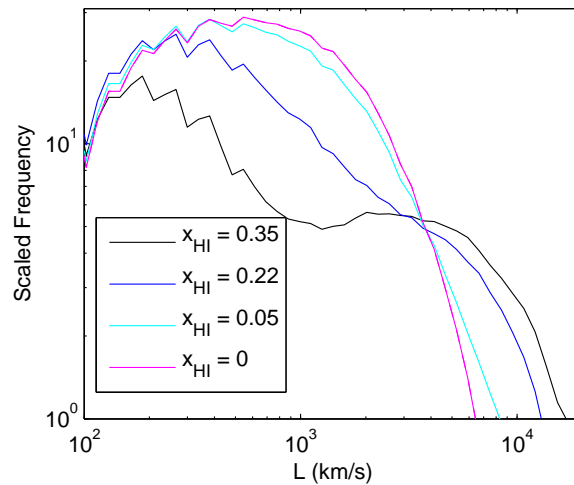
Figure 2.11: Mock dark gap size distribution. This figure is identical to Fig. 2.3 except that it uses spectra with spectral resolution FWHM = 100km/s, bin size $\Delta v_{\text{bin}} = 50$km/s, and a signal-to-noise ratio of 10 at the continuum. This figure shows the expected histogram of dark gap sizes using 20 spectra with $\langle x_{\text{HI}} \rangle = 0.35$ (black), 0.22 (blue), 0.05 (cyan), and 0 (magenta) at fixed $\langle F \rangle = 0.1$.
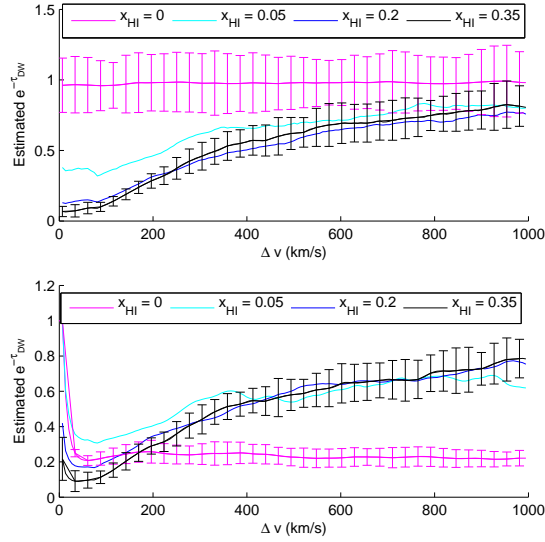
Figure 2.12: Using the Ly β forest to estimate damping-wing-less Ly α transmission. The above figure shows the estimated *shape* of stacked damping wing absorption for $\langle x_{\mathrm{HI}} \rangle = 0$ (magenta), 0.05 (cyan), 0.22 (blue), and 0.35 (black). The curves have been normalized to have their mean values peak at 1. Additionally, we show error bars for the fully ionized case and $\langle x_{\mathrm{HI}} \rangle = 0.35$ case which indicate the scatter in the curves between groups of 20 spectra. The left-hand plot is obtained by using a large ensemble of mock spectra to model a mapping between stacked Ly β transmission and stacked damping-wing-less Ly α transmission and then applying this to groups of 20 spectra. Meanwhile, the right-hand figure plots the ratio of the stacked Ly α flux to the stacked Ly β flux, providing a simplified estimate of the damping wing contribution to the absorption for each case.

57
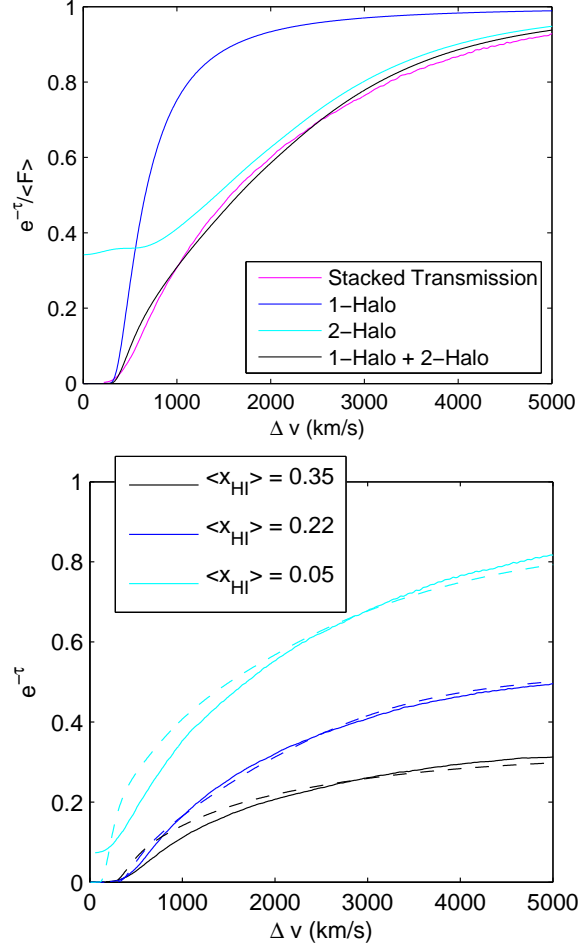
Figure 2.13: Model for the extended damping wing absorption. The left panel shows the components of our model for stacked transmission outside of a neutral region compared to the stacked transmission using mocked spectra (magenta) for $\langle x_{\mathrm{HI}} \rangle = 0.22$. We show the absorption due to the central neutral region (blue), average absorption due to neighboring, clustered neutral regions (cyan), and the product of the two transmissions (black). These are denoted in the legend as "1-Halo", "2-Halo", and "1-Halo + 2-Halo" in analogy with the halo model. In the right-hand panel, we show the comparison between the modelled transmission (dashed) and transmission from stacked mocked spectra (solid) for $\langle x_{\mathrm{HI}} \rangle = 0.35$ (black), 0.22 (blue), and 0.05 (cyan). The curves in the right-hand figure have been multiplied by the mean transmission (computed here ignoring resonant absorption for illustration). In this appendix, the stacking is done at the HI/HII boundaries and only damping wing absorption is incorporated to demonstrate the extended excess absorption owing to correlated neighboring systems.

2.10 Introduction

The Epoch of Reionization (EoR) is the time period when early generations of galaxies first turn on and gradually photoionize neutral hydrogen gas in the surrounding intergalactic medium (IGM). The IGM is expected to resemble a two phase medium during reionization. One phase consists of highly ionized regions, termed 'ionized bubbles', that form around clustered groups of ionizing sources, while the other phase is made up of intervening mostly neutral regions that shrink and eventually vanish as reionization progresses. A primary goal of reionization studies is to determine the size distribution and volume-filling factor of the ionized bubbles. This should, in turn, significantly improve our understanding of high redshift galaxy and structure formation. A wide variety of current observations have started to provide tantalizing hints regarding the timing and nature of the EoR (e.g., Fan et al. 14, Totani et al. 52, Dunkley et al. 13, Ouchi et al. 43, Bouwens et al. 4, Mortlock et al. 42, Zahn et al. 56, Schenker et al. 50), but we still await a more detailed understanding.

A highly anticipated way of improving our knowledge of the EoR is to directly detect intergalactic neutral hydrogen from the EoR using the redshifted 21 cm transition (e.g., Madau et al. 32, Zaldarriaga et al. 59, Furlanetto et al. 19). Indeed, several radio telescopes have been constructed, or are presently under construction, in effort to detect this signal, including the Giant Metrewave Radio Telescope (GMRT) (Paciga et al. 45), the Low Frequency Array (LOFAR) (Harker et al. 22), the Murchison Widefield Array (MWA) (Lonsdale et al. 31), and the Precision Array for Probing the Epoch of Reionization (PAPER) (Parsons et al. 46). This method provides the most direct, and potentially most powerful, way of studying reionization, but several challenges need first to be overcome. In particular, upcoming surveys will need to extract the faint cosmological signal in the presence of strong foreground emission from our own galaxy and extragalactic point sources, and to control systematic effects from the instrumental response, polarization leakage, calibration errors, and other sources of contamination (e.g., Liu et al. 30, Datta et al. 9, Harker et al. 22, Petrovic and Oh 48, Morales et al. 41, Parsons et al. 47). In addition, thermal noise will

prevent early generations of 21 cm experiments from making detailed maps of the reionization process. Instead, detections will mostly be of a statistical nature (McQuinn et al. 35). For example, a primary goal of these experiments is to measure the power spectrum of 21 cm brightness temperature fluctuations by binning together many individually noisy Fourier modes (Zaldarriaga et al. 59, Morales and Hewitt 40, Bowman et al. 5, McQuinn et al. 35).

It is unclear, however, how best to analyze the upcoming redshifted 21 cm data. Most previous work has focused only on the power spectrum of 21 cm brightness temperature fluctuations (e.g., Furlanetto et al. 17, Lidz et al. 28, Mesinger et al. 38). This statistic does not provide a complete description of the 21 cm signal from the EoR, which will be highly non-Gaussian, with large ionized regions of essentially zero signal intermixed with surrounding neutral regions. The power spectrum, and especially its redshift evolution, do encode interesting information about the volume-averaged ionized fraction and the bubble size distribution (e.g., Lidz et al. 28). However, these inferences are somewhat indirect and likely model dependent, and so it is natural to ask if there are more direct ways of determining the properties of the ionized regions.

The approach we explore here is to check whether it may be possible to directly identify ionized regions in noisy redshifted 21 cm observations by applying suitable filters to the noisy data. Our aim here is to blindly identify ionized bubbles across an entire survey volume, rather than to consider targeted searches around special regions, such as those containing known quasars (e.g., Wyithe and Loeb 54, Friedrich et al. 15). Since the 21 cm signal from reionization is expected to have structure on rather large scales – $\gtrsim 30\ h^{-1}$Mpc co-moving (Furlanetto et al. 18, Iliev et al. 24, Zahn et al. 57, McQuinn et al. 36) – it may be possible to make crude images of the large scale features even in the regime where the signal to noise per resolution element is much less than unity. Even if it is only possible to identify a few unusually large ionized regions in upcoming data sets, this would still be quite valuable. Any such detection would be straightforward to interpret, and would

open-up several interesting possibilities for follow-up investigations. Towards this end, we extend previous work by (10) and (11), who considered the prospects for detecting ionized regions using an optimal matched filter. A matched filter is constructed by correlating a known 'template' signal with a noisy data set in order to determine whether the template signal is present in the noisy data. Matched filters are used widely in astrophysics: to name just a few examples, matched filters are used to detect clusters in cosmic microwave background (CMB) data (Haehnelt and Tegmark 20), to identify galaxy clusters from weak lensing shear fields (e.g., Hennawi and Spergel 23, Marian et al. 34), and are central to data analysis efforts aimed at detecting gravitational waves (e.g., Owen and Sathyaprakash 44).

The outline of this paper is as follows. In §2.11 we describe the mock 21 cm data sets used in our investigations. We use the mock data to first consider the ability of future surveys to make maps of the redshifted 21 cm signal (§2.12). In §2.13, we then quantify the prospects for identifying individual ionized regions using a matched filter technique. In §2.14 and §2.15 we consider variations around our fiducial choice of reionization history and redshifted 21 cm survey parameters. We compare with previous related work in §2.16, and conclude in §2.17. Throughout we consider a ΛCDM cosmology parametrized by $n_s = 1, \sigma_8 = 0.8, \Omega_m = 0.27, \Omega_\Lambda = 0.73, \Omega_b = 0.046$, and $h = 0.7$, (all symbols have their usual meanings), consistent with the latest WMAP constraints from (25).

2.11 Method

Briefly, our approach is to construct mock redshifted 21 cm data sets and check whether we can successfully identify known 'input' ionized regions in the presence of realistic levels of instrumental noise and the degrading impact of foreground cleaning. Here we describe the ingredients of our mock data sets: our simulations of reionization and the 21 cm signal, our model for thermal noise, and our approach for incorporating the impact of foreground cleaning.

The 21 cm Signal

First, let us describe the underlying 21 cm signal and our reionization simulations. The 21 cm signal will be measured through its contrast with the cosmic microwave background (CMB). The brightness temperature contrast between the CMB and the 21 cm line from a neutral hydrogen cloud with neutral fraction x_{HI} and fractional baryon overdensity δ_ρ is (Zaldarriaga et al. 59):

$$\delta T_{\mathrm{b}} = 28 x_{\mathrm{HI}}(1 + \delta_\rho) \left(\frac{T_{\mathrm{S}} - T_\gamma}{T_{\mathrm{S}}}\right) \left(\frac{1 + z}{10}\right)^{1/2} \mathrm{mK}. \tag{2.26}$$

Here T_γ denotes the CMB temperature and T_{S} is the spin temperature of the 21 cm line. Here and throughout we neglect effects from peculiar velocities, which should be a good approximation at the redshifts and neutral fractions of interest (e.g., Mesinger and Furlanetto 37, Mao et al. 33). Furthermore, throughout we assume that the spin temperature is globally much larger than the CMB temperature, i.e., we assume that $T_{\mathrm{S}} \gg T_\gamma$. In this case the 21 cm signal appears in emission and the brightness temperature contrast is independent of T_{S}. This is expected to be a good approximation for the volume-averaged ionized fractions of interest for our present study, although it will break down at earlier times (e.g., Ciardi and Madau 8). With these approximations,

$$\delta T_{\mathrm{b}} = T_0 x_{\mathrm{HI}}(1 + \delta_\rho), \tag{2.27}$$

where $T_0 = 28 \left[(1 + z)/10\right]^{1/2} \mathrm{mK}$. Throughout this paper, we refer to the brightness temperature contrast in units of T_0.

Semi-Numeric Simulations

In order to simulate reionization we use the 'semi-numeric' scheme described in (57) (see also e.g., Mesinger et al. 38, for related work and extensions to this technique). This scheme is essentially a Monte Carlo implementation of the analytic model of (18), which

is in turn based on the excursion set formalism. The (57) algorithm allows us to rapidly generate realizations of the ionization field over large simulation volumes at various stages of the reionization process. The results of these calculations agree well with more detailed simulations of reionization on large scales (Zahn et al. 57, 58).

We start by generating a realization of the linear density field in a simulation box with a co-moving side length of 1 h^{-1}Gpc and 512^3 grid cells. The ionization field, x_i, is generated following the algorithm of (57), assuming a minimum host halo mass of $M_{\min} = 10^8 M_\odot$, comparable to the atomic cooling mass at these redshifts (Barkana and Loeb 1). Each halo above $M_{\min}$ is assumed to host an ionizing source, and the ionizing efficiency of each galaxy is taken to be independent of halo mass. In our fiducial model, we adjust the ionizing efficiency so that the volume-averaged ionization fraction is $\langle x_i \rangle = 0.79$ at $z_{\mathrm{fid}} = 6.9$. We focus most of our analysis on this redshift and on this particular model for the volume-averaged ionized fraction. However, we consider additional redshifts in §2.14, as well as variations around our fiducial ionization history in effort to bracket current uncertainties in the ionization history (see e.g., Kuhlen and Faucher-Giguere 26, Zahn et al. 56).

From the linear density field and the ionization field we generate the 21 cm brightness temperature contrast following Equation 2.27. Using the linear density field here – rather than the evolved non-linear density field – should be a good approximation for the large scales of interest for our study; we focus on length scales of $R \gtrsim 20\ h^{-1}$Mpc and high redshift ($z \gtrsim 6$) in subsequent sections.

Redshifted 21 cm Surveys and Thermal Noise

We mostly consider two concrete examples of upcoming redshifted 21 cm surveys. The first is based on the current, 128-tile version of the MWA (Tingay et al. 51) and the second is based on an expanded, 500-tile version of the MWA (as described in Lonsdale et al. 31, and considered in previous work such as Lidz et al. 28, McQuinn et al. 35). These two examples are intended to indicate the general prospects for imaging and bubble identification with

first and second generation 21 cm surveys, respectively. Similar considerations would apply for other experiments, but we choose these as a concrete set of examples. We mainly focus on the 500-tile configuration in this paper because of its greater sensitivity. In §2.14, we shift to considering 128-tile configurations and in §2.15, we consider a LOFAR-style interferometer for comparison. Hereafter, we refer to the 500-tile configuration as the MWA-500 and the 128-tile version as the MWA-128.

Throughout this paper, we work in co-moving coordinates described by Cartesian labels (x-y-z), with Fourier counterparts (k_x-k_y-k_z). The Fourier modes can be connected directly with the u-v-ν coordinate system generally used to describe interferometric measurements. Here u and v describe the physical separation of a pair of antennae in units of the observed wavelength, while ν describes the corresponding observed frequency. The instrument makes measurements for every frequency, ν, in its bandwidth, and for every antenna tile separation, (u, v), sampled by the array. In order to shift to a Fourier space description, the interferometric measurements must first be Fourier-transformed along the frequency direction. With our Fourier convention, the relation between the two sets of coordinates is given by:

$$k_x = \frac{2\pi u}{D} \qquad k_y = \frac{2\pi v}{D} \qquad k_z = \frac{2\pi}{\Delta\chi}, \tag{2.28}$$

where D is the co-moving distance to the survey center and $\Delta\chi$ is the co-moving distance corresponding to a small difference in observed frequency of $\Delta\nu$ (e.g., Liu et al. 30). For small $\Delta\nu/\nu$, we can express $\Delta\chi$ as

$$\Delta\chi \approx \frac{c(1 + z_{\text{fid}})}{H(z_{\text{fid}})} \frac{|\Delta\nu|}{\nu}, \tag{2.29}$$

where $H(z_{\text{fid}})$ is the Hubble parameter at the fiducial redshift, and $|\Delta\nu|/\nu$ is the absolute value of the fractional difference between two nearby observed frequencies.

In order to test the prospects for imaging and bubble identification with the MWA, we must corrupt the underlying 21 cm signal described in §2.11 with thermal noise. We do this by generating a Gaussian random noise field in the $\boldsymbol{k}$-space coordinate system described

above, using an appropriate power spectrum. We assume that the co-variance matrix of the thermal noise power is diagonal in $\boldsymbol{k}$-space. We add the resulting noise field to the underlying 21 cm signal (Equation 2.27). The power spectrum of the thermal noise is given by (McQuinn et al. 35, Furlanetto and Lidz 16):

$$P_{\mathrm{N}}(k, \mu) = \frac{T_{\mathrm{sys}}^2}{B t_{\mathrm{int}}} \frac{D^2 \Delta D}{n(k_\perp)} \left(\frac{\lambda^2}{A_{\mathrm{e}}} \right)^2. \tag{2.30}$$

Here μ is the cosine of the angle between wavevector $k = |\mathbf{k}|$ and the line of sight, so that $k_\perp = \sqrt{1 - \mu^2}k$ is the transverse component of the wavevector. We assume a system temperature of $T_{\mathrm{sky}} = 280\,[(1 + z)/7.5]^{2.3}$ K (Wyithe and Morales 55) and a total observing time of $t_{\mathrm{int}} = 1000$ hours, which is an optimistic estimate for the observing time in one year. At our fiducial redshift of $z_{\mathrm{fid}} = 6.9$, the co-moving distance to the center of the survey is $D = 6.42 \times 10^3 \; h^{-1}\mathrm{Mpc}$. In this equation, λ denotes the observed wavelength of the redshifted 21 cm line, $\lambda = 0.211(1 + z)\mathrm{m}$, and A_{e} is the effective area of each antenna tile. We determine A_{e} by linearly extrapolating or interpolating from the values given in Table 2 of (6); the effective area at $z_{\mathrm{fid}} = 6.9$ is $A_{\mathrm{e}} = 11.25\mathrm{m}^2$. We assume that the full survey bandwidth of 32 MHz is broken into individual blocks of bandwidth $B = 6$ MHz to protect against redshift evolution across the analysis bandwidth (McQuinn et al. 35). The co-moving survey depth depth corresponding to a $B = 6$ MHz chunk is $\Delta D = 69 \; h^{-1}\mathrm{Mpc}$. The $n(k_\perp)$ term describes the configuration of the antenna tiles. More specifically, it is the number density of baselines observing modes with transverse wavenumber $k_\perp$ (McQuinn et al. 35). Following (5) and (35), we assume the antenna tiles are initially packed as closely as possible in a dense compact core, and that the number density of antenna tiles subsequently falls off as r^{-2} out to a maximum baseline of 1.5 km. The radius of the dense antenna core is set by the requirement that the antenna density falls off as r^{-2} outside of the core, and that it integrates to the total number of antennae. For the MWA-500, this gives $r_{\mathrm{c}} = 20\mathrm{m}$, while for the MWA-128, the core radius is $r_{\mathrm{c}} \approx 8\mathrm{m}$. Equation 2.30 gives

the noise power spectrum in units of mK^2, and so we divide by T_0^2 to combine with the simulated 21 cm signal expressed in units of T_0.

Note that the volume of the MWA survey differs somewhat from that of our reionization simulation. In particular, the transverse dimension of the simulation is smaller than that of the MWA by a factor of ~ 3, while the simulation is deeper in the line-of-sight direction by about the same factor, as compared with the full MWA bandwidth. However, we remove the long wavelength modes along the line-of-sight direction to mimic foreground cleaning (§2.11), and so we do not, in practice, use the longer line-of-sight scales in our simulation box. As we will see, the ionized regions in the simulation are substantially smaller than the transverse length of the box. Transverse slices should therefore be representative of what the actual MWA will observe from a fraction of its larger field of view. We have checked that the coarser transverse k-space sampling in the simulation compared to in the actual MWA survey does not impact our results.

Foregrounds

Next, we need to consider contamination from foreground emission at the frequencies of interest. The relevant foregrounds include diffuse Galactic synchrotron radiation, extragalactic point sources, and Galactic Bremsstrahlung radiation. While these foregrounds are many orders of magnitude brighter than the cosmological 21 cm signal, they are expected to individually follow smooth power laws in frequency. Over a sufficiently small frequency range, the summed contributions can also be approximated as following a smooth power law, while the 21 cm signal will vary rapidly. This allows the foregrounds to be removed from the data by, for example, fitting a low-order function along each line of sight and subtracting it. While this procedure is effective at removing foreground contamination, it also removes long wavelength modes along the line of sight from the signal itself, and hence prevents measuring these modes. Several related methods for foreground removal have been

discussed in the literature (e.g., Wang et al. 53, Harker et al. 21, Petrovic and Oh 48, Chapman et al. 7). In this work, we approximately mimic the degrading effects from foreground removal by subtracting the running mean from the noisy signal along each line of sight, rather than including realizations of the foregrounds in our simulation and excising them with one of the above algorithms. We generally remove the running mean over a bandwidth of 16 MHz, which corresponds to a co-moving distance of $L_{\mathrm{fg}} = 185\,h^{-1}\,\mathrm{Mpc}$ at redshift $z_{\mathrm{fid}} = 6.9$; we consider the impact of other choices of L_{fg} in §2.14. We defer more detailed models of foreground contamination, and foreground removal algorithms, to future work.

2.12 Prospects for Imaging

Having described our mock 21 cm data sets, we now turn to consider the prospects for constructing direct 'images' of the redshifted 21 cm signal. Previous studies already suggest that the prospects for imaging with the MWA-500 are limited (McQuinn et al. 35). Here we emphasize that even a crude, low-resolution image of the redshifted 21 cm signal may be quite interesting, especially given that the ionized regions during reionization may be rather large scale features. We hence seek to quantify the imaging capabilities further using our corrupted reionization simulations. Here our work complements recent work in a similar vein by (60), who considered the prospects for imaging with LOFAR. While the central idea in this section is similar to this previous work, we focus on the MWA while (60) considered LOFAR. In order to construct the best possible images from the noisy mock 21 cm data, we apply a Wiener filter. We assess the ability of the MWA to image the redshifted 21 cm sky by comparing the filtered (recovered) noisy signal with the underlying noise-free 21 cm input signal.

The Wiener Filter

The Wiener filter is the optimal filter for extracting an input signal of known power spectrum when it is corrupted by additive noise, also with known power spectrum. As described in (49), this filter is optimal in that it minimizes the expectation value of the integrated squared error between the estimated signal field and the true signal field. The estimate of the true signal is a convolution of the Wiener filter and the corrupted signal in real space, and so is a product of the two quantities in Fourier space,

$$\tilde{S}(\mathbf{k}) = C(\mathbf{k})W(\mathbf{k}), \tag{2.31}$$

where $C(\mathbf{k})$, $W(\mathbf{k})$, and $\tilde{S}(\mathbf{k})$ are the Fourier transforms of the corrupted signal, Wiener filter, and estimated signal, respectively. Requiring that the filter be optimal in the least-square sense results in $W(\mathbf{k})$ taking the form

$$W(k, \mu) = \frac{P_{\mathrm{S}}(k)}{P_{\mathrm{S}}(k) + P_{\mathrm{N}}(k, \mu)}, \tag{2.32}$$

where $P_{\mathrm{S}}(k)$ and $P_{\mathrm{N}}(k, \mu)$ are the power spectra of the signal and noise, respectively. We note that, while the signal power spectrum is roughly isotropic[1], the noise power spectrum depends on μ and consequently so does the filter. The filter keeps a unity weighting for k-modes where $P_{\mathrm{S}}(\mathbf{k}) \gg P_{\mathrm{N}}(\mathbf{k})$ and significantly downweights k-modes where $P_{\mathrm{S}}(\mathbf{k}) \ll P_{\mathrm{N}}(\mathbf{k})$. This can allow for partial recovery of the original signal, provided that the signal power dominates for some $\boldsymbol{k}$-modes.

The Wiener filter requires an estimate of the signal power spectrum, $P_{\mathrm{S}}(k)$, and of the total (signal plus noise) power spectrum, $P_{\mathrm{S}}(k) + P_{\mathrm{N}}(k, \mu)$, as inputs. These may not be precisely known. However, since the filter is the outcome of a minimization problem – i.e., it minimizes the expected difference between the estimated and true fields – the accuracy

---

[1]Redshift-space distortions and redshift evolution across the observed bandwidth break isotropy (e.g. Datta et al. 12). However, for the bandwidth considered here ($B = 6$ MHz) and the neutral fractions of interest, the signal should be approximately isotropic.

of the filter should be insensitive to small changes about its optimal value. In other words, the accuracy of the filter is not expected to change greatly by using estimates of the signal and noise power spectra rather than the true spectra.

Furthermore, we do expect to have an estimate of the underlying signal power spectrum; measuring this statistic is a major goal of redshifted 21 cm surveys. Specifically, the underlying signal power can be estimated by cross-correlating redshifted 21 cm measurements made over two different time intervals (after foregrounds have been removed). The statistical properties of the signal should be identical across the two different time periods, but the thermal noise contributions will be independent. The cross-correlation between two time chunks then provides an unbiased estimate of the signal power (e.g., Liu et al. 30). Estimates of the noise power spectrum can then be made by subtracting the estimated signal power from the power measured over the entire integration time, which contains both the signal and noise contributions. The Wiener filter does not actually require the noise power spectrum to be known on its own. However, in §2.13 we consider the optimal matched filter, which does have this requirement. Throughout this study, we assume perfect knowledge of the underlying power spectra.

Before applying the Wiener filter to our corrupted simulations, it is useful to estimate the expected signal-to-noise ratio of the filtered maps analytically, using simulated signal power spectra and the noise power spectrum of Equation 2.30. The expected signal-to-noise ratio of the Wiener-filtered field is $\mathcal{S}_{\mathrm{wf}} = \tilde{\sigma}_{\mathrm{S}}/\tilde{\sigma}_{N}$, where $\tilde{\sigma}^2_{\mathrm{S(N)}}$ is the filtered signal (noise) variance. The signal and noise variance can in turn be calculated as integrals over their respective power spectra,

$$\tilde{\sigma}^2_{\mathrm{S(N)}} = \int \frac{\mathrm{d}^3 k}{(2\pi)^3} |W(k,\mu)|^2 P_{\mathrm{S(N)}}(k,\mu). \tag{2.33}$$

Here we use $P_{\mathrm{S(N)}}$ to denote the power spectrum of the signal (noise). One can also consider the impact of foreground cleaning here by downweighting modes where the foreground power

is large compared to the signal power. In order to consider the dependence of the signal-to-noise ratio on the stage of reionization, we consider simulation outputs in which the volume-averaged ionization fraction is $\langle x_i \rangle = 0.51, 0.68, 0.79$ and 0.89. We consider each of these models at our fiducial redshift of $z_{\text{fid}} = 6.9$.[1] Presently, we don't consider still earlier stages of reionization since the prospects for imaging with the MWA-500 are especially poor for lower ionized fractions.
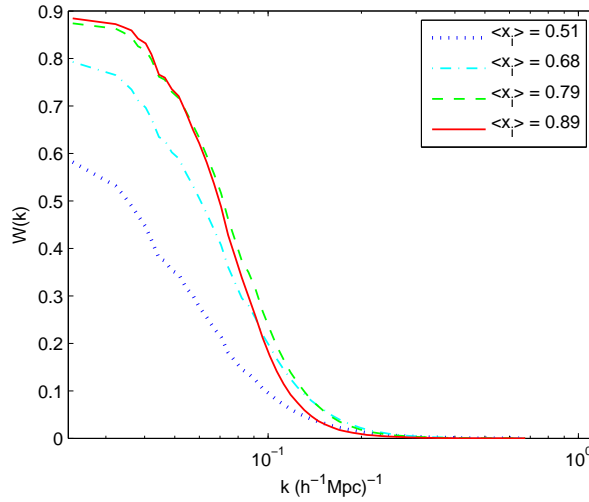
Figure 2.14: Fourier profile of the Wiener filter, $W(k)$. The filter is averaged over line-of-sight angle and the results are shown at $z_{\text{fid}} = 6.9$ for simulated models with $\langle x_i \rangle = 0.51$ (blue dotted), $\langle x_i \rangle = 0.68$ (cyan dot-dashed), $\langle x_i \rangle = 0.79$ (green dashed), and $\langle x_i \rangle = 0.89$ (red solid).

The resulting Wiener filters for the different values of $\langle x_i \rangle$ are shown in Figure 2.14,

---

[1]In practice, the simulated ionization fields for ionized fractions lower (higher) than our fiducial value ($\langle x_i \rangle = 0.79$ at $z_{\text{fid}} = 6.9$) come from slightly higher (lower) redshift simulation outputs. We generate the 21 cm signal and noise as though each data cube were in fact at $z_{\text{fid}} = 6.9$. This is appropriate to the extent that the statistical properties of the ionized regions are mainly determined by the volume-averaged ionized fraction, and are relatively insensitive to the precise redshift at which a given ionized fraction is reached (see McQuinn et al. 36 and Furlanetto et al. 18.)

after integrating over angle μ. In this figure, foreground cleaning has been accounted for by subtracting a running mean along the line of sight, as described in §2.11. It is helpful to note, from Equation 2.32, that the filter is equal to $1/2$ for modes where the signal and noise power are equal. The figure suggests that a small range of k-modes with $k \lesssim 0.1h$ Mpc^{-1} will have signal-to-noise ratio larger than unity for all four ionized fractions considered, although imaging is less promising for the smaller ionized fractions. If the ionized regions are larger than in our fiducial model – as expected if, for example, rarer yet more efficient and more clustered sources dominate reionization (e.g., McQuinn et al. 36, Lidz et al. 28) – then the prospects for imaging may improve somewhat. Performing the integrals in Equation 2.33, while incorporating foreground cleaning, we find that the total signal-to-noise ratio expected for the MWA-500 is $S_{\mathrm{wf}} = 0.52$, 0.79, 1, and 1.2 for $\langle x_i \rangle = 0.51, 0.68, 0.79, 0.89$, respectively.

Application to a Simulated 21 cm Signal

With the analytic signal-to-noise ratio estimates as a guide, we apply the Wiener filter to our mock noisy redshifted 21 cm data. The results of these calculations, for a particular slice through the simulation volume, are shown in Figure 2.15. The side length ($1\ h^{-1}$Gpc) of each slice is a factor of ~ 3 smaller than the transverse dimension of the MWA. One can asses how well the original signal is 'recovered' by comparing the top-left panel of the figure which shows the input signal with the bottom-left panel which shows the filtered noisy signal, after mimicking foreground removal. The two panels do not bear a striking resemblance since the average signal-to-noise ratio is only of order unity. Nonetheless, it is encouraging that many of the minima in the filtered noisy signal do indeed correspond to ionized regions in the input signal. Furthermore, we can compare the filtered noisy signal in the bottom-left panel with the top-right panel, which shows filtered pure noise. While these two panels do not look drastically different, they are easily distinguishable from each other given the increased contrast in the filtered noisy signal. In addition, we see that

the filtered noisy signal obtains signal-to-noise values exceeding $6 - \sigma$, while the statistical significance of the filtered noise does not exceed $\sim 5 - \sigma$. Quantitatively, $\sim 3\%$ ($\sim 0.03\%$) of the volume in the filtered noisy signal is occupied by pixels with statistical significance greater (in magnitude) than $3 - \sigma$ ($5 - \sigma$). This is expected given that the filtered data cube has an average signal-to-noise ratio of $\sigma_{\mathrm{S}}/\sigma_{\mathrm{N}} \approx 1$, as anticipated in the analytic calculation of §2.12.

Comparing the filtered noisy signal and the filtered pure noise, one can see that ionized regions in the underlying signal are diminished if they happen to be coincident with upward fluctuations in the noise, as expected. For example, the ionized region in the bottom-right corner of the unfiltered signal lies very close to a $\sim 3 - \sigma$ upward fluctuation in the filtered noise and, as a result, appears with weak statistical significance in the filtered noisy signal. Conversely, some of the most statistically significant regions in the filtered noisy signal occur when ionized regions overlap downward noise fluctuations. We can further compare the filtered noisy signal with the filtered noise-*less* signal, shown in the bottom right panel of Figure 2.15. The filtered noise-less signal is normalized by the standard deviation of the filtered noise so that it can be compared with the signal-to-noise slices in the other panels. This comparison reveals that high significance regions ($\gtrsim 5 - \sigma$) in the filtered noisy signal only line up well with the corresponding regions in the filtered noiseless signal if they are coincident with downward fluctuations in the noise. On its own, the filtered noiseless signal only attains statistical significances of $\lesssim 4\sigma_{\mathrm{N}}$. Finally, Figure 2.16 illustrates the impact of foreground cleaning, performed here over a bandwidth of 16 MHz (§2.11). Foreground cleaning removes the long wavelength modes along the line of sight – which is along the vertical axis in the figure – and thereby compresses structures along the line of sight. However, the cleaning process only impacts the long wavelength line-of-sight modes which still leaves room to image other modes robustly.

Note that the slice thickness ($8\ h^{-1}\mathrm{Mpc}$) in Figure 2.15 and 2.16 is somewhat arbitrary. However, the Wiener filter smooths out structure on significantly larger scales than this

(Figure 2.14), and so we expect similar results for other values of the slice thickness, provided the slice is thin compared to the cut-off scale of the filter. In practice, of course, one can make many independent maps similar to Figure 2.15 from the MWA-500 or similar surveys. Collectively, our results mostly confirm previous wisdom; the prospects for imaging with the MWA-500 are limited. Nonetheless, it appears that a signal-to-noise ratio of order unity is achievable, suggesting that the MWA-500 *can* make low resolution maps of the reionization process.

2.13 Prospects for Identifying Ionized Regions

We now shift our focus to discuss whether it may also be possible to identify interesting individual features in upcoming 21 cm data cubes. In particular, we aim to identify ionized regions in noisy 21 cm data sets and, furthermore, to estimate the spatial center and approximate size of each ionized bubble. For this purpose, we will use an optimal matched filter technique. As we discuss, individual ionized regions may be identifiable as *prominent minima in the filtered field*.

The Optimal Matched Filter

The optimal matched filter is suited for the case of a corrupted signal containing a known feature that one would like to extract. The filter acts in Fourier space by cross-correlating the corrupted signal with a template describing the known feature, while downweighting $\boldsymbol{k}$-modes in the corrupted signal by the noise power. The resulting form of the filter in Fourier space, $M(k, \mu)$, is

$$M(k, \mu) = \frac{T(\mathbf{k})}{P_{\mathrm{N}}(k, \mu)}, \tag{2.34}$$

where $T(\mathbf{k})$ is the Fourier profile of the known feature. The filter is optimal in the sense that it maximizes the signal-to-noise ratio in the filtered data cube at the location of the feature being extracted. While the Wiener filter requires an estimate of the signal and total (signal

plus noise) power spectra, the matched filter requires a good estimate of the template profile, $T(\mathbf{k})$, and the noise power spectrum, $P_N(k, \mu)$. For our present application, we would like templates describing the ionized regions. An appropriate choice is not obvious; theoretical models predict that the ionization state of the gas during reionization has a complex, and somewhat uncertain, morphology, with ionized regions of a range of sizes and shapes (Iliev et al. 24, Zahn et al. 57, McQuinn et al. 36). However, we find that the simplest conceivable choice of template filters, corresponding to completely ionized spherical bubbles of varying size, are nonetheless effective at identifying ionized regions with a more realistic and complex morphology. In this case, $T(\mathbf{k}; R)$ is just the Fourier transform of a spherical top-hat of radius R and is given by

$$T(\mathbf{k}; R_T) = \frac{V}{k^3 R_T^3} \left[-kR_T \cos kR_T + \sin kR_T \right], \tag{2.35}$$

with V denoting the volume of the spherical top-hat. Note that the precise normalization of the filter is unimportant since we are mainly interested in the signal-to-noise ratio here, in which case the overall normalization divides out.

Application to Isolated Spherical Ionized Regions with Noise

It is instructive to first consider an idealized test case that can be treated analytically before applying the matched filter to our full mock 21 cm data sets. In particular, we consider the case of an isolated, spherical, and highly ionized region placed at the origin and embedded in realistic noise. We assume that the neutral fraction exterior to the ionized region is uniform, with a mass-weighted neutral fraction of $\langle x_{HI}(1 + \delta_\rho) \rangle$. Ignoring foreground contamination for the moment, the 21 cm signal may be written as:

$$\delta T_b(\mathbf{x}) - \langle \delta T_b \rangle = \tilde{B}(\mathbf{x}; R_B) + \tilde{N}(\mathbf{x}), \tag{2.36}$$

where $B(\mathbf{x}; R_B)$ denotes our isolated bubble of radius R_B, and $N(\mathbf{x})$ denotes the thermal noise contribution to the signal. We have subtracted off the overall mean brightness temperature, $\langle \delta T_b \rangle$, since this will not be measured in an interferometric observation. The

tildes indicate that the spatial average has been removed from each of the underlying signal and noise so that $\tilde{B}(\mathbf{x}; R_\mathrm{B})$ and $\tilde{N}(\mathbf{x})$ each have zero mean. In this case $\tilde{B}(\mathbf{x}; R_\mathrm{B})$ has an inverted spherical top-hat profile,

$$\tilde{B}(\mathbf{x}; R_\mathrm{B}) = \begin{cases} - \langle x_\mathrm{HI}(1 + \delta_\rho) \rangle & |\mathbf{x}| < R_\mathrm{B}, \\ 0 & \text{otherwise.} \end{cases} \tag{2.37}$$

The Fourier transform of the isolated bubble is hence related to the Fourier transform of our template by $\tilde{B}(\mathbf{k}; R_\mathrm{B}) = - \langle x_\mathrm{HI}(1 + \delta_\rho) \rangle \, T(\mathbf{k}; R_\mathrm{B})$. Note that we express brightness temperatures in units of T_0 (see Equation 2.27), and so all quantities here are dimensionless.

It is straightforward to derive the expected signal-to-noise ratio at the center of the isolated ionized region, and thereby gauge the prospects for bubble detection with a matched filter technique. Let us assume that the radius, R_B, of our template filter is well matched to the true radius of the ionized region. This will maximize the expected signal-to-noise ratio. Neglecting foregrounds for the moment, and using the fact that the thermal noise has zero mean, we find that the signal-to-noise ratio at bubble center for the optimal matched filter is:

$$\mathcal{S}(R_\mathrm{B}) = - \langle x_\mathrm{HI}(1 + \delta_\rho) \rangle \left[\int \frac{\mathrm{d}^3 k}{(2\pi)^3} \frac{T^2(k; R_\mathrm{B})}{P_\mathrm{N}(k, \mu)} \right]^{1/2}. \tag{2.38}$$

For our sign convention, in which the template and ionized regions have opposite signs, this quantity is negative – ionized bubbles are regions of low 21 cm signal. The contribution of a Fourier mode to the signal to noise ratio depends on the relative size of $T^2(k; R_\mathrm{B})$ and $P_\mathrm{N}(k, \mu)$: modes for which the template is much larger than the noise power contribute appreciably to $\mathcal{S}(R_\mathrm{B})$ while modes dominated by the noise power are not useful. The signal-to-noise ratio depends on the neutral fraction: a larger exterior neutral fraction increases the contrast between an ionized bubble and the exterior, and hence boosts the detectability of the ionized region. We would like to calculate the expected signal-to-noise ratio for ionized regions of different sizes and for various volume-averaged ionization fractions. To do this, we need to connect the volume-averaged ionized fraction with the mass-averaged fraction,

$\langle x_{\mathrm{HI}}(1+\delta_\rho)\rangle$, which enters into Equation 2.38. Here we should incorporate that large scale overdense regions are generally ionized before typical regions during reionization, i.e., the neutral fraction and overdensity fields are anti-correlated. Defining $\delta_x = (x_{\mathrm{HI}} - \langle x_{\mathrm{HI}}\rangle)/\langle x_{\mathrm{HI}}\rangle$, we approximate $\langle \delta_x \delta_\rho\rangle$ as fixed at $\langle \delta_x \delta_\rho\rangle = -0.25$ throughout the reionization process (Lidz et al. 27).

The results of the signal to noise calculation are shown in Figure 2.17 for the MWA-500 and a LOFAR-type experiment. Here we consider only our fiducial redshift, $z_{\mathrm{fid}} = 6.9$. The (absolute value of) $S(R_{\mathrm{B}})$ is evidently a strongly increasing function of bubble size. This occurs because the thermal noise is a strong function of scale and only the rather large scale modes are measurable. It is encouraging that the expected signal-to-noise ratio exceeds five, $S(R_{\mathrm{B}}) \gtrsim 5$, for a range of radii and neutral fractions. This corresponds to a $5 - \sigma$ detection: 'false' bubbles at this significance from downward fluctuations in the noise are highly unlikely, with a fraction of only $\sim 3 \times 10^{-7}$ of pixels in the filtered noise having such a large (negative) significance on their own. For simplicity we neglect the impact of foreground cleaning in this figure: this will degrade the expected signal-to-noise ratios somewhat, as we will consider subsequently (see §2.13, §2.14).

In order to estimate the number of bubbles that can be detected from these curves, we need to consider how many bubbles there are of different sizes, i.e., we need to fold in an estimate of the bubble size distribution. In particular, while the contrast of an ionized region increases with the neutral fraction, large ionized bubbles become increasingly scarce for larger values of the neutral fraction. For instance, we can consider the model bubble size distributions in Figure 4 of (57). This figure indicates that bubbles of radius larger than 30 h^{-1}Mpc are exceedingly rare for neutral fractions larger than $\langle x_{\mathrm{HI}}\rangle > 0.5$, with only the tail end of the distribution extending past 25 h^{-1}Mpc. However, bubbles this size are relatively common later in reionization. Since Figure 2.17 indicates that only bubbles with $R \gtrsim 30$ h^{-1}Mpc exceed $S(R_{\mathrm{B}}) \gtrsim 5$, this suggests that bubble detection is feasible for the MWA-500 after the Universe is more than $\sim 50\%$ ionized, but that it will

be difficult to use this method at earlier stages of the reionization process. Also, note again that the the calculation here neglects the effects of foreground cleaning. However, we find that incorporating foreground cleaning only has a small effect on bubbles of this size ($\lesssim 30\,h^{-1}\,\mathrm{Mpc}$, §2.14). Bubble detection will also be challenging once the Universe is less than $\sim 10 - 20\%$ neutral, owing mostly to the reduced contrast between the bubbles and typical regions. If the ionized bubbles at a given stage of the EoR are larger than in the model of (57), then the prospects for bubble detection will be enhanced. We refer the reader to (36) for a quantitative exploration of the bubble size distribution across plausible models for the ionizing sources.

Finally, it is interesting to consider a LOFAR-style interferometer, as discussed further in §2.15. This is shown as the red dot-dashed curve in Figure 2.17. The expected $\mathcal{S}(R)$ exceeds that of the MWA-500 for small bubble radii, before flattening off at larger radii. This occurs because the LOFAR-style interferometer has more collecting area per baseline, but a larger minimum baseline. This makes it more sensitive to the smaller ionized regions, but less sensitive to larger ones.

While the signal-to-noise curves in this toy case provide a useful guide, we should keep in mind their limitations. First, it considers only the case of a single isolated ionized region. Next, we consider here only the signal to noise at the bubble center, while an ionized region will typically have a strong (negative) signal to noise over much of its volume. This can help significantly with detection. Finally, we consider only the *average* signal-to-noise ratio here. In practice, the signal-to-noise ratio in a filtered map may fluctuate significantly around this average, as we will see.

Application to a Simulated 21 cm Signal

With the estimates of the previous section as a rough guide, we now apply the matched filter to our noisy mock redshifted 21 cm data. In order to illustrate the results of passing our mock data through a matched filter, we start by examining simulated signal-to-noise

fields for a single template radius of $R_{\mathrm{T}} = 35 \ h^{-1}\mathrm{Mpc}$. This template radius corresponds to the typical size of the ionized bubbles we believe we can detect (see Figure 2.17). A representative slice through the simulation is shown in Figure 2.18. The results look promising, with signal-to-noise ratios comparable to the values anticipated in the idealized calculation of Figure 2.17. Although the Wiener filter provides the best overall map, or data cube, one can still detect individual features at greater significance by applying a matched filter. Comparing with Figure 2.15, it is clear that the Wiener filter is passing more small scale structure than the matched filter shown here. This results in the signal-to-noise ratio being larger (in absolute value) for the matched filter than for the Wiener filter. In particular, we find values of the signal-to-noise ratio that are as low as ~ -10 in the matched filter data cube, a significant improvement over the global minimum of ~ -6 for the Wiener filter. Moreover, we can compare the filtered noisy signal in the bottom-left panel with the filtered pure noise field in the top-right panel. They differ by more than in the case of the Wiener filter. Indeed, the very low signal to noise ratio regions (shown in dark blue/purple in the bottom-left panel) line up fairly well with ionized regions in the top-left panel. This is especially apparent when comparing the filtered noisy signal to the filtered noiseless signal, shown in the bottom-right panel. For the slice shown, almost all of the significant features in the filtered noiseless signal are preserved in the noisy case. Figure 2.19 shows the impact of foreground cleaning: as in the case of the Wiener filter (Figure 2.16), this compresses structures along the line of sight and reduces the overall signal-to-noise ratio in the data cube. The signal-to-noise ratio is still significant enough, however, to robustly identify ionized regions.

As with the Wiener filter, and in what follows subsequently, we show slices of $8 \ h^{-1}\mathrm{Mpc}$ thickness. This choice is arbitrary, but we expect similar results provided the slice thickness is small compared to the radius of the template filter. It is important to keep in mind, however, the full data cube will consist of many separate slices of this thickness. Also note

that the transverse dimension of the MWA-500 is larger than that of our simulation box by a factor of ~ 3, and so these slices represent only $\sim 1/9$ of the MWA field of view.

These results are promising, but they are for a single filtering scale, and so we can do significantly better by considering a range of template radii, and looking for extrema in the resulting signal-to-noise fields. In particular, we proceed to apply a sequence of filters with template radii up to $R_\mathrm{T} \leq 75\,h^{-1}\,\mathrm{Mpc}$ – see §2.13 for a justification of this maximum – across the simulation volume. We assign the minimum (most negative) signal-to-noise value obtained over the range of template radii to each simulation pixel and use this to construct a new field. The position of local minima in this field are chosen to be the centers of candidate bubbles, and each such bubble is assigned a radius according to the scale of the template filter that minimizes its signal-to-noise. We focus on *minimum* values since ionized regions are expected to appear as regions of low 21 cm signal. All candidate bubbles whose central signal to noise is lower than -5 are considered to be detected ionized regions.

We find it important to apply one additional criterion to robustly identify ionized regions. The criterion is that a low signal to noise region on scale R_B must additionally be *low in signal to noise at all smaller smoothing scales*, $R_\mathrm{T} < R_\mathrm{B}$. This guards against the possibility that a detected bubble will be centered on neutral material that is nevertheless surrounded by ionized hydrogen. A region like this will have a high (least negative) signal-to-noise when filtered on small scales and then dive down (gaining statistical significance) when filtered on scales containing the surrounding ionized material. We discard such spurious bubbles by requiring that the field is low on all smaller smoothing scales. The only downside to this procedure is that it occasionally discards true ionized regions whose center happens to coincide with a significant upward noise fluctuation. Overall, however, it improves the quality of detected bubbles (§2.13). This cut also requires a threshold choice; we reject candidate regions if their signal-to-noise ratio crosses above a threshold $\mathcal{S}_\mathrm{max}$ at any smoothing scale less than R_T. After trying several thresholds, we found the most effective choice to be $\mathcal{S}_\mathrm{max} = -1\sigma$. In principle, one might use the full curve of signal-to-noise ratio

versus template radius for each candidate bubble to help verify the detection and determine the properties of the bubble. In practice, we found that individual signal-to-noise curves are noisy and difficult to incorporate into our analysis and so we don't consider this possibility further in what follows.

We apply this algorithm to the mock redshifted 21 cm data and identify 220 ionized regions across the simulation volume (which is different than the MWA survey volume, as we will discuss subsequently). A representative example of a detected bubble is shown in Figure 2.20. The circle in the figure identifies the detected bubble size and the location of its center in both the filtered noisy signal (top-left and top-right panels), as well as in the input signal (bottom-left and bottom-right panels). The algorithm has convincingly identified an ionized region. The detected bubble overlaps a small fraction (%10) of neutral material in the input signal. Although this particular ionized bubble is well identified, most of the ionized regions in the signal will escape detection. This is because the significance levels of the detected bubbles are not that high, and an ionized region generally needs to be coincident with a downward fluctuation in the noise to pass our significance threshold. For example, consider the larger ionized region below and to the left of the detected region in the bottom-left panel of Figure 2.20. This region, while larger and therefore more detectable on average than the identified bubble, happens to coincide with a large upward noise fluctuation and hence fails to cross the significance threshold. While we can not identify all of the large ionized regions in the noisy mock data, we can robustly identify some regions; this may still be quite valuable.

It is also clear that the underlying ionized regions are manifestly non-spherical, creating an ambiguity as to what the appropriate 'radius' of the region is. Focusing on the bottom right panel in Figure 2.20, we could imagine the size being reasonably described by a radius $\sim$ %50 larger, so as to enclose more of the nearby ionized material. However, our method naturally favors radii causing little overlap with neutral material at these size scales. Therefore, an ionized region like the one shown in Figure 2.20 is more likely to be detected

as several small ionized regions than one large one, although both characterizations seem reasonable.

Figure 2.21 gives a further example of how the algorithm identifies bubbles, and some of the ambiguities that can result. This figure shows an example of an irregular, yet contiguous, ionized region that is detected as more than one ionized bubble. Here we show spatial slices through the center of the middle sphere, marked with a solid circle, which happens to intersect neighboring ionized bubbles, whose cross sections are shown as dashed circles. Hence, our algorithm generally represents large, irregularly shaped, yet contiguous, regions as multiple ionized bubbles.

It is important to emphasize further the difference between the simulated results shown here and the idealized test case of the isolated bubble shown in the previous section. In particular, we consider here the application of matched filters to the 21 cm signal during a late phase of reionization in which many ionized regions, with a broad size distribution, fill the survey volume: the ionized regions *are not* isolated bubbles in a sea of partly neutral material. When applying a matched filter of template radius R_T around a point, the values of the field at many neighboring pixels impact the filtered field at the point in question. It is hence possible that a filtered pixel is affected by several distinct neighboring ionized regions. Indeed, this can result in even neutral regions having low signal-to-noise ratios provided they are surrounded by many nearby ionized regions. For instance, in the low noise limit, *any region with volume-averaged neutral fraction lower than the cosmic mean would pass our significance threshold*. To guard against this type of false detection, we implemented the requirement that a candidate bubble has low signal-to-noise for *all* template radii smaller than the detected radius. Another possibility might be to treat small ionized regions as an additional noise term in the filter. However, in practice, our attempts along these lines introduced an additional level of model dependence without significantly increasing the quality of the detected bubbles. Ultimately, it is important to keep in mind that the signal-to-noise values quoted here reflect only the likelihood that a value arises purely from noise,

and so they are not strictly indicative of the quality of the detected bubbles.

Success of Detecting Ionized Regions

We hence turn to describe the characteristics of the detected ionized regions, and to quantify the method's level of success in detecting ionized bubbles. To do this, we calculate the fractional overlap of each detected bubble with ionized material in the underlying signal. Additionally, we estimate how many ionized bubbles should be detectable across the entire MWA-500 survey volume.

The matched filter technique finds 220 bubbles across our simulation volume. However, the algorithm for determining bubble positions and sizes allows for bubbles to occupy over-lapping areas, as shown in Figure 2.21. We find that $\sim 55\%$ of the detected bubbles have *some* overlap with another bubble, although only $\sim 15\%$ of the *total* volume occupied by detected bubbles is occupied by more than one. Regardless, $\sim 96\%$ of the detected ionized bubbles have an average ionized fraction larger than $x_i = 0.79$, which is the volume-averaged ionization fraction of the simulation box at the redshift under consideration. Furthermore, $\sim 42\%$ of the detected bubbles have an ionized fraction greater than $x_i = 0.9$. The lowest ionization fraction of a detected bubble is $x_{i,\min} = 0.77$, just slightly below the volume-averaged ionization fraction of the simulation. In total, we detect 9 bubbles whose ionized fractions are less than the average ionization fraction of the box. Inspection reveals that these regions happen to be coincident with significant $(\leq -3 - \sigma)$ downward noise fluctuations.

In Figure 2.22, we plot the volume-averaged ionized fraction within each of our detected bubbles against the detected bubble radius. For comparison, we show the $1 - \sigma$ spread in the ionized fraction enclosed by *randomly* distributed spheres of the same size.[1] The spread

---

[1]The $1 - \sigma$ spread shown in the figure extends past $x_i = 1$, but this is only because the distribution of ionized fractions is not symmetric about the mean, i.e., the probability distribution function of the ionized fraction is non-Gaussian.

in ionization of the randomly distributed spheres around the box average ionized fraction, $\langle x_i \rangle = 0.79$, decreases with increasing radius; this reflects the drop off in the power spectrum of the ionization field towards large scales. Most of the detected bubbles are significantly more ionized than random regions, as expected, indicating a significant success level. There are a few poor detections which result mostly from downward noise fluctuations. There is a small overall decrease in the ionized fraction of detected bubbles larger than $R_\mathrm{B} \gtrsim 40$ $h^{-1}\mathrm{Mpc}$, suggesting that we may no longer be detecting individual ionized regions here. These regions may potentially be distinguished from isolated bubbles by examining the signal-to-noise ratio as a function of template radius closely, as we discuss in §2.13.

We can estimate the number of ionized regions detectable in the MWA-500 by scaling from our simulation volume to the MWA survey volume. At $z_\mathrm{fid} = 6.9$, for an ionized fraction of $\langle x_i \rangle = 0.79$, we expect to find 140 bubbles in a $B = 6$ MHz chunk of the MWA, over its entire field of view of ~ 770 deg^2. About 135 (60) of these detected bubbles are expected to have ionized fractions larger than 79% (90%). This estimate comes from simply scaling our simulation volume (which is deeper than the MWA bandwidth) to a 6 MHz portion of the MWA survey volume. Analyzing the MWA data over a 6 MHz chunk is meant to guard against redshift evolution: the full bandwidth of the survey is $B = 32$ MHz and so the prospects for bubble detection across the full survey are even better than this estimate suggests. The precise gain will be dependent on how rapidly the bubble size distribution evolves across the full survey bandwidth. One caveat with our estimate, however, is that $B = 6$ MHz corresponds to only $\sim 70\, h^{-1}\,\mathrm{Mpc}$. This is comparable to the size of our larger bubbles, and so analyzing chunks this small might weaken our ability to detect large bubbles. This effect is not incorporated in our scaling estimate, which simply takes the ratio of the MWA survey volume and our simulation volume. In practice, one can perform the bubble extraction for different analysis bandwidths to help ensure robust detections.

Range of Template Radius Considered

It is worth mentioning one further detail of our algorithm. In the previous section, we set the maximum template radius considered at $R_{\mathrm{T,max}} = 75 \ h^{-1}\mathrm{Mpc}$, without justification. In fact, we have a sensible and automated way for arriving at this choice. We discuss this procedure briefly here.

A good candidate ionized region should in fact obey three criteria. First, it should have a large (negative) signal-to-noise ratio, so that it is unlikely to result from a noise fluctuation. Second, the signal-to-noise ratio should be small for all trial radii smaller than the optimal template radius, as discussed in §2.13. Finally, the total signal must itself be small in an absolute sense. In the limit of low noise, anything less neutral than average would qualify as a bubble by the first criterion, and so this third criterion may then become important for robustly identifying bubbles. This low noise limit is relevant for the MWA-500 only on very large smoothing scales, where the noise averages down significantly.

Since this third criterion becomes important only on very large smoothing scales here, we use it only to set the maximum template radius considered. Without this third consideration, our algorithm generally identifies a few excessively large ionized bubbles, but this can be easily understood and avoided as follows. Consider, for the moment, the 21 cm brightness temperature field in the absence of noise and foregrounds. Let's further work in units of T_0 (Equation 2.27), and remove the average brightness temperature contrast across the data cube. In this case, the signal inside a highly ionized bubble is expected to be $-\langle x_{\mathrm{HI}}(1 + \delta_\rho)\rangle$. If we now spherically average the field on scales smaller than the bubble, the value at bubble center will not change from this value, $-\langle x_{\mathrm{HI}}(1+\delta_\rho)\rangle$. Once the smoothing scale becomes larger than the bubble scale, however, surrounding neutral material will increase the value of the filtered field at bubble center. Hence, if the filtered field becomes everywhere larger than $-\langle x_{\mathrm{HI}}(1 + \delta_\rho)\rangle$ on some smoothing scale, it is clear that no larger ionized bubbles exist within the data cube. This suggests that we can set the maximum template radius by requiring that the filtered noisy signal reaches sufficiently small values,

84

at some locations across the data cube, for there to still plausibly be completely ionized regions. Since the presence of noise only increases the variance, this should provide a conservative estimate of the maximum size of the ionized regions. In practice, we need to chose a threshold criterion without assuming prior knowledge of the neutral fraction. Here we set the maximum template radius to be the smallest smoothing scale at which the filtered noisy field everywhere exceeds $-\langle x_{\mathrm{HI}}(1 + \delta_\rho)\rangle \geq -0.075$. This corresponds to the expected contrast at $\langle x_{\mathrm{HI}}\rangle = 0.1$, assuming $\langle \delta_x \delta_\rho \rangle = -0.25$, and yields a maximum template radius of $R_{\mathrm{T,max}} = 70 \, h^{-1} \, \mathrm{Mpc}$, $73 \, h^{-1} \, \mathrm{Mpc}$, $75 \, h^{-1} \, \mathrm{Mpc}$, and $75 \, h^{-1} \, \mathrm{Mpc}$ for $\langle x_i \rangle = 0.51$, 0.68, 0.79, and 0.89, respectively. The precise threshold used here, -0.075, is somewhat arbitrary but this choice is only being used to set the maximum template radius considered.[1]

2.14 Variations on the Fiducial Model

So far, we have considered the prospects for bubble detection only in our fiducial model with $\langle x_i \rangle = 0.79$ at $z_{\mathrm{fid}} = 6.9$ and only for the MWA-500. Here we consider first alternate models in which the Universe is more or less ionized at $z_{\mathrm{fid}} = 6.9$ than in our fiducial case, and then consider how the sensitivity declines towards higher redshifts at fixed ionized fraction. In addition, we consider variations around our fiducial assumptions regarding the impact of foreground cleaning. Then we turn to consider the sensitivity of the MWA-128; this is meant to illustrate the prospects for bubble detection with the very first generation of redshifted 21 cm surveys, while the MWA-500 represents a second generation survey.

---

[1]This choice might appear to preclude the possibility of detecting bubbles at the end of reionization when $\langle x_{\mathrm{HI}}(1 + \delta)\rangle \leq 0.075$. However, the threshold choice is only used to set the maximum template radius, and so ionized regions may still in principle be detected at these late stages of reionization. The ionized regions identified at the end of reionization are, however, generally less robust given the reduced contrast between fully ionized and average regions at these times (see §2.14).

Ionized Fraction

In order to consider bubble finding at earlier and later stages of the EoR, we run our matched filter on simulation outputs with volume-averaged ionized fractions of $\langle x_i \rangle = 0.51, 0.68$, and 0.89. As discussed in §2.12 these outputs are actually at slightly different redshifts, but we generate the 21 cm field as though they were at $z_{\text{fid}} = 6.9$. As far as bubble detection is concerned, varying the ionized fraction leads to two, generally competing, effects. First, the bubbles grow as reionization proceeds. This tends to boost detection, since it is only the large scale modes that are detectable over the thermal noise. Second, however, the *contrast* between an ionized region and a typical volume of the Universe is reduced as reionization proceeds. This makes bubble detection more difficult. Both of these effects are quantified in the idealized isolated bubble case in Figure 2.17. It is also clear that the ideal ionized fraction for bubble detection will be somewhat survey dependent. As already illustrated in Figure 2.17 and discussed further in §2.15, a LOFAR-type interferometer will perform better when the ionized regions are smaller.

We find that the matched filter is capable of detecting ionized regions for each of the ionized fractions studied. In Figure 2.23 we show histograms of the detected bubble size distributions for each ionized fraction. Since we preferentially detect large ionized regions, we don't expect these distributions to be representative of the true underlying bubble size distributions. For example, in Figure 2.23, the size distribution peaks around $\gtrsim 40\,h^{-1}\,\mathrm{Mpc}$ for the case of $x_i = 0.79$, despite volume-weighted size distribution peaking around $\sim 30\,h^{-1}\,\mathrm{Mpc}$ in Figure 4 of (57) at roughly the same ionized fraction. Nonetheless, the histograms illustrate a general shift from smaller to larger detected bubble radius as the ionized fraction increases. By applying the matched filter to several redshift bins, one can potentially observe precisely this evolution with the MWA-500. This would complement studies of the 21 cm power spectrum evolution over the same redshift range (e.g., Lidz et al. 28). From the histograms, one can see that – of the models shown – the best ionized fraction for bubble detection is $\langle x_i \rangle = 0.79$. This is apparently near the sweet spot for the

MWA-500 where the bubbles are large enough in the model for detection, but the contrast with typical regions is still sufficiently large.

The average ionized fraction within detected bubbles varies significantly across the different ionized fractions considered. Specifically, the percentage of detected bubbles that are more than 90% ionized is 0%, 15%, 43%, and 91% for $\langle x_i \rangle = 0.51$, 0.68, 0.79, and 0.89, respectively. However, in each case the percentage of detected bubbles with ionized fraction larger than the (global) volume-averaged ionization fraction is fixed at $\gtrsim 95\%$. At first glance, one aspect of these results may appear to be in tension with the calculations of §2.13, where we estimated that bubble detection would be unsuccessful for neutral fractions larger than $\langle x_{\rm HI} \rangle \gtrsim 0.5$. However, this estimate considered the detection of *isolated* bubbles. Inspection reveals that the detected bubbles at $\langle x_i \rangle = 0.51$ each correspond to clusters of smaller ionized regions. Evidently, these appear as a single larger ionized region after convolving with the template filter and downweighting the noisy short-wavelength modes. In practice, it may be possible to distinguish this case from that of an isolated bubble by analyzing the trend of signal-to-noise ratio versus trial template radius. The signal-to-noise ratio is expected to grow more rapidly with radius (before reaching the bubble scale) for a truly isolated bubble.

Timing of Reionization

We now consider how the prospects for bubble detection diminish if reionization occurs earlier and the observations are focused on the corresponding redshifts. In particular, we examine the case that our model with an ionized fraction of $\langle x_i \rangle = 0.79$ is observed at a higher redshift. We focus on this case since this ionized fraction appears close to optimal for bubble detection. Aiming for only a rough estimate here, we consider the prospects for detecting a $R_{\rm B} = 40 \ h^{-1}{\rm Mpc}$ bubble.

Although several different factors in the noise power spectrum of Equation 2.30 scale with redshift, the dominant scaling is with the sky temperature. The noise power scales as

$P_{\mathrm{N}} \propto T_{\mathrm{sky}}^2$, and the sky temperature follows $T_{\mathrm{sky}} \propto \nu^{-2.6} \propto (1+z)^{2.6}$. Therefore, we expect the signal-to-noise ratio of a detected bubble to fall off with increasing observation redshift roughly as

$$\mathcal{S}(z) = \mathcal{S}(z_{\mathrm{fid}}) \left(\frac{1 + z_{\mathrm{fid}}}{1 + z} \right)^{2.6}. \tag{2.39}$$

This indicates the signal-to-noise ratio for a bubble detected with a signal-to-noise of $\mathcal{S}(z_{\mathrm{fid}})$ at redshift $z_{\mathrm{fid}} = 6.9$, if the bubble were instead observed at redshift z. A relatively large bubble with $R_{\mathrm{B}} \approx 40 \ h^{-1} \mathrm{Mpc}$ has a typical signal-to-noise ratio at bubble center of $\mathcal{S} \approx 4$ at our fiducial redshift. This value is found by incorporating foreground cleaning into the corresponding curve in Figure 2.17. According to Equation 2.39, the signal-to-noise value will be reduced to a significance of $\mathcal{S} \approx 2$ (1) at $z = 9.3$ (12.5). The bubble will, in fact, be more detectable than implied by this one number – the signal-to-noise ratio at bubble center – since an ionized region should have low signal-to-noise over much of its volume. From this, we conclude that bubble detection should be feasible with the MWA-500 if our fiducial ionized fraction occurs later than $z \lesssim 9$ or so, but that the prospects are rather limited in the case of significantly earlier reionization. A range of recent work in the literature, however, suggests that reionization is unlikely to complete so early. See, for example, Figure 9 from the recent study of (26) which combines Ly-α forest data (Fan et al. 14), measurements of the Thomson optical depth from WMAP (Komatsu et al. 25), and measurements of the Lyman-break galaxy luminosity function (Bouwens et al. 3). Hence, the prospects for bubble detection appear good for the MWA-500.

Effects of Foreground Cleaning

Next, we consider the impact of variations around our standard foreground cleaning model. As discussed previously (§2.11), our standard assumption is that the impact of foreground cleaning can be approximately mimicked by removing the running mean, over a bandwidth of $B = 16$ MHz, across each line of sight. The optimal foreground cleaning strategy avoids 'over-fitting' by removing the smoothest possible function over the largest possible

bandwidth, in order to preserve the underlying signal as much as possible. It also avoids 'under-fitting' by ensuring that foreground residuals do not excessively contaminate the signal. (29), for example, find that 21 cm foregrounds can be removed to one part in 10^5 or 10^6 by subtracting roughly three modes over ~ 32 MHz of bandwidth. This should have a fairly similar impact to our fiducial cleaning model, but we would expect a bit more degradation in this case. A detailed investigation would add foreground contamination into our mock data cubes, and explore the impact of various cleaning algorithms directly.

Here, we instead check how our results change for slightly more and less aggressive foreground cleaning. In particular, we remove the running mean over each of $B = 8$ MHz and $B = 32$ MHz and rerun our bubble finding algorithm (at $z_{\mathrm{fid}} = 6.9$, $\langle x_i \rangle = 0.79$). This has little impact on our results. In particular, the number of identified bubbles varies by less than $10 - 15\%$ across the range of cleaning bandwidths considered. The quality of detected bubbles decreases slightly for the more aggressive cleaning model, and improves slightly in the most optimistic case. Specifically, for $B = 16$ MHz, 96% (43%) of bubbles have ionized fractions exceeding $x_i = 0.79$ (0.9); for $B = 8$ MHz the corresponding numbers are 90% (32%); and for $B = 32$ MHz the same numbers are 96% (62%). While these estimates are encouraging, a more detailed study is warranted. It may also be advantageous to estimate the power spectrum of the foregrounds, and incorporate this as an additional noise term in Equation 2.32 and Equation 2.34 for each of the Wiener filter and the matched filter, respectively.

128 Antenna Tile Configurations

So far our analysis has focused on the MWA-500, which is meant to represent a second generation 21 cm survey. In the near term, it is timely to consider the prospects for a 128 tile version of the MWA (the MWA-128) which is ramping up to take data in the very near future. This should be significantly less sensitive, since the number of baselines scales as the number of antenna tiles squared.

In order to generate thermal noise representative of the MWA-128, we start by considering a similar antenna distribution as for the MWA-500. In particular, we assume all of the antenna tiles are packed as closely as possible within a core of radius 8m and that the antenna distribution subsequently falls off as r^{-2} out to a maximum baseline of 1.5 km. After comparing the thermal noise power spectrum in this configuration with that in (2), we find that our noise power is larger by up to a factor of a few. This could possibly be due to our approximation of a smooth antenna distribution being less valid for the MWA-128, or to the fact that our analytic formula for the noise power spectrum does not incorporate a full treatment of rotation synthesis. In an effort to bracket somewhat the impact of the detailed antenna distribution, we further consider a configuration where all antenna tiles are packed as closely in a dense core of radius $\sim$ 25m. This resembles the 'super-core' configuration considered in (28) for the power spectrum.

The results of applying the optimal matched filter for a single template radius of $35h^{-1}$Mpc are shown in Figure 2.24 for the r^{-2} tile distribution. This shows that the sensitivity is much lower than for the MWA-500, as expected. It is much more difficult to distinguish the filtered noisy signal (bottom-left panel) from the filtered pure noise (top-left) panel here than in Figure 2.18. Most of the significant, dark blue regions in the filtered noisy signal correspond simply to low noise regions. However, applying the detection algorithm we do nonetheless detect 7 bubbles across a volume equivalent to a 6 MHz chunk of the MWA-128 survey. The success is generally lower than in the case of the MWA-500: here 75% of detected bubbles exceed the average ionized fraction of the box, while $\sim$ 42% exceed $x_i = 0.9$. In the supercore configuration, we find slightly higher significance levels (up to $6.9 - \sigma$) but the identified regions generally correspond to several large clustered ionized regions, rather than a single ionized bubble. Altogether, the algorithm identifies 10 ionized regions across the MWA survey in the supercore configuration, but the identified regions have a lower overall quality than in the r^{-2} configuration.

Our conclusion is that bubble detection is only marginally possible with the MWA-128.

While the results are unlikely to be very compelling, it is worth applying the matched filter to the first generation surveys as an initial test. Even a few weakly identified candidate bubbles would provide compelling targets for follow-up observations. Another possibility is to focus on *targeted searches* around known bright sources for the MWA-128 (e.g., Wyithe and Loeb 54, Friedrich et al. 15).

2.15 Favorable Antenna Configurations for Bubble Detection

The possibility of imaging or identifying ionized regions from second generation redshifted 21 cm surveys invites the question: how do we optimize future surveys for this goal? It seems unlikely that the optimal configuration for bubble detection is identical to that for measuring the power spectrum, although power spectrum measurements have mostly driven survey design considerations thus far. In the case of the power spectrum, one aims to minimize the error bar on power spectrum estimates in particular bins in wavenumber. The power spectrum error bar for each k-mode contains a thermal noise term and a sample variance (sometimes called 'cosmic variance') term. Because of the sample variance contribution, the gain from reducing the thermal noise for a given k-mode is limited: once the thermal noise is reduced sufficiently far below the sample variance, it is advantageous to instead measure a different k-mode on the sky within the $|k|$ bin of interest. As a result, grouping individual antennas into only small tiles to achieve a wide survey, generally reduces the statistical error bars on power spectrum measurements compared to antenna configurations with larger tiles that probe narrower fields of view. For imaging and bubble detection, one aims for the best possible signal to noise on *particular regions of the sky*. In other words, for good imaging one wants to reduce the thermal noise to *well* below the sample variance level. Grouping individual antennas into larger tiles, in order to devote more collecting area to a narrower field of view, may be better for this purpose.

In order to get some sense for these trade-offs, we consider here a LOFAR-style interferometer with the specifications listed in (36). Although the detailed specifications for LOFAR

have evolved somewhat (e.g., Zaroubi et al. 60), (as have the MWA specifications), this is nonetheless a helpful case to consider. In particular, our toy LOFAR-style interferometer has many fewer antenna tiles than the MWA-500 but a substantially larger collecting area per tile. Specifically, the interferometer considered has $N_a = 32$ antenna tiles, $A_e = 596\mathrm{m}^2$ at our fiducial redshift (compared to $A_e = 11.25\mathrm{m}^2$ for the MWA-500), $d_{min} = 100\mathrm{m}$, and $d_{max} = 2$ km. We assume that antenna tiles are packed as closely as possible, consistent with $d_{min} = 100\mathrm{m}$, inside a compact core and that the density subsequently falls off as r^{-2}, out to a maximum radius of $r_{max} = 1000\mathrm{m}$. These parameters are meant to broadly represent an upgraded version of the existing LOFAR array, analogous to our MWA-500 survey, which is an upgrade to the ongoing MWA-128 instrument. With these parameters, the LOFAR-style interferometer has more total collecting area than the MWA-500 setup by a factor of a few.

The results of applying a matched filter to a data cube with simulated LOFAR noise are shown in Figure 2.25. Here we zoom in to show a portion of our simulation box that matches the smaller field of view of this LOFAR-like instrument. From the figure it is evident that the filter removes large scale structures, a result of the relatively large minimum baseline of this interferometer. In addition, the maximum signal-to-noise achieved here is smaller than with the MWA-500 (it drops from 10 to 6.9). Nonetheless, many small-scale ionized regions in the unfiltered noise-less signal are well preserved in the filtered noisy signal. This is consistent with the idealized calculation of Figure 2.17, which showed that LOFAR should have a higher signal-to-noise detection of small ionized regions, but a reduced signal-to-noise otherwise. Because of this, the LOFAR-style configuration is more successful during earlier stages of reionization when the bubbles are still relatively small. In general, we find that the LOFAR-style configuration detects slightly fewer bubbles overall but with more success for $\langle x_i \rangle \lesssim 0.79$, while the MWA-500 has a greater level of success at later stages of the EoR.

This example suggests that the ideal configuration for bubble detection is likely intermediate between the MWA-style and LOFAR-style antenna configurations. It appears helpful

to have more collecting area on fewer baselines than the MWA, but a smaller minimum baseline than in the LOFAR-style instrument is necessary to detect large bubbles. This deserves further study, however: for example, we have neglected calibration requirements and systematic concerns. These considerations will also certainly drive the experimental design. As a further concrete example of how systematic concerns could impact the design of future arrays, suppose foreground cleaning requires removing more large scale modes than anticipated. In this case, it would make sense to focus efforts on smaller bubbles. This would shift the ideal configuration closer to a LOFAR-style instrument with a larger minimum baseline.

2.16   Comparisons to Previous Work

Previous work by (10) and (11) also considered the possibility of detecting ionized regions in noisy redshifted 21 cm data sets using a matched filter technique. The main difference between our study and this earlier work is that these previous authors considered the prospects for detecting a *specific* spherical ionized region of varying size, i.e., they considered the detectability of a spherical bubble at the origin, or offset slightly from the origin. These authors also considered the case where the bubble of interest was embedded in a variety of different ionization environments; the bubble under consideration was not always isolated. Altogether, their study is mostly similar to a targeted search, where one has a good prior regarding the likely location of an ionized region. It also provides a feasibility estimate for a more ambitious blind search. The main advantage of a targeted search is that, if a region is known *a priori* to be highly ionized, one need not worry about an entirely false detection from a downward noise fluctuation. This then allows a lower significance threshold for robust bubble detection, and may therefore be the most feasible approach for the MWA-128 and other first generation surveys.

Nonetheless, our work is a significant extension to the earlier work by (10) in that we conduct a blind search across an entire mock survey volume. A detailed comparison with

their work is not straightforward given the difference between our approaches, but both studies have a similar bottom-line conclusion: ionized regions are detectable with surveys similar to the MWA-500.

2.17 Conclusion

We considered the prospects for making low-resolution images of the 21 cm sky and for direct, blind detection of ionized regions using first and second generation 21 cm surveys. We find that a 500-tile version of the MWA, the MWA-500, is potentially capable of detecting ionized regions. In our fiducial model, in which 79% of the volume of the Universe is ionized at $z_{\mathrm{fid}} = 6.9$, the MWA-500 can find ~ 150 ionized regions in a $B = 6$ MHz chunk after $\sim 1,000$ hours of observing time. First generation surveys, such as the MWA-128, are substantially less sensitive. We find that the MWA-128 may, nonetheless, be able to detect a handful of ionized regions across its survey volume, with 7 expected in our fiducial model. The MWA-128 may be more effective at identifying ionized bubbles using targeted searches towards, for example, bright quasars (e.g. Friedrich et al. 15).

There are several possible future directions for this work. First, while we incorporate realistic levels of thermal noise and mimic the effect of foreground cleaning, it will be important to test the robustness of bubble detection with a more detailed model for foreground contamination, and to consider systematic effects from calibration errors and the MWA instrumental response. These considerations can also help in determining the optimal design for future surveys aimed at bubble detection. Our first efforts considering which configurations of antenna tiles are favorable for bubble detection, detailed in §2.15, suggest that an observing strategy intermediate to that of the MWA and LOFAR is favorable. It would also be interesting to consider the prospects for bubble identification across a larger range of reionization models than considered here. If the ionized regions at a given stage of reionization are, in fact, larger than in the models considered here, this should increase their

detectability. On the other hand, if the ionized regions are smaller than in our present models, this would likely diminish detectability, at least for the MWA-500.

If blind bubble identification is indeed feasible in future 21 cm surveys, we believe this will open up several interesting avenues of investigation. First, direct identification of ionized regions can help to build confidence in early redshifted 21 cm detections. Next, if the centers of ionized regions can be robustly identified, one may be able to use the brightness temperature contrast between the signal near the bubble's center and its surroundings to directly constrain the cosmic mean neutral fraction (e.g., Petrovic and Oh 48). These authors also discuss how detected bubbles can be used to calibrate foreground cleaning (Petrovic and Oh 48). Finally, identifying ionized regions in redshifted 21 cm surveys allows one to commence follow-up observations, comparing galaxy properties inside detected bubbles with those in more typical regions. Typical regions and likely neutral regions can be identified as locations in the data cube with average and maximal signal-to-noise ratios, respectively, after applying the matched filter. Furthermore, if the edge of an ionized region can be identified precisely enough, one might imagine targeted searches for galaxies at the edge of bubbles, close to neighboring neutral gas. Spectroscopic observations of these galaxies might then help to reveal the damping wing redward of the Ly-α line (e.g., Miralda-Escude 39). This would provide yet another means for constraining the neutral fraction.
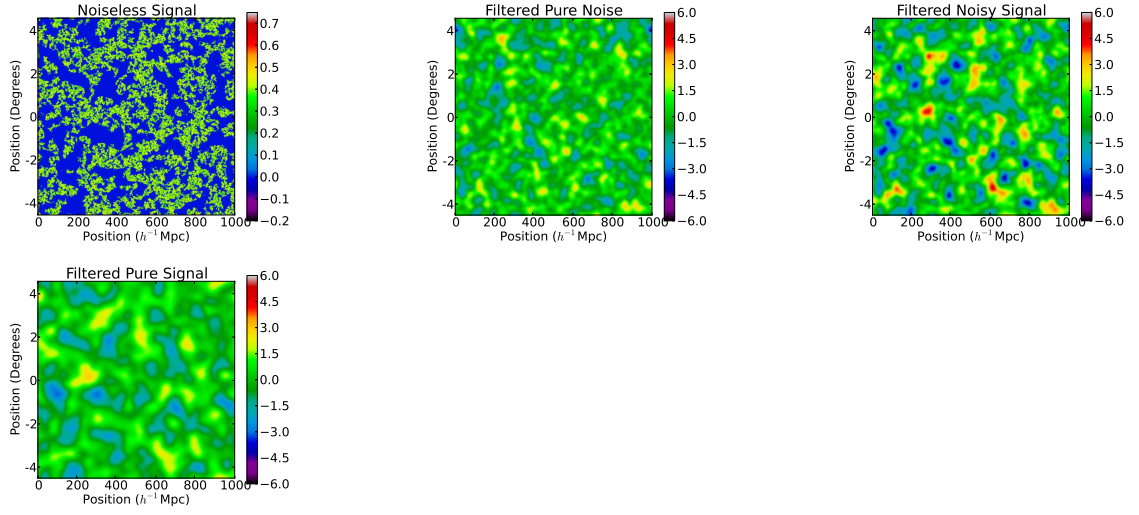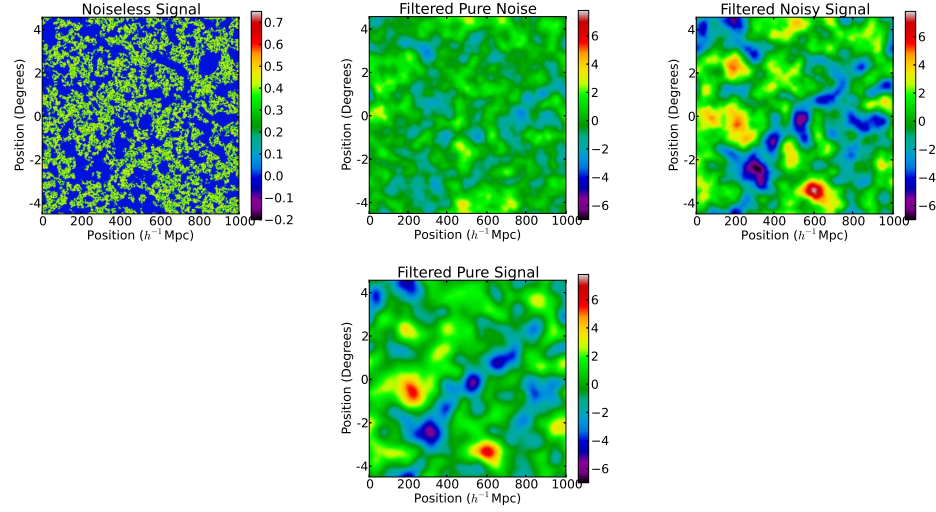
Figure 2.15: Application of the Wiener filter to simulated data. The results are for our fiducial model with $\langle x_i \rangle = 0.79$ at $z_{\text{fid}} = 6.9$. *Top-Left*: Spatial slice of the unfiltered and noise-less 21 cm brightness temperature contrast field (normalized by T_0). *Top-Right*: Simulated signal-to-noise field after applying the Wiener filter to a pure noise field. *Bottom-Left*: Simulated signal-to-noise field after applying the Wiener filter to the noisy signal. This can be compared with the uncorrupted input signal shown in the top-left panel and the noise realization in the top-right panel. *Bottom-Right*: Simulated signal-to-noise field after applying the Wiener filter to the noiseless signal. (The filtered noiseless signal shown here is normalized by the standard deviation of the noise to facilitate comparison with the other panels.) All panels show a square section of the MWA field of view transverse to the line of sight with sidelength $L = 1 \, h^{-1} \, \text{Gpc}$. All slice thicknesses are $\sim 8 \, h^{-1} \, \text{Mpc}$. Unless noted otherwise, the simulation slices in subsequent figures have these same dimensions.
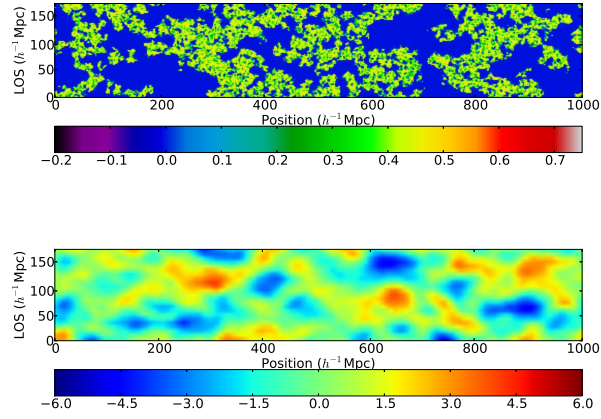
Figure 2.16: Impact of foreground cleaning on the Wiener-filtered field. The top slice is a perpendicular, zoomed-in view of the simulated, unfiltered, noise-less brightness temperature contrast. The bottom slice is the signal-to-noise of the same region after applying the Wiener filter to the noisy signal field. The vertical axis shows the line-of-sight direction, with its extent set to the distance scale for foreground removal, $L_{\mathrm{fg}} = 185\,h^{-1}\,\mathrm{Mpc}$. The horizontal axis shows a dimension transverse to the line of sight and extends $1\,h^{-1}\,\mathrm{Gpc}$.
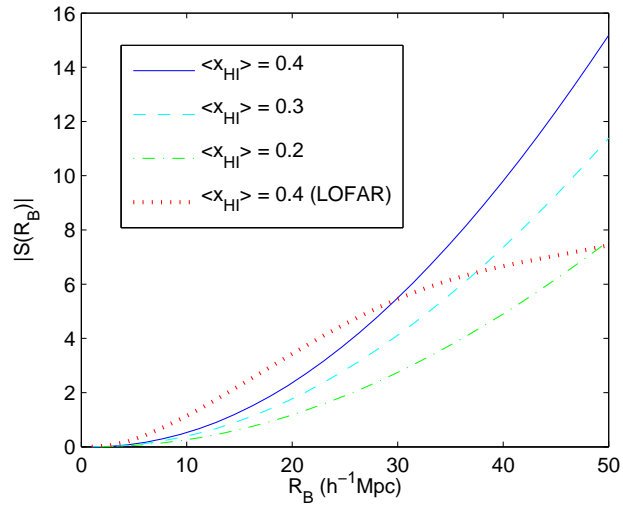
Figure 2.17: Expected signal-to-noise ratio at the center of isolated, spherical, ionized bubbles as a function of bubble radius after applying the optimal matched filter. The curves show the signal-to-noise ratio at $z_{\mathrm{fid}} = 6.9$ for the MWA-500 at various neutral fractions: $\langle x_{\mathrm{HI}} \rangle = 0.4$ (blue solid), 0.3 (cyan dashed), and 0.2 (green dot-dashed). For contrast, the red dotted curve indicates the expected signal-to-noise for an interferometer with a field of view and collecting area similar to a 32-tile LOFAR-like antenna array (at $\langle x_{\mathrm{HI}} \rangle = 0.4$).

Figure 2.18: Application of the matched filter to simulated data and noise ($\langle x_i \rangle = 0.79$ at $z_{\mathrm{fid}} = 6.9$). The template radius of the filter is $35\,h^{-1}\,\mathrm{Mpc}$, since this is a commonly detected bubble radius for our matched filter search. *Top-Left*: Spatial slice of the unfiltered and noise-less 21 cm brightness temperature contrast field. *Top-Right*: Simulated signal-to-noise field after applying the matched filter to a pure noise field. *Bottom-Left*: Simulated signal-to-noise field after applying the matched filter to the noisy signal. This can be compared directly to the top-left panel. *Bottom-Right*: Simulated signal-to-noise field after applying the matched filter to the noiseless signal. All panels are at the same spatial slice. See text for discussion on interpreting signal-to-noise values.
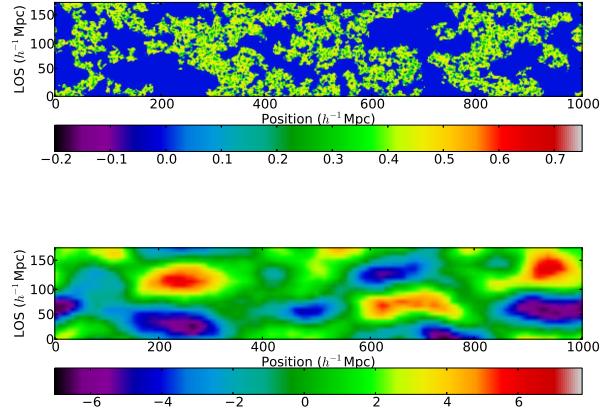
Figure 2.19: Impact of foreground cleaning on the matched-filtered field. This is similar to Figure 2.16, except that the results here are for a matched filter with a template radius of $R_{\rm T} = 35\,h^{-1}\,{\rm Mpc}$.
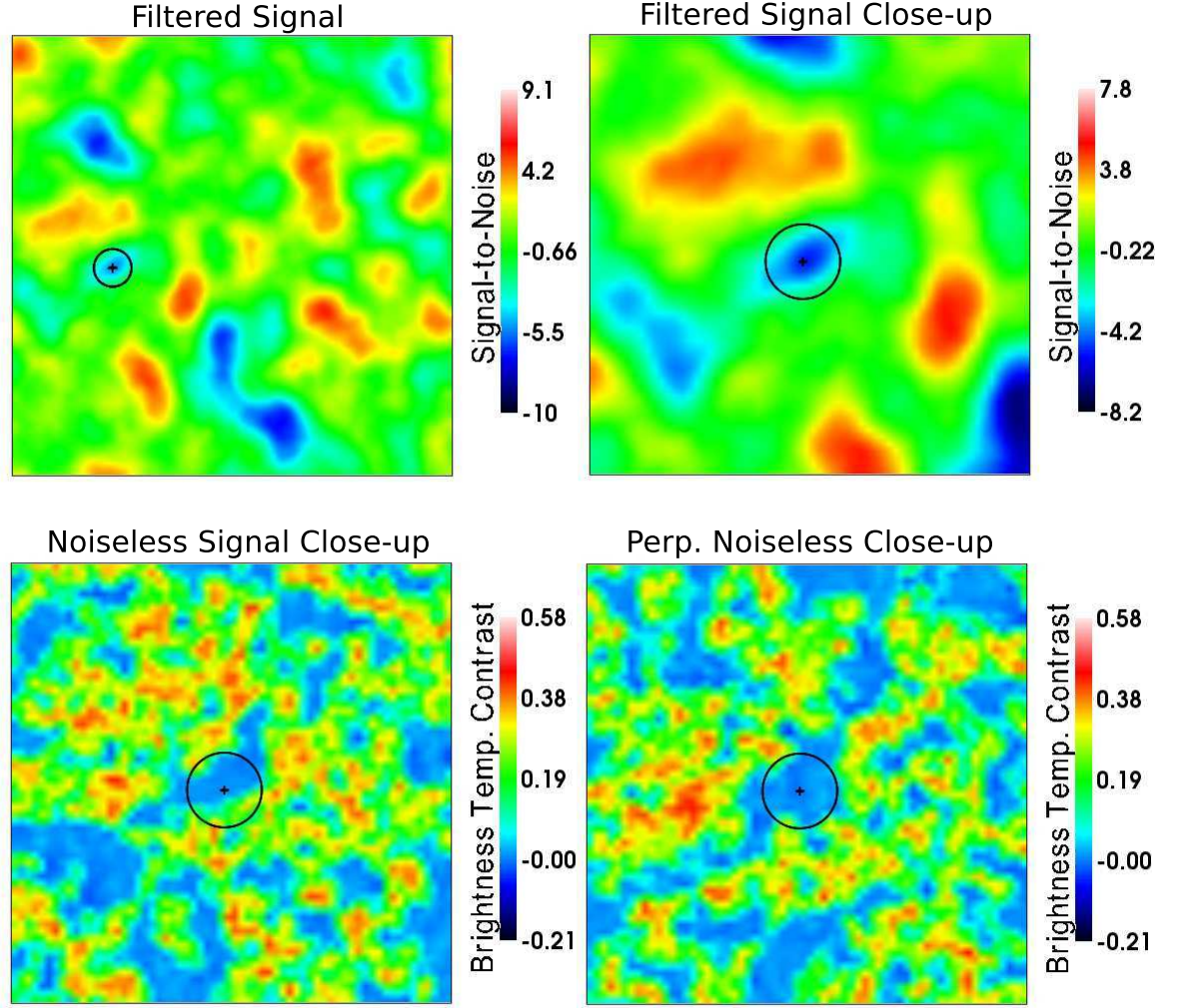
Figure 2.20: An example of a detected ionized region. *Top-left:* Signal-to-noise field after applying the matched filter to the noisy signal. The detected bubble is plotted on top of the corresponding region in the map. *Top-Right:* Zoomed-in view of the detected bubble in the matched-filtered map. *Bottom-Left:* Detected bubble superimposed on a zoomed-in view of the noise-less unfiltered 21 cm brightness temperature contrast map. *Bottom-Right:* A perpendicular zoomed-in view of the bubble depicted in the bottom-left panel. All matched-filtered maps use the template radius that minimizes the signal-to-noise at the center of the detected bubble. In the top-left case, the boxlength is $L = 1\,h^{-1}\,\mathrm{Gpc}$, while in the zoomed-in slices it is $L \approx 500\,h^{-1}\,\mathrm{Mpc}$.
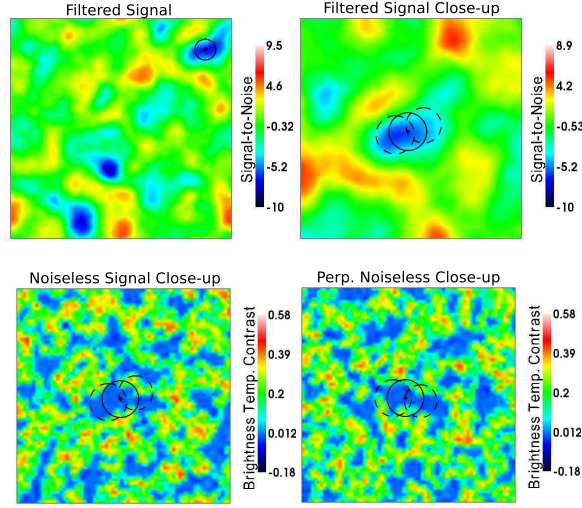
Figure 2.21: An example of an ionized region that our algorithm detects as several neighboring bubbles. *Top-left:* Signal-to-noise field after applying the matched filter to the noisy signal. The main detected bubble is plotted on top of the corresponding region in the map. *Top-Right:* Zoomed-in view of the main detected bubble in the matched filtered map (solid curve) along with two other nearby detected bubbles (dashed curve). *Bottom-Left:* The detected bubble superimposed on the zoomed-in, noise-less, unfiltered 21 cm brightness temperature contrast map. Again, the additional nearby detected bubbles are shown (dashed curve). *Bottom-Right:* A perpendicular view of the bubble depicted in the bottom-left panel, with the nearby detected bubbles visible. All matched-filtered maps use the template radius that maximizes the signal to noise at the center of the main detected bubble. The box length in the top-left figure is $L = 1\,h^{-1}\,\mathrm{Gpc}$, while in the zoomed-in panels, the box length is $L = 550\,h^{-1}\,\mathrm{Mpc}$.
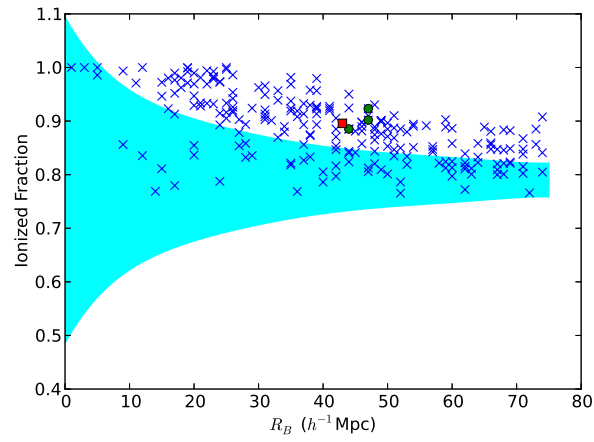
Figure 2.22: A measure of the bubble detection success rate. The points ($\times$) show the volume-averaged ionized fraction of detected bubbles versus their detected radius. For comparison, the cyan shaded region shows the 1-σ spread in the ionized fraction of *randomly* placed bubbles of the same radii. The bubble depicted in Fig. 2.20 is marked with a large red square, while the three bubbles shown in Fig. 2.21 are marked with large green circles.
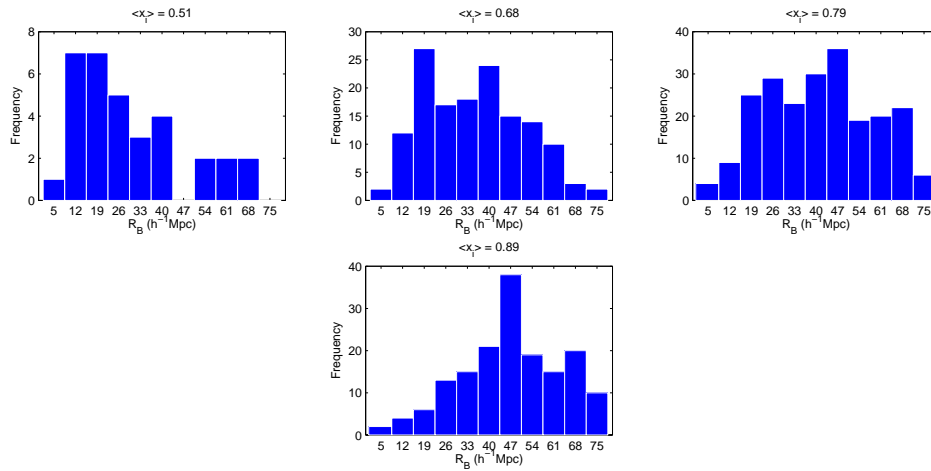
Figure 2.23: Size distributions of detected bubbles for varying (volume-averaged) ionization fractions. The histograms show the size distribution of (identified) ionized regions for simulation snapshots with volume-averaged ionized fractions of $\langle x_i \rangle = 0.51$ (top-left), 0.68 (top-right), 0.79 (bottom-left), and 0.89 (bottom-right). These figures demonstrate how the total number and size distribution of detected bubbles varies with ionized fraction.
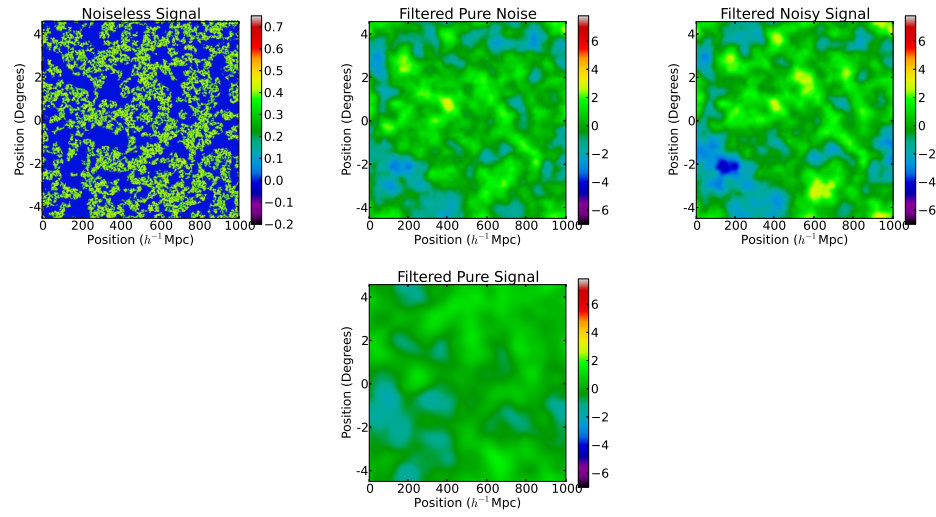
Figure 2.24: Bubble detection with the MWA-128. This figure is similar to Figure 2.18, except it is for the MWA-128 configuration rather than for the MWA-500.
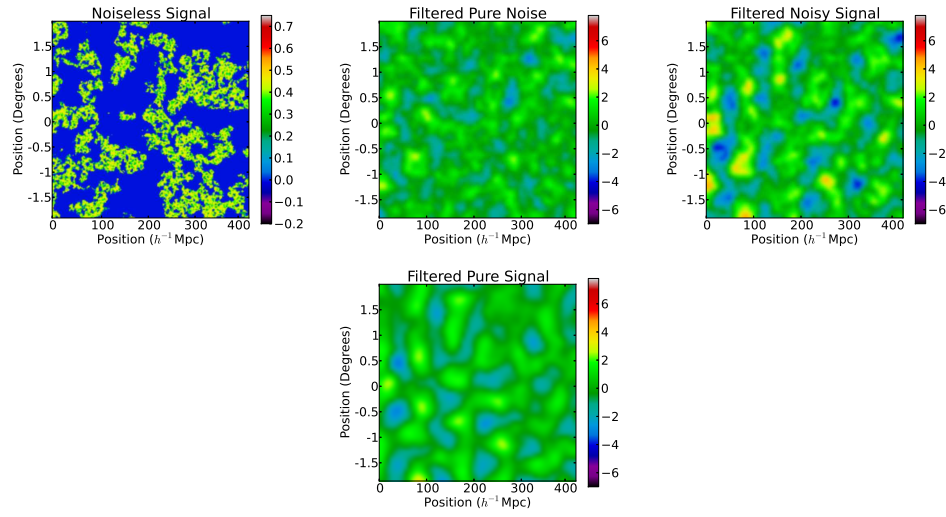
Figure 2.25: Bubble detection with a LOFAR-style interferometer. This figure is similar to Figure 2.18, except it is for the LOFAR configuration rather than the MWA-500. Additionally, all boxes in this figure have a side length of $426\,h^{-1}\,\mathrm{Mpc}$, corresponding to the field-of-view of the LOFAR-style interferometer at $z = 6.9$.

Chapter 3

Conclusion

3.1 Wrapping up...

I rest my case. Lorem ipsum dolor sit amet, consectetuer adipiscing elit. Ut purus elit, vestibulum ut, placerat ac, adipiscing vitae, felis. Curabitur dictum gravida mauris. Nam arcu libero, nonummy eget, consectetuer id, vulputate a, magna. Donec vehicula augue eu neque. Pellentesque habitant morbi tristique senectus et netus et malesuada fames ac turpis egestas. Mauris ut leo. Cras viverra metus rhoncus sem. Nulla et lectus vestibulum urna fringilla ultrices. Phasellus eu tellus sit amet tortor gravida placerat. Integer sapien est, iaculis in, pretium quis, viverra ac, nunc. Praesent eget sem vel leo ultrices bibendum. Aenean faucibus. Morbi dolor nulla, malesuada eu, pulvinar at, mollis ac, nulla. Curabitur auctor semper nulla. Donec varius orci eget risus. Duis nibh mi, congue eu, accumsan eleifend, sagittis quis, diam. Duis eget orci sit amet orci dignissim rutrum.

Nam dui ligula, fringilla a, euismod sodales, sollicitudin vel, wisi. Morbi auctor lorem non justo. Nam lacus libero, pretium at, lobortis vitae, ultricies et, tellus. Donec aliquet, tortor sed accumsan bibendum, erat ligula aliquet magna, vitae ornare odio metus a mi. Morbi ac orci et nisl hendrerit mollis. Suspendisse ut massa. Cras nec ante. Pellentesque a nulla. Cum sociis natoque penatibus et magnis dis parturient montes, nascetur ridiculus

mus. Aliquam tincidunt urna. Nulla ullamcorper vestibulum turpis. Pellentesque cursus luctus mauris.

Nulla malesuada porttitor diam. Donec felis erat, congue non, volutpat at, tincidunt tristique, libero. Vivamus viverra fermentum felis. Donec nonummy pellentesque ante. Phasellus adipiscing semper elit. Proin fermentum massa ac quam. Sed diam turpis, molestie vitae, placerat a, molestie nec, leo. Maecenas lacinia. Nam ipsum ligula, eleifend at, accumsan nec, suscipit a, ipsum. Morbi blandit ligula feugiat magna. Nunc eleifend consequat lorem. Sed lacinia nulla vitae enim. Pellentesque tincidunt purus vel magna. Integer non enim. Praesent euismod nunc eu purus. Donec bibendum quam in tellus. Nullam cursus pulvinar lectus. Donec et mi. Nam vulputate metus eu enim. Vestibulum pellentesque felis eu massa.

Quisque ullamcorper placerat ipsum. Cras nibh. Morbi vel justo vitae lacus tincidunt ultrices. Lorem ipsum dolor sit amet, consectetuer adipiscing elit. In hac habitasse platea dictumst. Integer tempus convallis augue. Etiam facilisis. Nunc elementum fermentum wisi. Aenean placerat. Ut imperdiet, enim sed gravida sollicitudin, felis odio placerat quam, ac pulvinar elit purus eget enim. Nunc vitae tortor. Proin tempus nibh sit amet nisl. Vivamus quis tortor vitae risus porta vehicula.

Fusce mauris. Vestibulum luctus nibh at lectus. Sed bibendum, nulla a faucibus semper, leo velit ultricies tellus, ac venenatis arcu wisi vel nisl. Vestibulum diam. Aliquam pellentesque, augue quis sagittis posuere, turpis lacus congue quam, in hendrerit risus eros eget felis. Maecenas eget erat in sapien mattis porttitor. Vestibulum porttitor. Nulla facilisi. Sed a turpis eu lacus commodo facilisis. Morbi fringilla, wisi in dignissim interdum, justo lectus sagittis dui, et vehicula libero dui cursus dui. Mauris tempor ligula sed lacus. Duis cursus enim ut augue. Cras ac magna. Cras nulla. Nulla egestas. Curabitur a leo. Quisque egestas wisi eget nunc. Nam feugiat lacus vel est. Curabitur consectetuer.

Suspendisse vel felis. Ut lorem lorem, interdum eu, tincidunt sit amet, laoreet vitae, arcu. Aenean faucibus pede eu ante. Praesent enim elit, rutrum at, molestie non, nonummy

vel, nisl. Ut lectus eros, malesuada sit amet, fermentum eu, sodales cursus, magna. Donec eu purus. Quisque vehicula, urna sed ultricies auctor, pede lorem egestas dui, et convallis elit erat sed nulla. Donec luctus. Curabitur et nunc. Aliquam dolor odio, commodo pretium, ultricies non, pharetra in, velit. Integer arcu est, nonummy in, fermentum faucibus, egestas vel, odio.

Sed commodo posuere pede. Mauris ut est. Ut quis purus. Sed ac odio. Sed vehicula hendrerit sem. Duis non odio. Morbi ut dui. Sed accumsan risus eget odio. In hac habitasse platea dictumst. Pellentesque non elit. Fusce sed justo eu urna porta tincidunt. Mauris felis odio, sollicitudin sed, volutpat a, ornare ac, erat. Morbi quis dolor. Donec pellentesque, erat ac sagittis semper, nunc dui lobortis purus, quis congue purus metus ultricies tellus. Proin et quam. Class aptent taciti sociosqu ad litora torquent per conubia nostra, per inceptos hymenaeos. Praesent sapien turpis, fermentum vel, eleifend faucibus, vehicula eu, lacus.

Appendices

Appendix A

Some Appendix

A.1 first section

Appendix B

Another Appendix

Glossary

Roman Symbols

M   Mass of object, page 113

Greek Symbols

τ Optical depth, page 113

Superscripts

*   Conjugate, page 113

Subscripts

$\odot$ relating to the sun (Sol), page 113

Other Symbols

11HUGS   11 Mpc Halpha and Ultraviolet Galaxy Survey, page 113

Acronyms

Ph.D   Acronym, page 1

2MASS   Two-Micron All Sky Sruvey, page 113

References

[1] Rennan Barkana and Abraham Loeb. In the beginning: The First sources of light and the reionization of the Universe. *Phys.Rept.*, 349:125–238, 2001. doi: 10.1016/S0370-1573(01)00019-9. 63

[2] A.P. Beardsley, B.J. Hazelton, M.F. Morales, W. Arcus, D. Barnes, et al. The EoR Sensitivity of the 128 Antenna Murchison Widefield Array. 2012. 90

[3] R.J. Bouwens, G.D. Illingworth, I. Labbe, P.A. Oesch, M. Trenti, et al. A candidate redshift z 10 galaxy and rapid changes in that population at an age of 500 Myr. *Nature*, 469:504–507, 2011. doi: 10.1038/nature09717. 88

[4] R.J. Bouwens, G.D. Illingworth, P.A. Oesch, M. Trenti, I. Labbe, et al. Lower-Luminosity Galaxies could reionize the Universe: Very Steep Faint-End Slopes to the UV Luminosity Functions at z¿=5-8 from the HUDF09 WFC3/IR Observations. 2011. 59

[5] Judd D. Bowman, Miguel F. Morales, and Jacqueline N. Hewitt. The Sensitivity of first generation epoch of reionization observatories and their potential for differentiating theoretical power spectra. *Astrophys.J.*, 638:20–26, 2006. doi: 10.1086/498703. 60, 65

[6] Judd D. Bowman, Miguel F. Morales, and Jacqueline N. Hewitt. Constraints on fundamental cosmological parameters with upcoming epoch of reionization observations. *Astrophys.J.*, 661:1–9, 2007. doi: 10.1086/516560. 65

[7] Emma Chapman, Filipe B. Abdalla, Geraint Harker, Vibor Jelic, Panagiotis Labropoulos, et al. Foreground Removal using FastICA: A Showcase of LOFAR-EoR. *Mon.Not.Roy.Astron.Soc.*, 423:2518–2532, 2012. doi: 10.1111/j.1365-2966.2012.21065.x. 67

[8] Benedetta Ciardi and Piero Madau. Probing beyond the epoch of hydrogen reionization with 21 centimeter radiation. *Astrophys.J.*, 596:1–8, 2003. doi: 10.1086/377634. 62

[9] A. Datta, J.D. Bowman, and C.L. Carilli. Bright Source Subtraction Requirements For Redshifted 21 cm Measurements. *Astrophys.J.*, 724:526–538, 2010. doi: 10.1088/0004-637X/724/1/526. 59

[10] Kanan K. Datta, Somnath Bharadwaj, and T. Roy Choudhury. Detecting ionized bubbles in redshifted 21 cm maps. *Mon.Not.Roy.Astron.Soc.*, 382:809, 2007. doi: 10.1111/j.1365-2966.2007.12421.x. 61, 93

[11] Kanan K. Datta, Suman Majumdar, Somnath Bharadwaj, and T. Roy Choudhury. Simulating the impact of HI fluctuations on matched filter search for ionized bubbles in redshifted 21 cm maps. *Mon.Not.Roy.Astron.Soc.*, 391:1900, 2008. 61, 93

[12] Kanan K. Datta, Garrelt Mellema, Yi Mao, Ilian T. Iliev, Paul R. Shapiro, et al. Light cone effect on the reionization 21-cm power spectrum. 2011. 68

[13] J. Dunkley et al. Five-Year Wilkinson Microwave Anisotropy Probe (WMAP) Observations: Likelihoods and Parameters from the WMAP data. *Astrophys.J.Suppl.*, 180:306–329, 2009. doi: 10.1088/0067-0049/180/2/306. 59

[14] Xiao-Hui Fan, Michael A. Strauss, Robert H. Becker, Richard L. White, James E. Gunn, et al. Constraining the evolution of the ionizing background and the epoch of reionization with z 6 quasars. 2. a sample of 19 quasars. *Astron.J.*, 132:117–136, 2006. doi: 10.1086/504836. 4, 5, 13, 15, 59, 88

[15] Martina M. Friedrich, Kanan K. Datta, Garrelt Mellema, and Ilian T. Iliev. Prospects of observing a quasar HII region during the Epoch of Reionization with redshifted 21cm. 2012. 60, 91, 94

[16] Steven Furlanetto and Adam Lidz. The Cross-Correlation of High-Redshift 21 cm and Galaxy Surveys. *Astrophys.J.*, 2006. 65

[17] Steven Furlanetto, Matias Zaldarriaga, and Lars Hernquist. Statistical probes of reionization with 21 cm tomography. *Astrophys.J.*, 613:16–22, 2004. doi: 10.1086/423028. 60

[18] Steven Furlanetto, Matias Zaldarriaga, and Lars Hernquist. The Growth of HII regions during reionization. *Astrophys.J.*, 613:1–15, 2004. doi: 10.1086/423025. 10, 60, 62, 70

[19] Steven Furlanetto, S. Peng Oh, and Frank Briggs. Cosmology at Low Frequencies: The 21 cm Transition and the High-Redshift Universe. *Phys.Rept.*, 433:181–301, 2006. 59

[20] Martin G. Haehnelt and Max Tegmark. Using the kinematic Sunyaev-Zeldovich effect to determine the peculiar velocities of clusters of galaxies. *Mon.Not.Roy.Astron.Soc.*, 279:545–556, 1996. 61

[21] Geraint Harker, Saleem Zaroubi, Gianni Bernardi, Michiel A. Brentjens, A.G. de Bruyn, et al. Non-parametric foreground subtraction for 21cm epoch of reionization experiments. *Mon.Not.Roy.Astron.Soc.*, 397:1138, 2009. 67

[22] Geraint Harker, Saleem Zaroubi, Gianni Bernardi, Michiel A. Brentjens, A.G. de Bruyn, et al. Power spectrum extraction for redshifted 21-cm epoch of reionization experiments: the LOFAR case. *Mon.Not.Roy.Astron.Soc.*, 405:2492–2504, 2010. 59

[23] Joseph F. Hennawi and David N. Spergel. Mass selected cluster cosmology. 1: Tomography and optimal filtering. *Astrophys.J.*, 2004. 61

[24] Ilian T. Iliev, Garrelt Mellema, Ue-Li Pen, Hugh Merz, Paul R. Shapiro, et al. Simulating cosmic reionization at large scales. 1. the geometry of reionization. *Mon.Not.Roy.Astron.Soc.*, 369:1625–1638, 2006. doi: 10. 1111/j.1365-2966.2006.10502.x. 60, 74

[25] E. Komatsu et al. Seven-Year Wilkinson Microwave Anisotropy Probe (WMAP) Observations: Cosmological Interpretation. *Astrophys.J.Suppl.*, 192:18, 2011. doi: 10. 1088/0067-0049/192/2/18. 61, 88

[26] M. Kuhlen and C.A. Faucher-Giguere. Concordance models of reionization: implications for faint galaxies and escape fraction evolution. 2012. 63, 88

[27] Adam Lidz, Oliver Zahn, Matthew McQuinn, Matias Zaldarriaga, and Suvendra Dutta. Higher Order Contributions to the 21 cm Power Spectrum. *Astrophys.J.*, 659:865–876, 2007. doi: 10.1086/511670. 76

[28] Adam Lidz, Oliver Zahn, Matthew McQuinn, Matias Zaldarriaga, and Lars Hernquist. Detecting the Rise and Fall of 21 cm Fluctuations with the Murchison Widefield Array. *Astrophys.J.*, 680:962–974, 2008. doi: 10.1086/587618. 60, 63, 71, 86, 90

[29] Adrian Liu and Max Tegmark. How well can we measure and understand foregrounds with 21 cm experiments? *Mon.Not.Roy.Astron.Soc.*, 419:3491–3504, 2012. doi: 10. 1111/j.1365-2966.2011.19989.x. 89

[30] Adrian Liu, Max Tegmark, Judd Bowman, Jacqueline Hewitt, and Matias Zaldarriaga. An Improved Method for 21cm Foreground Removal. *Mon.Not.Roy.Astron.Soc.*, 298: 401, 2009. 59, 64, 69

[31] Colin J. Lonsdale, Roger J. Cappallo, Miguel F. Morales, Frank H. Briggs, Leonid Benkevitch, et al. The Murchison Widefield Array: Design Overview. *IEEEP*, 97:1497, 2009. 59, 63

[32] Piero Madau, Avery Meiksin, and Martin J. Rees. 21-CM tomography of the intergalactic medium at high redshift. *Astrophys.J.*, 475:429, 1997. doi: 10.1086/303549. 59

[33] Yi Mao, Paul R. Shapiro, Garrelt Mellema, Ilian T. Iliev, Jun Koda, et al. Redshift Space Distortion of the 21cm Background from the Epoch of Reionization I: Methodology Re-examined. *Mon.Not.Roy.Astron.Soc.*, 422:926–954, 2012. doi: 10.1111/j.1365-2966.2012.20471.x. 62

[34] Laura Marian, Robert E. Smith, and Gary M. Bernstein. The cosmology dependence of weak lensing cluster counts. *Astrophys.J.*, 698:L33–L36, 2009. doi: 10.1088/0004-637X/ 698/1/L33. 61

[35] Matthew McQuinn, Oliver Zahn, Matias Zaldarriaga, Lars Hernquist, and Steven R. Furlanetto. Cosmological parameter estimation using 21 cm radiation from the epoch of reionization. *Astrophys.J.*, 653:815–830, 2006. doi: 10.1086/505167. 60, 63, 65, 67

[36] Matthew McQuinn, Adam Lidz, Oliver Zahn, Suvendra Dutta, Lars Hernquist, et al. The Morphology of HII Regions during Reionization. *Mon.Not.Roy.Astron.Soc.*, 377: 1043–1063, 2007. doi: 10.1111/j.1365-2966.2007.11489.x. 10, 60, 70, 71, 74, 77, 91

[37] Andrei Mesinger and Steven Furlanetto. Efficient Simulations of Early Structure Formation and Reionization. 2007. 62

[38] Andrei Mesinger, Steven Furlanetto, and Renyue Cen. 21cmFAST: A Fast, Semi-Numerical Simulation of the High-Redshift 21-cm Signal. *MNRAS*, 411:955, 2010. 60, 62

[39] Jordi Miralda-Escude. Reionization of the intergalactic medium and the damping wing of the Gunn-Peterson trough. *Astrophys.J.*, 501:15–22, 1998. doi: 10.1086/305799. 6, 95

[40] Miguel F. Morales and Jacqueline Hewitt. Toward epoch of re-ionization measurements with wide - field LOFAR observations. *Astrophys.J.*, 615:7–18, 2004. doi: 10.1086/424437. 60

[41] Miguel F. Morales, Bryna Hazelton, Ian Sullivan, and Adam Beardsley. Four Fundamental Foreground Power Spectrum Shapes for 21 cm Cosmology Observations. *Astrophys.J.*, 752:137, 2012. 59

[42] Daniel J. Mortlock, Stephen J. Warren, Bram P. Venemans, Mitesh Patel, Paul C. Hewett, et al. A luminous quasar at a redshift of z = 7.085. *Nature*, 474:616, 2011. 59

[43] Masami Ouchi, Kazuhiro Shimasaku, Hisanori Furusawa, et al. Statistics of 207 Lyα Emitters at a Redshift Near 7: Constraints on Reionization and Galaxy Formation Models. *Astrophys.J.*, 723:869, 2010. 59

[44] Benjamin J. Owen and B.S. Sathyaprakash. Matched filtering of gravitational waves from inspiraling compact binaries: Computational cost and template placement. *Phys.Rev.*, D60:022002, 1999. doi: 10.1103/PhysRevD.60. 022002. 61

[45] Gregory Paciga, Tzu-Ching Chang, Yashwant Gupta, Rajaram Nityanada, Julia Odegova, et al. The GMRT Epoch of Reionization experiment: A New upper limit on the neutral hydrogen power spectrum at z 8.6. *Mon.Not.Roy.Astron.Soc.*, 413:1174–1183, 2011. doi: 10. 1111/j.1365-2966.2011.18208.x. 59

[46] Aaron R. Parsons, Donald C. Backer, Richard F. Bradley, James E. Aguirre, Erin E. Benoit, et al. The Precision Array for Probing the Epoch of Reionization: 8 Station Results. 2009. 59

[47] Aaron R. Parsons, Jonathan C. Pober, James E. Aguirre, Christopher L. Carilli, Daniel C. Jacobs, David Moore, et al. A Per-Baseline, Delay-Spectrum Technique for Accessing the 21cm Cosmic Reionization Signature. 2012. 59

[48] Nada Petrovic and S. Peng Oh. Systematic Effects of Foreground Removal in 21cm Surveys of Reionization. 2010. 59, 67, 95

[49] William Press, Saul Teukolsky, William Vetterling, and Brian Flannery. *Numerical Recipes in C++: The Art of Scientific Computing.* Cambridge University Press, 2002. 68

[50] M.A. Schenker, D.P Stark, R.S. Ellis, B.E. Robertson, J.S. Dunlop, et al. Keck Spectroscopy of Faint 3¡z¡8 Lyman Break Galaxies:- Evidence for a Declining Fraction of Emission Line Sources In the Redshift Range 6¡z¡8. *Astrophys.J.*, 744:179, 2012. doi: 10.1088/0004-637X/744/2/179. 59

[51] S.J. Tingay, R. Goeke, J.D. Bowman, D. Emrich, S.M. Ord, et al. The Murchison Widefield Array: the Square Kilometre Array Precursor at low radio frequencies. 2012. 63

[52] Tomonori Totani, Nobuyuki Kawai, George Kosugi, Kentaro Aoki, Toru Yamada, et al. Implications for the cosmic reionization from the optical afterglow spectrum of the gamma-ray burst 050904 at z = 6.3. *Publ.Astron.Soc.Jap.*, 58:485–498, 2006. 59

[53] Xiao-Min Wang, Max Tegmark, Mario Santos, and Lloyd Knox. Twenty-one centimeter tomography with foregrounds. *Astrophys.J.*, 650:529–537, 2006. doi: 10.1086/ 506597. 67

[54] J. Stuart B. Wyithe and Abraham Loeb. Redshifted 21cm signatures around the highest redshift quasars. *Astrophys.J.*, 610:117–127, 2004. doi: 10.1086/421042. 60, 91

[55] Stuart Wyithe and Miguel F. Morales. Biased Reionisation and Non-Gaussianity in Redshifted 21cm Intensity Maps of the Reionisation Epoch. *Mon.Not.Roy.Astron.Soc.*, 2007. 65

[56] O. Zahn, C.L. Reichardt, L. Shaw, A. Lidz, K.A. Aird, et al. Cosmic microwave background constraints on the duration and timing of reionization from the South Pole Telescope. *Astrophys.J.*, 756:65, 2012. doi: 10.1088/0004-637X/756/1/ 65. 59, 63

[57] Oliver Zahn, Adam Lidz, Matthew McQuinn, Suvendra Dutta, Lars Hernquist, et al. Simulations and Analytic Calculations of Bubble Growth During Hydrogen Reionization. *Astrophys.J.*, 654:12–26, 2006. doi: 10.1086/509597. 60, 62, 63, 74, 76, 77, 86

[58] Oliver Zahn, Andrei Mesinger, Matthew McQuinn, Hy Trac, Renyue Cen, et al. Comparison Of Reionization Models: Radiative Transfer Simulations And Approximate, Semi-Numeric Models. 2010. 63

[59] Matias Zaldarriaga, Steven R. Furlanetto, and Lars Hernquist. 21 Centimeter fluctuations from cosmic gas at high redshifts. *Astrophys.J.*, 608:622–635, 2004. doi: 10.1086/ 386327. 59, 60, 62

[60] S. Zaroubi, A.G. de Bruyn, G. Harker, R.M. Thomas, P. Labropolous, et al. Imaging neutral hydrogen on large-scales during the Epoch of Reionization with LOFAR. 2012. 67, 92